Matthias Blaickner

Monte Carlo simulations of an ensemble of reference phantoms as a basis towards a more individual dose assessment in Nuclear Medicine

DOCTORAL THESIS

For obtaining the academic degree of

Doktor der technischen Wissenschaften

Doctoral Programme of Technical Sciences
Technical Physics

Graz University of Technology

Supervisor:

Ao. Univ. Prof. Dr. phil. Peter Kindl
Institute of Materials Physics

Graz, November 2010

Acknowledgments

I'd like to thank the people who supported me by one means or another in completing this thesis.

Ao. Univ. Prof. Dr. phil. Peter Kindl, my doctoral supervisor at the Graz University of Technology for making this thesis possible and providing assistance all the time.

Dr. Thomas Geringer, my former boss at the research center formerly known as Seibersdorf who gave me the opportunity to develop a new field of research and whose support made me a full time researcher.

Dr. Christa Nöhammer, my current boss, who has supported my research ever since the restructuring of what now is called AIT Austrian Institute of Technology GmbH (and formerly Austrian Research Centers Seibersdorf)

Ao. Univ. Prof. DI. Dr. Helmuth Böck, from the Atomic Institute of the Vienna University of Technology for acting as second reviewer.

Dr. Nina Petoussi-Henss from the GSF for the provision of SAFs of some of their voxel phantoms.

Additionally I want to express my gratitude to all the scientists and physicists that provided ideas and suggestions with regard to my work and of course my colleagues at the AIT who are simply fun to work with.

Last but not least I want to thank my family and especially my parents who supported the university education that led to this work. Above all I want to thank my partner in life Bernadette and my son Sammy because their presence in my life always reminds me that there are so many things much more important than the hodge-podge of facts and figures we call science.

Dammit, man! I'm a doctor, not a physicist!

true words, spoken by Leonard 'Bones' McCoy,
"Star Trek" (2009)

Kurzfassung

Einleitung: Die Dosimetrie in der Nuklearmedizin hängt sehr stark von publizierten S-Faktoren ab, die ihrerseits wieder auf errechneten Specific Absorbed Fractions (SAFs) basieren, die für eine begrenzte Anzahl von anthropomorphen, mathematischen Phantomen, bekannt als die Cristy/Eckerman Reihe zur Verfügung stehen. Um eine individuellere Dosisabschätzung zu ermöglichen, zielt diese Arbeit darauf ab, das Angebot an Phantomen und deren SAFs zu verbreitern.
Methodik: Ein Ensemble bestehend aus 21 mathematischen Phantomen wurde mit dem Monte Carlo Code MCNP4c2 zum Zwecke der Berechnung der SAFs für die Vernichtungsstrahlung simuliert. Diese Werte wurden gemäß dem MIRD-System (Medical Internal Radiation Dose) in eine interne Dosisberechnung inkorporiert indem auf publizierte, biokinetische Daten für eine intravenöse Verabreichung von ^{18}F-FDG zurückgegriffen wurde. Die Ergebnisse wurden mit Resultaten der ICRP, der MIRD-Berichte und begleitenden Berechungen anhand von OLINDA/EXM verglichen.
Resultate: Es konnte ein sehr gute Übereinstimmung mit jenen Quellen beobachtet werden, die sich auf die SAFs von Cristy und Eckerman stützen, also die ICRP und OLINDA/EXM, d.h. die überwiegende Mehrheit der Organe und Altersgruppen zeigen minimale Abweichungen. Im Falle des roten Knochenmarks wurden die King Spiers Faktoren in der Drei-Faktoren-Annäherung weggelassen, was zu einer präzisen Übereinstimmung mit den Ergebnissen von Cristy und Eckerman führt. Einzelne, Ausreißer verursachende SAFs konnten identifiziert werden, als auch die wenigen Organe, die nicht für die gewählte Methodik der Dosisberechnung geeignet sind.
Conclusio: Die gute Übereinstimmung dieser Arbeit mit OLINDA/EXM Berechnungen, d.h. der Vergleich unter Referenzphantomen und deren vergleichsweise hohe Abweichung von den in MIRD 19 tabellierten Werten, welche gemittelte Dosen von individuellen Abschätzungen darstellen, unterstreicht die Präferenz von Referenzphantomen. Das Ensemble erlaubt die Diskretisierung in so viele Phantome, daß die Energiedosis eines Organs oder die Effektivdosis als Funktion von physischen Parametern wie Größe oder Gewicht als glatte Kurve dargestellt werden kann. Zusammenfassend kann man sagen, daß die Ergebnisse eine Bestätigung der

oft verwendeten SAFs von Cristy und Eckerman sind und daß die Vergrößerung des Spektrums von Phantomen eine hößhere Diversität erzeugt und somit vor allem im Falle des Fehlens von zusätzlicher Information des Patienten in Form bildgebender Verfahren wie CT oder MR eine individuellere Dosisabschätzung ermöglicht.

Abstract

Introduction: Dosimetry in Nuclear Medicine strongly depends on published S-values, which are based on calculated specific absorbed fractions (SAFs) available for a limited number of anthropomorphic, mathematical phantoms known as the Cristy and Eckerman series. In order to enable a more individual dose assessment this study aimed to broaden the supply of phantoms and their respective SAFs.
Material and Methods: An ensemble of 21 mathematical phantoms was submitted to the Monte Carlo Code MCNP4c2 for the purpose of calculation of SAFs for annihilation radiation. These values were incorporated into an internal dose assessment following the Medical Internal Radiation Dose (MIRD) schema and relying on published biokinetic data for intravenous administration of ^{18}F-FDG. The results were compared with data from the ICRP, MIRD reports and concurrent calculations with OLINDA/EXM.
Results: A very good agreement with sources relying on the SAFs of Cristy and Eckerman (i.e., the ICRP and OLINDA/EXM) was observed, i.e. the large majority of organs and age groups show minimal deviations. In the case of dose to red marrow, the King Spiers factors were omitted in the three-factor approximation, which led to a precise accordance with the Cristy/Eckerman values. Some individual SAFs causing outliers could be identified as well as the few organs not suitable for the method chosen.
Conclusion: The good accordance of this study with OLINDA/EXM calculations, i.e. comparison of reference models among themselves and their comparatively big deviations to the values of MIRD 19 which are averaged means from individual estimates underlines the preference of reference models. The ensemble allows discretization into so many phantoms, that the absorbed dose to an organ or to the whole body as a function of a phantom parameter such as weight can be depicted as a smooth curve. Summarizing, one can say that the results are a confirmation of the widely used SAFs produced by Cristy and Eckerman and that the enlargement of the available array of phantoms creates a bigger diversity, therefore enabling a more individual dose assessment, above all in the case of the absence of any additional imaging information of the patient, such as CT or MRI.

List of Abbreviations

3CF	Three Correction Factor
AF	Absorbed Fraction
CE	Conversion Electron
CT	Computed Tomography
FDA	U.S. Food and Drug Administration
FDG	Flourodeoxyglucose
FDR	Fluence-to-Dose Response
GSF	GSF-Forschungszentrum für Umwelt und Gesundheit (National Research Center for Environment and Health)
ICRP	International Commission of Radiological Protection
ICRU	International Commission of Radiation Units and Measurements
LET	Linear Energy Transfer
LINAC	Linear Accelerator
MCNP	Monte Carlo N-Particle
MIRD	Medical Internal Radiation Dose
MR	Magnetic Resonance
NURBS	Nonuniform Rational B-Spline
OLINDA/EXM	Organ Level Internal Dose Assessment with Exponential Modeling

ORNL	Oak Ridge National Laboratory
PET	Positron Emission Tomography
REM	Remaining Tissue
RIT	Radioimmunotherapy
RM	Red Bone Marrow
ROI	Region of Interest
SAF	Specific Absorbed Fraction
SPECT	Single Photon Emission Computed Tomography
TAC	Time-Activity Curve
TB	Total Body
TRT	Targeted Radionuclide Therapy

Contents

Chapter 1

Introduction

The scientific work presented in this thesis is based on following publications:

- M. Blaickner and P. Kindl.
  Diversification of Existing Reference Phantoms in Nuclear Medicine: Calculation of Specific Absorbed Fractions for 21 Mathematical Phantoms and Validation Through Dose Estimates Resulting from the Administration of ^{18}F-FDG.
  Cancer Biotherapy & Radiopharmaceuticals 23(6):767-82, 2008. [1]

- M. Blaickner and P. Kindl.
  New Specific Absorbed Fractions for Annihilation Radiation as a Step towards a more Individual Dosimetry in Nuclear Diagnostics
  Second European IRPA Congress on Radiation Protection, Paris, France; 15.05.2006 - 19.05.2006; in: Second European IRPA Congress on Radiation Protection Second European IRPA Congress on Radiation Protection, Proceeding of Full Papers CD-ROM, Paris (2006).

- M. Blaickner and P. Kindl.
  Steps towards an Individual Treatment Planning with the Internal Dosimetry of ^{18}F-FDG as example for Nuclear Diagnostics and perspectives for Internal Radiation Therapy.
  14th International Conference of Medical Physics of the International Organization for Medical Physics and the German Society of Medical Physics (DGMP), Nürnberg, Deutschland; 13.09.2005 - 18.09.2005; in: 14th International Conference of Medical Physics of the International Organization for Medical Physics and the German Society of Medical Physics (DGMP), Biomedizinische Technik; Proceedings of the jointly held Congresses. Schiele & Schön GmbH, Nürnberg, Deutschland (2005), Part 1 2005; S. 921 - 922.

Text passages, figures and tables originally published in these publications, especially the paper in the peer reviewed journal, were partly incorporated into this work but elaborated in a much more detailed way since a scientific article has to be formulated brief and condensed and hence not all the relevant findings could be displayed there. This thesis is structured as follows:

Chapter 2 gives a brief overview over the different applications in Nuclear Medicine. On the diagnostic side this involves planar scintigraphy, Single Photon Emission Computed Tomography (SPECT) as well as Positron Emission Tomography (PET) and its combination with Computed Tomography (CT) , PET-CT. The underlying physical and technical principles of the different detection systems are outlined and examples of radioactive tracers are listed together with their respective medical fields of applications. With regard to therapeutic applications the basic concept of Targeted Radionuclide Therapy (TRT) is explained and lists of tumor-targeting agents and typical therapeutic radionuclides are invoked.

Chapter 3 is dedicated to the mathematical system of internal dose calculation, namely the MIRD-System by the Medical Internal Radiation Dose (MIRD) Committee as well as the motivation for this work. The necessary physical quantities and their definitions are introduced. Most important the two essential quantities within the MIRD-System are discussed in detail: The cumulated activity $\tilde{A}(r_S, T_D)$ and the residence time $\tilde{a}(r_S, T_D)$ respectively refer to the biokinetic behavior of the tracer whereas the S-value $S(r_T \leftarrow r_S)$ contains the description of the internal radiation transport. The S-value is based on specific absorbed fractions (SAFs) which stem from Monte Carlo simulations for the reference phantom series of Cristy and Eckerman or individual voxel models. After a précis about available phantoms for internal dose calculation the basic idea of the thesis is outlined: The development of a whole ensemble of mathematical phantoms and their respective S-values and SAFs in order to cover the spectrum of human anatomy. As a first step toward such an ensemble, the Cristy and Eckerman series is to be expanded into 21 phantoms, the SAFs for annihilation radiation calculated, and subsequently the S-values for ^{18}F, which then are incorporated into an internal dose calculation for the intravenous administration of ^{18}F-flourodeoxyglucose (FDG) , using the biokinetic data from MIRD Dose Estimate Report No. 19 and the International Commission of Radiological Protection (ICRP) Publication 80 .

Chapter 4 describes the details of the simulation model. Starting with the principle of Monte Carlos calculations the code used for this study, MCNP, is briefly described as well as additional software like BodyBuilder. The ensemble's anatomic features and other data relevant for radiation transport are outlined as well as the biokinetic input and particular approximations. A special emphasis is put on the calculation of the absorbed dose to red marrow and bone surface. The

different approaches of state of the art bone dosimetry are illustrated including the specific methods chosen for this study.

Chapter 5 lists the results of the simulations and dose calculations. Due to a sufficient number of histories the simulations shows very good statistical properties, providing very small uncertainties for individuals SAFs. The comparison with the organ absorbed doses listed in ICRP 80 demonstrates that for the vast majority of organs and age groups there is an excellent agreement. In the case of dose to red marrow, the omission rather than the inclusion of the King Spiers factors leads to a precise accordance with the Cristy/Eckerman values. Some outliers with regard to particular phantom ages are identified as well as organs showing general discrepancies for all age groups. This is confirmed when crosschecked with the dose calculation program OLINDA/EXM. As for the comparison with MIRD 19 it turns out that there is an extraordinary good agreement between the ensemble's results and concurrent calculations with OLINDA/EXM using MIRD 19 biokinetics, the lung being the only exception. On the other side the averaged mean doses from individual estimates tabulated in the same report deviate from this study as well as OLINDA/EXM results.

Chapter 6 discusses the results and their implications. The disagreement of the results tabulated in MIRD Dose Estimate Report No. 19 and calculations with reference models like OLINDA/EXM or this study give evidence that averaged mean doses from individuals are less suited for whole body dosimetry than reference models which introduce a form of standardization. Additionally organ absorbed dose values like the one referring to the brain can't be correct in MIRD 19 which is why it should be revised. As for the outliers listed in chapter 5 individual SAFs stemming from inaccurate anatomic modeling by BodyBuilder are identified as the cause and the strong influence of the specific biokinetics applied on the deviations is demonstrated. With regard to the organ absorbed doses showing a general discrepancy the methods and models chosen for this study are not applicable. It is shown that the case of the lung remains an issue somewhat unresolved due to the rather broad spreading of respective SAFs available in literature. Finally the limitations, the reliability as well as the applicability of the results are discussed. The very good accordance with published data for the majority of organs and the findings of many recent studies that confirm the validity of SAFs from mathematical phantoms in the light of the anatomically more realistic voxel phantoms prove the basic idea to be promising since in most cases of nuclear medicine exams no CT or MR scans are made. This is why the enlargement of the available array of phantoms creates a bigger diversity and therewith enables a more individual dose assessment.

Chapter 7 contains brief concluding remarks that summarize the findings and give an outlook on future studies.

Chapter 2

Applications in Nuclear Medicine

Nuclear Medicine refers to the branch of medicine that makes use of radiopharmaceuticals, i.e. pharmaceuticals which are labeled with a radionuclide. The radiation emitted by the radioactive isotope serves a diagnostic or therapeutic purpose. This chapter gives a brief overview over the current and most frequent applications in Nuclear Medicine.

2.1 Diagnostic applications

Procedures in nuclear diagnostics rely on the penetrating properties of photon radiation. This way a radioactive compound within the human body can be traced from outside by means on an appropriate detector, hence the term "tracer". The applied quantities are chosen small enough to ensure that the metabolism to be monitored is not significantly altered. In some cases the isotope itself is the tracer (e.g. iodine isotopes for thyroid scintigraphy), in others the tracer consists of a radionuclide attached to a carrier molecule where the later participates in metabolic processes and the radionuclide just acts as a marker that enables the pursuit of the carrier (e.g. ^{18}F-fluorodeoxyglucose, abbreviated FDG, for applications in oncology [2]). Different types of nuclides are used as photon sources, such as:

- Radionuclides with a prompt γ-line, e.g. ^{131}I
- Nuclear isomers, e.g. $^{99\mathrm{m}}$Tc
- Nuclides undergoing β^+-decay which causes the emission of annihilation radiation, e.g. ^{18}F

Nuclear medicine imaging is also referred to as radionuclide imaging or nuclear scintigraphy. In order to avoid confusion about technical terms the expression *planar scintigraphy* is used with regard to the imaging technique that projects

the emitted radiation on an image plane with respect to only one angle and thus produces a cross section of the whole object. As a contrast emission tomography like SPECT or PET measures projections with regard to multiple angles and yields a so called tomogram which is the stacking of two dimensional images of the object's layers (cf. Computer Tomography).

The following overview of procedures in nuclear diagnostics only serves an introducing and accompanying purpose for the later chapters on dosimetry. Recommendations for further reading are given in the respective sections.

2.1.1 Planar Scintigraphy

As explained above planar scintigraphy detects the photon radiation emitted within the human body from one angle and generates a two dimensional cross section of the object. The corresponding instrument is known as a gamma camera and

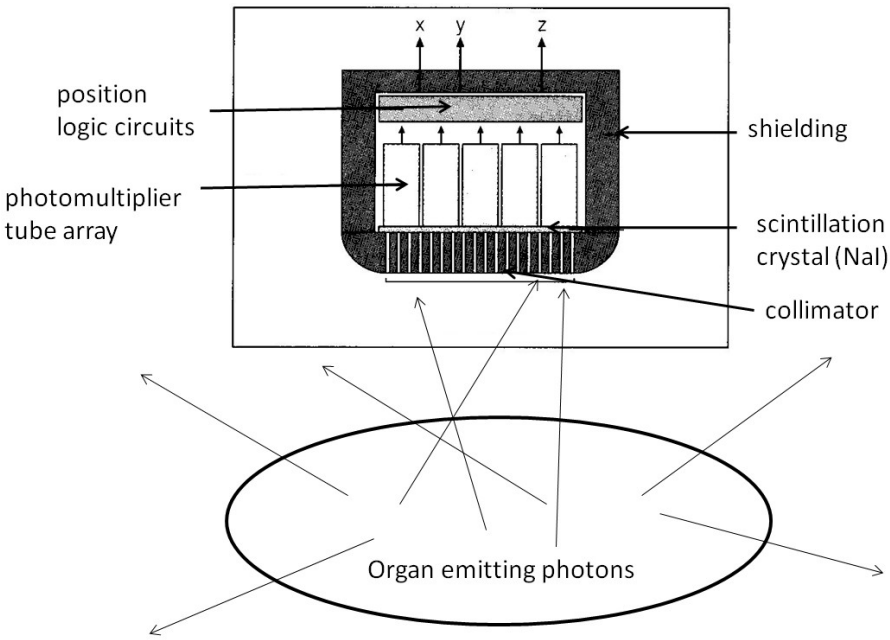

Figure 2.1: Composition and principle of gamma camera.

roughly consists of collimator, scintillation crystal, photomultiplier tube array, position logic circuits and a data analysis computer (see figure 2.1). The collimator usually consists of series of drilled holes within an absorbing material like lead or tungsten. The drilling which lies on the symmetry axis of the radiation cone gets fully penetrated by photons. The bigger the angle between the symmetry axis of the radiation cone and the flight direction of photon the more the holes cast a

shadow on the side of the collimator where the photons exit. Thereby the intensity profile of the collimated photons of a point source is a Gaussian curve. Photons

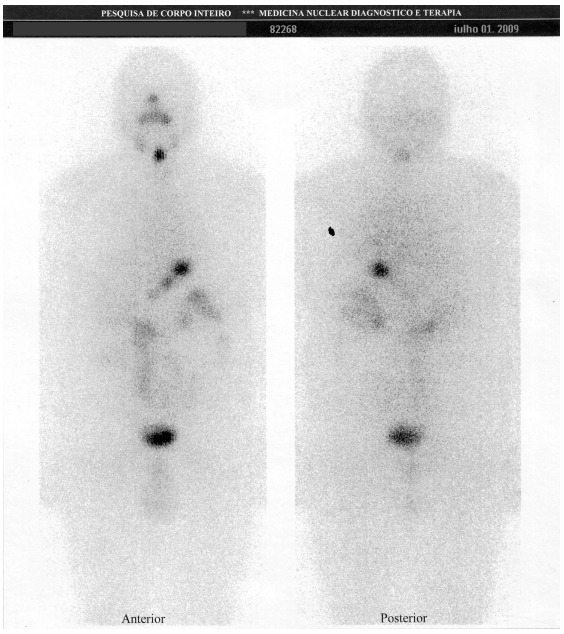

Figure 2.2: A scintigraphy of the whole body using a gamma camera detector and ^{131}I. The image shows uptake of iodine in the thyroid region due to thyroid cancer. Uptake seen in other regions (mouth, salivary glands, colon, stomach and urinary bladder) are due to normal excretion. The image does not show metastases in other regions. From Ref. [3].

deliver their energy within the sodium iodine crystal (NaI) and produce secondary photo-, Compton- and pair production electrons. The secondary electrons on the other hand get slowed down and loose energy via emission of light quanta that knock electrons out of the photocathode placed next to the crystal. Thereupon the electrons get multiplied in a photomultiplier and a large cluster of electrons is converted into an electric pulse. The pulse height is proportional to the energy of the electron. Finally the electric impulses are received by the positions logic circuits and allows the determination of the position of each scintillation event in the detector crystal.

There are two basic types of scintigraphy:

- **cold spot scintigraphy:** Imaging of normal organ tissue. Healthy tissue enriches the tracer whereas disease-modified organs show a deficit in uptake (cold spot).

- **hot spot scintigraphy:** Use of revere mechanism. Involves the use of radiopharmaceuticals that have little or no uptake in healthy tissue but preferable enrich in sites of diseases. A disease-modified process therefore shows a high activity concentration (hot spot).

An example of a scintigraphy is given in figure 2.2. For further literature on scintigraphy *Physics in nuclear medicine* [4] by Cherry, Sorenson and Phelps is recommended.

2.1.2 SPECT

As in planar scintigraphy nuclides applied in Single Photon Emission Computed tomography (SPECT) emit γ-radiation, e.g. ^{131}I, ^{123}I, ^{99m}Tc or ^{111}In. The stan-

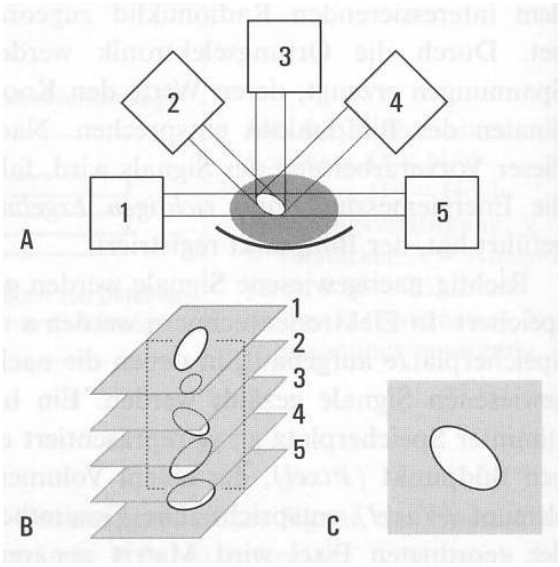

Figure 2.3: Principle of SPECT: A: Registration of projections at different positions, hence angles; B: Single projections are processed into tomogram by back projection (C).

dard construction of a SPECT-system is a measuring head of a gamma camera that rotates 360° around the patient. An engine powered holder moves the measuring head (mostly) stepwise on a circular path around the symmetry axis. After each angular step a two-dimensional projection of the object is registered. Out of these projections a set of parallel layers is reconstructed by means of projecting them into an image matrix. This is referred to as back projection which is a two dimensional image of the objects layer. Since the individual projections are registered successively a quasi stationary activity distribution within the patient during

the exam is necessary. Fast and dynamic processes cannot be captured although multi-headed gamma cameras can speed up the acquisition. The hybrid system SPECT-CT is not discussed here since the underlying technique and principle of co-registering two images from different gantries is the same as PET-CT which is described in the next section.

Typical medical exams employing SPECT imaging involves myocardial perfusion imaging [5], functional brain imaging and diagnosis of different forms of dementia [6]. For further literature on SPECT *Emission tomography: the fundamentals of PET and SPECT* [7] by Wernick and Aarsvold is recommended.

2.1.3 PET

SPECT makes use of spatially directed measuring of γ-rays by applying a mechanical collimator which results in a projection beam in form of a cone. Positron Emission Tomography (PET) on the other side makes use of a physical effect which results from the $\beta+$ decay, namely the emission of annihilation radiation. As tracers $\beta+$ emitters like ^{18}F, ^{11}C, ^{13}N and ^{15}O are in use whose emitted positron annihilates with an electron and thereby results in two photons of exactly 511 keV. If the positron at the moment of annihilation had zero kinetic energy the emission of the two photons would occur at an angle of exactly 180°. Since this is very unlikely to happen the emission angle between the two photons deviates somewhat from 180°.

Consequently in the case of a spatially directed measuring of positron emitters the collimation is realized electronically by means of facing detectors and using coincidence statistics. A decay is accepted as signal and further processed if the two photons get registered at both sides at the according angular position in a certain time interval (see figure 2.4). With the help of filtered back projection these information is used to reconstruct layers which can be displayed as tomographic image. Modern PET-scanners use detectors arranged on one or multiple rings. Since PET doesn't have to rely on mechanical collimators the measuring sensitivity increases. The good spatial and temporal resolution allows for an absolute activity quantification including the specification of flow and metabolic rates (e.g. in ml/min or mmol/min) by consideration of absorption and special algorithms for analysis. This way PET provides a noninvasive imaging of biochemical processes within the living organism without altering the physical or chemical properties. The medical fields of applications for PET are numerous and involve oncology [2], neurology [9], cardiology [10], psychiatry [11] and many more.

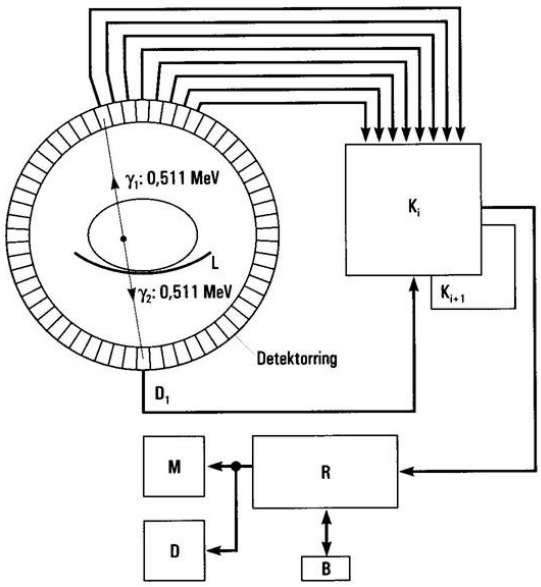

Figure 2.4: Principle of PET: Annihilation radiation gets emitted within the human body and measured by means of a detector ring and using coincidence statistics.

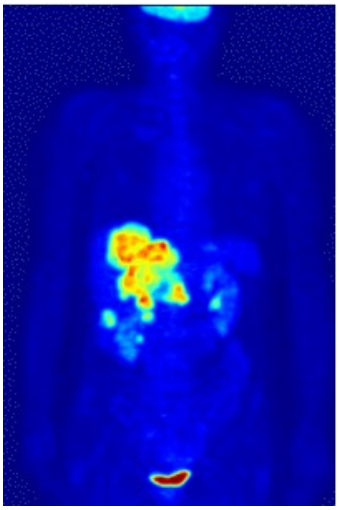

Figure 2.5: Whole body PET with ^{18}F-FDG, showing abnormal focal uptake in the liver. Normal isotope levels are seen in the brain, renal system and bladder. From Ref. [8].

PET-CT

One of the most important developments in recent years is the the combination of Computed Tomography (CT) and PET in one single gantry system known as PET-CT. Due to various reasons, not least because of the simplification of the clinical protocol, PET-CT procedures integrate both methods in one scanner. Thereby the patient gets two examinations in one procedure and the images containing the information of PET and CT are co-registered. PET- and CT images get overlaid by the use of digital image processing software in order to assign enrichments that are depicted in PET-images to anatomical structures shown in CT-images.

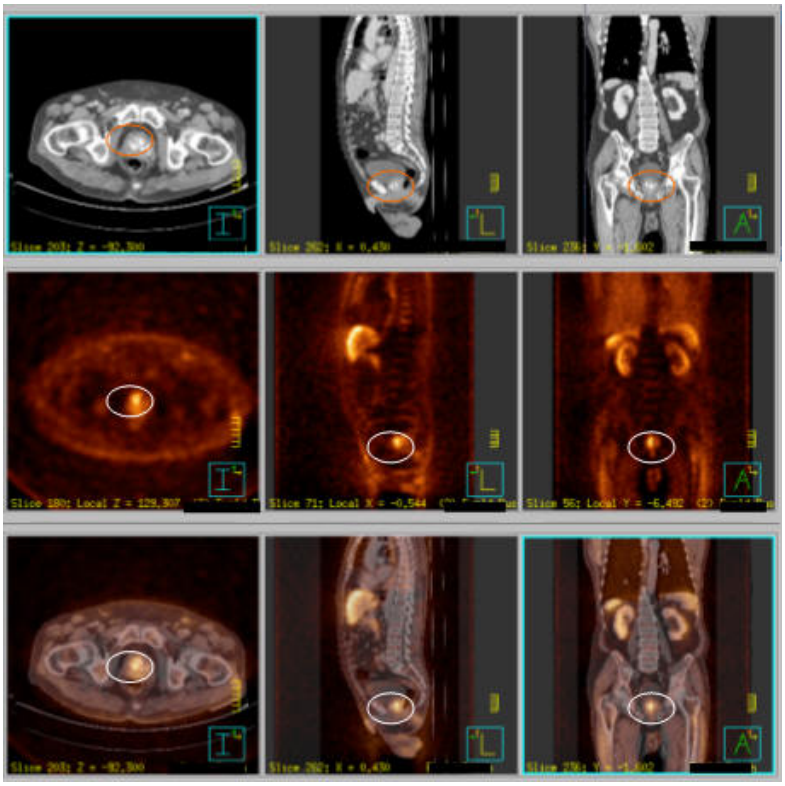

Figure 2.6: PET-CT image: The 1st row depicts the CT-, the 2nd the PET- and the 3rd the co-registered image. The high uptake of the ^{11}C-Choline tracer in cancerous tissue seen in the PET image (the glowing spot within the ellipse) can be allocated within the prostate depicted in the CT image by co-registration of the images. From Ref. [12].

Today PET-CT is one of the most important imaging techniques applied at patients with malign tumors or other diseases. In order to pinpoint the location of

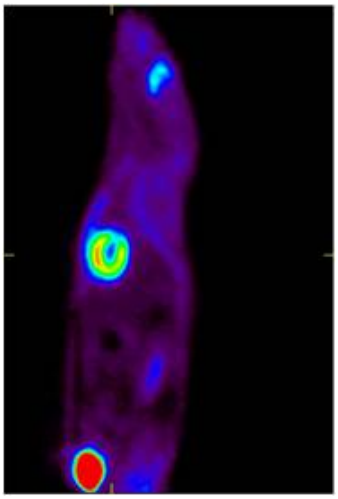

Figure 2.7: Mouse depicted by microPET. Enrichments can be seen in myocardium and bladder.

tumors precisely highly qualitative anatomic information is necessary . PET isn't suitable for this task whereas CT is the best choice. Depending on the situation CT-exams uses radiocontrast agents, e.g. for the imaging of the colon or tissue structures. Metabolic imaging with PET on the other side depicts the uptake of sugar in various body regions. Since malign tumors have a high consumption of sugar they can be found accurately with FDG-PET (see figure 2.6). After the therapy the decrease in consumption is one of the first indicators for the success of the therapy which makes PET often be used for therapy control. Furthermore Co-registered PET-CT images are essential for treatment planning systems in targeted radionuclide therapy (TRT) as discussed in section 2.2.

microPET

A microPET, also referred to as Animal PET, employs the technology of PET to the imaging of small animals like mouse, rat or hamster (see figure 2.7). One of the major fields of applications is pharmacology, where in pre-clinical studies the biodistribution of a new drug can be studied in vivo. The respective drug is radiolabeled and parameters like concentration in certain tissues, speed of elimination or possible penetration of the blood-brain barrier is studied by means of microPET imaging [13].

With regard to detailed literature about PET and PET-CT *PET: physics, instrumentation, and scanners* by Phelps [14] and *Hybrid PET/CT and SPECT/CT Imaging: A Teaching File* by Delbeke and Israel [15] is suggested at this point.

2.2 Therapeutic applications

In the last half century much effort has been put in the development of therapies employing radioactive agents. The principle of fighting malignant tissue with unsealed radioactive sources differs from the long established types of radiotherapy using an external beam. Teletherapy uses photon- or electron beams originating from linear accelerator (LINACs) or sealed radioactive sources (e.g. telecobalt) to irradiate the patient from a distance. Brachytherapy also makes use of sealed radioactive sources but places them inside or next to the target tissue. For example interstitial brachytherapy consist of small radioactive rods, called "seeds", being implanted directly into the tumor as done in the case of prostate cancer treatment. Intracavitary brachytherapy on the other hand places sources inside a pre-existing body cavity for a specific amount of time, e.g. in the case of cervical cancer.

As opposed to this the principle of using a radioactive agent in a therapeutic application in nuclear medicine involves the application of a compound labeled with a radionuclide which preferable enriches in malignant tissue. In the majority of cases the form of the application is an intravenous injection but there are also different ways like oral [16] and intraperitoneal administration [17, 18] as well as direct injection into brain tumor sites [19]. Since the range of particles used for this kind of therapy (cf. subsection 2.2.2) in human tissue is in the order of tenths of millimeters up to centimeters, high doses can be achieved in locations where the tracers concentrate, i.e. the cancerous tissue, whereas a much lower dose is to be expected in the surrounding tissue. Especially in the case of small tumors and disseminated malignancy therapy with radioactive tracers has an advantage towards irradiation with external beams because of the later's incapacity to target a large amount of small metastases.

2.2.1 Tumor-targeting agents

The mother of all therapeutic application protocols in nuclear medicine is the oral application of $Na^{+}\ ^{131}I^{-}$ as postsurgery treatment of different types of thyroid cancer [16]. A lot of research has been put into monoclonal antibodies as tumor targeting vehicles which coined the term radioimmunotherapy (RIT). However more recently the focus has shifted to biochemical molecules like peptides or liposomes as delivery agents, so that the term targeted radionuclide therapy (TRT) became the hypernym for all therapies employing unsealed radioactive compounds. Table 2.1 gives a partial overview of tumor-targeting agents.

Agent	Molecular weight (Da) or physical size	Application [Reference]
NaI	154 Da	Thyroid cancer
MIBG	130 Da	Neuroendocrine tumors [20]
Octreotides	100 Da	Neuroendocrine tumors [21]
SHALs	<2 kDa	Lymphoma [22]
Nucleotides	10 kDa	Solid tumors [23]
Antibodies	25 - 150 kDa	Lymphomas, solid tumors [24]
Liposomes	100 nm	Solid tumors [25]
Nanoparticles	10 nm	Solid tumors [26]
Morpholinos	2 kDa	Solid tumors [27]
Spheres	30 μm	Hepatic lesions [28, 29]

Table 2.1: Tumor-targeting agents. Table adopted and modified from [30].

2.2.2 Types of emitters

Since in TRT the tracer preferably is absorbed in tumor tissue and therefore enables the application of doses from a very close distance the desired range of emitted particles is in the order of the tumor's expansion. Consequently nuclides with high γ-contributions are disadvantageous since they cause a high dose outside the tumor tissue and moreover to the whole body. Because of iodine's natural cumulation in the thyroid its respective isotopes were among the first to be administered for therapeutic protocols and are still widely used as for example ^{131}I, a β^--emitter with a tolerable γ-contribution. β^--emitters in general are the most common choice for TRT but more recently attention also has been given to nuclides emitting Auger electrons, α-particles and conversion electrons (CE) . Unlike β^--emitters these nuclides emit monoenergetic radiation. An overview of radionuclides employed in TRT is given in table 2.2.

Labeling of the carrier molecule isn't restricted to one radionuclide only. A study co-authored by the author of this thesis proved the usage of a radionuclide cocktail, i.e. the labeling with two β^- nuclides of the same element with differing range of their respective spectra very effective in the case of disseminated malignancy [42].

Radionuclide	Emission type relevant for TRT	Energy [keV]	Half life	Reference
^{131}I	β^-	182	8.0 d	[31]
^{90}Y	β^-	934	64.0 h	[32]
^{32}P	β^-	695	14.3 d	[17]
^{33}P	β^-	76	25.3 d	[33]
^{67}Cu	β^-	141	61.8 h	[34]
^{64}Cu	β^- and β^+	β^-: 191 β^+: 278	12.7 h	[35]
^{89}Sr	β^-	585	50.5 d	[36]
^{186}Re	β^-	347	3.7 d	[37]
^{188}Re	β^-	763	17.0 h	[37]
^{177}Lu	β^-	134	6.7 d	[38]
^{153}Sm	β^-	224	46.5 h d	[39]
^{103m}Rh	Auger and CE	Auger: 3 CE: 35	56.1 min	[38]
^{111}In	Auger and CE	Auger: 5 CE: 512	2.8 d	[40]
^{125}I	Auger and CE	Auger: 5 CE: 8	60.0 d	[40]
^{211}At	α	6789†	7.2 h	[41]
^{212}Bi	α and β^-	α: 7737$^\pm$ β: 695*	1.0 h	[41]
^{213}Bi	α and β^-	α: 8814$^\odot$ β: 440$^\boxplus$	45.6 min	[41]

† including the α-particle of daughter nuclide ^{211}Po and neglecting the electron capture contributions of ^{211}At and the β-contribution of ^{207}Bi respectively
$^\pm$ including the α-particle of daughter nuclide ^{212}Po
* including the β-contribution of daughter nuclide ^{208}Tl
$^\odot$ including the α-contribution of daughter nuclide ^{213}Po
$^\boxplus$ including the β-contribution of daughter nuclide ^{209}Tl

Table 2.2: Radionuclides applied in TRT. The cited energy is the average β-energy or the weighted mean of monoenergetic particles respectively.

2.2.3 Treatment planning in TRT

The steady development in external beam therapy and brachytherapy proofed the importance of planning a treatment on the basis of the patient's individual anatomy. Advanced computer-based, patient-specific dose calculations are still not available yet for TRT but recent developments offer potential for developing TRT dose calculation systems similar to those available for conventional radiotherapy treatment planning.

The obvious difficulty in designing algorithms for an internal emitter aiming for patient specific dosimetry is the fact that the source is inside the human tissue and distributed according to biochemical processes which are not controllable by changing geometrical and/or dosimetric parameters as done in Tele- or Brachytherapy where for example beam geometry, location of the seed, exposure time and therefore the source itself can be manipulated. This means that, whereas the patient's anatomical data still is provided by CT the activity distribution within the body has to be determined by PET. The increasing development of combined PET-CT devices makes a combination of both outputs desirable. In fact the fusion of PET and CT Images proved to be a quantum leap in the diagnosis of cancer, especially small metastases, and has a major impact on treatment decisions [43]. Another development which supports treatment planning in TRT is often referred to as "β - couples" and is subject of numerous studies: Works with ^{124}I / ^{131}I - couples [44] have been performed as well as numerous studies using ^{86}Y / ^{90}Y [46]. The nuclide used for planning has to be a β^+ emitter (e.g. ^{86}Y) since it will be administered for the PET-scan. Performing several scans over a longer period provides the medical physicist with time-activity curves of the source organs (cf. section 3.1). With the help of numerical methods this information can be turned into a biokinetic model with individual biological transfer constants. One can couple the nuclide used for therapy to the same molecular structure as the nuclide for planning, because it is the same element and therefore has the same chemical properties (e.g. ^{90}Y). But that also means that one can expect the same bio-distributional behavior. Hence it is possible to use the calculated biokinetic model which was determined by a PET-scan with low activity to calculate the spatial and temporal activity distribution of the therapeutic nuclide.

Furthermore, the anatomical information of the organ containing the tumor, which comes from CT-scans and the information about the activity distribution from the PET-scans combined in a corresponding interface enables a medical physicist to perform a dose calculation in the tumor and the surrounding tissue via numerical or analytical simulation of the radiation transport. In this way treatment planning can be performed, similar as it is done already in external beam therapy. This was first described in [47] and later improved in [48].

An excellent overview about the state of the art and the potentials of PET and

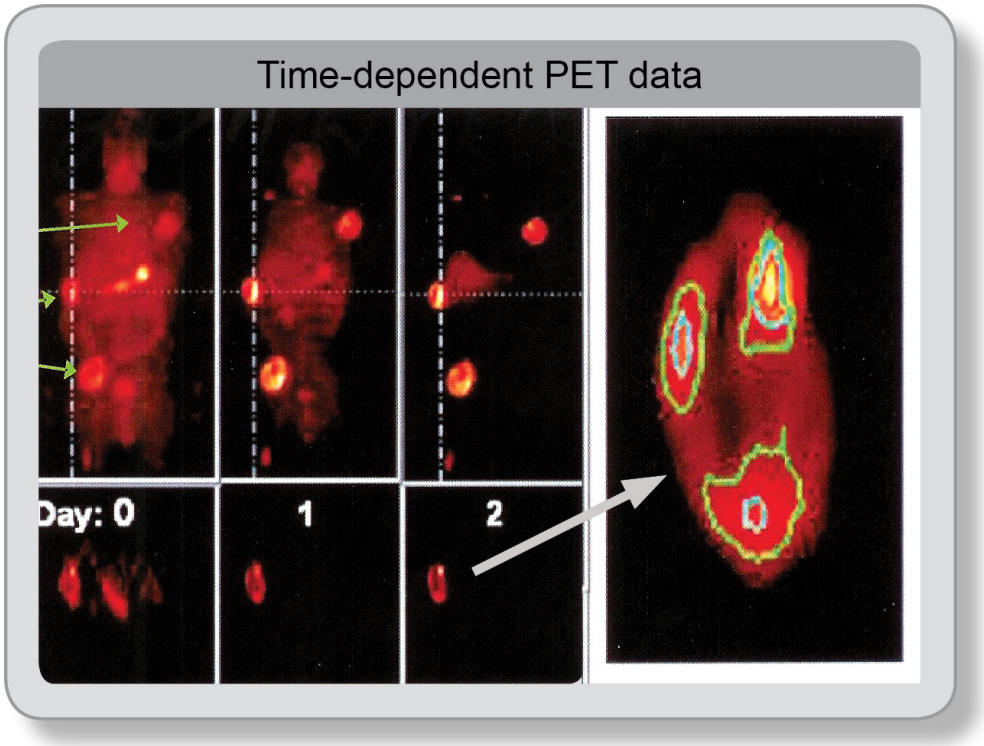

Figure 2.8: PET-based patient-specific dosimetry with β - couple ^{124}I / ^{131}I, adopted and modified version, original published in [44] and [45].

SPECT on dosimetry for TRT can be found in the article of Flux and co-workers [45]. In volumes big compared to their spatial resolution, PET as well as SPECT offer the possibility to determine a heterogeneous uptake of radiopharmaceuticals within the tumor tissue which then is used for dosimetric calculations. The work of Sgourous and co-workers [44] gives an impressing look on the potentials of a 3D dose planning. (see figure 2.8).

Chapter 3

Dosimetry in Nuclear Medicine

3.1 The MIRD-System

Before discussing in detail the dosimetry model used in Nuclear Medicine the most relevant dosimetric quantities are introduced. The **absorbed dose** D is the energy deposited by ionizing radiation per unit mass of a material.

$$D = \frac{dW}{dm}. \tag{3.1}$$

For its unit called Gray [Gy] it follows that 1 Gy = 1 J/kg. A very common quantity derived from the absorbed dose is the **equivalent dose** H_T to an organ or tissue T which takes into account the different linear energy transfer (LET) of different types of radiation, i.e. the particles' energy loss per unit distance. The LET has a considerable impact on the biological effect of irradiated tissue and is reflected in the use of radiation weighting factors w_R. The definition of the equivalent dose to a tissue T therefore is:

$$H_T = w_R \cdot D_T, \tag{3.2}$$

with D_T as the absorbed dose to T. The weighting factors for the respective radiation types are dimensionless since they represent the relative biological effectiveness compared to γ-radiation. Their values are determined by the International Commission on Radiological Protection (ICRP) and were last updated in ICRP Publication 103 [49]. For γ- and β - radiation $w_R = 1$ whereas for α - particles $w_R = 20$. The unit for the equivalent dose is 1 Sievert [Sv] = 1 J/kg.

The physical and mathematical methodology to calculate the absorbed dose to individual organs and the whole body due to the administration of radiopharmaceuticals is known as the **MIRD system** and has been developed by the Medical Internal Radiation Dose (MIRD) Committee of The Society of Nuclear Medicine

since the late 60s. A detailed description is provided in *MIRD Primer for Absorbed Dose Calculations* [50] and a very good essay about its history can be found in the article of Micheal Stabin [51].

The basic principle of the MIRD system is the classification into source- and target organs. Any organ can be a target for the radiation emitted by the radiopharmaceutical compound as long as it's within the range of the particle in question. That implies of course that the presence of a γ-emitter within the human body makes the organs in their entirety to targets because of the penetrating properties of photon irradiation. Source organs on the other hand denote the tissues or organs that have a radioactive uptake, i.e. enrich with the radiolabeled tracer. One has to stress at this point that a certain fraction of the tracer will be distributed more or less homogeneously throughout the body due to its transportation via the circulatory system. A tissue is classified as source organ if it shows a specific uptake which is noticeably higher than the nonspecific uptake in the rest of the body [30]. In clinical situations Regions of Interest (ROI) are drawn on the respective nuclear image to identify the source organs. In the MIRD System the irradiation to a target organ is determined by summing up the contributions from all source organs (see figure 3.1).

Since both internal organs (e.g. lung, liver) as well as tissues (e.g. red marrow) enrich with radioactive material the more general term "'source region", respectively "'target region" are used from now on. Furthermore the standardized nomenclature of MIRD Pamphlet No. 21 [52] is used. According to the MIRD system the absorbed dose $D(r_T, T_D)$ to a target region r_T over dose-integration period T_D is:

$$D(r_T, T_D) = \sum_{r_S} \tilde{A}(r_S, T_D) S(r_T \leftarrow r_S). \tag{3.3}$$

r_S denotes the source region, thereby summing up the contributions. This way internal dose calculations are broken down to two essential quantities, the time-integrated activity in source regions $\tilde{A}(r_S, T_D)$ over dose-integration period T_D which is commonly known as the cumulated activity, the term used from now on, and the so called S-value $S(r_T \leftarrow r_S)$ that refers to a specific pair of source- and target region.

Let's first investigate the origin of the cumulated activity $\tilde{A}(r_S, T_D)$. Mathematically it is the integral over a time period T_D of a given time-activity curve (TAC) $A(r_S, t)$ in a source region, thus

$$\tilde{A}(r_S, T_D) = \int_0^{T_D} A(r_S, t) dt. \tag{3.4}$$

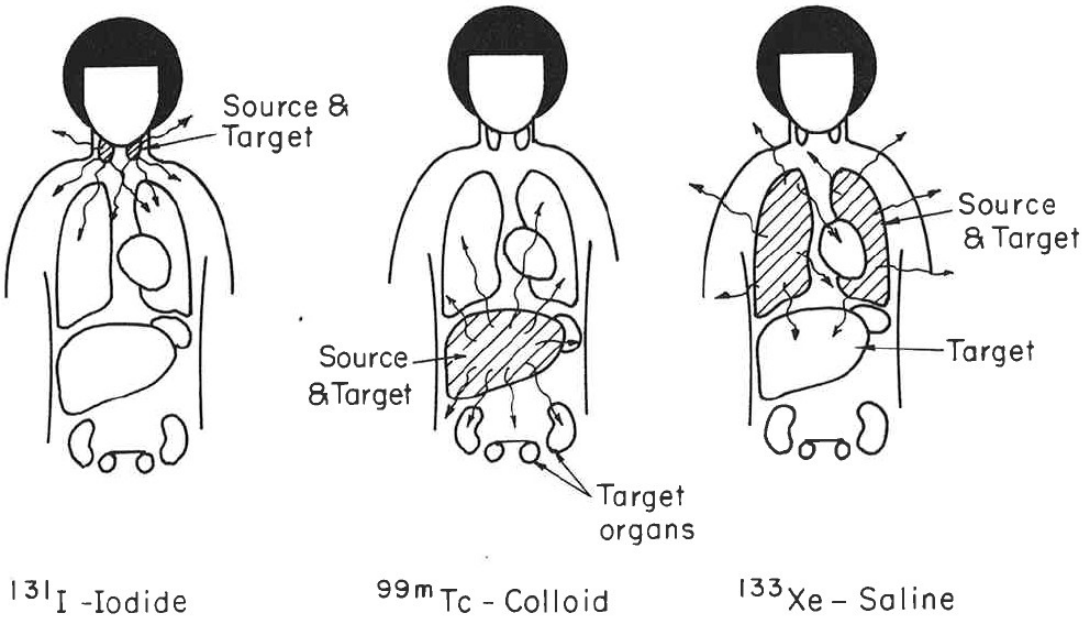

Figure 3.1: Concept of source and target organ as depicted in the MIRD Primer [50]. The source organs for the respective tracer, i.e. the tissue where the major accumulation occurs are (from left to right) thyroid, liver and lung. Because of self irradiation these organs are also target organs.

For radiation protection reasons the radionuclides used in Nuclear Medicine have a sufficiently short half live which is why it's feasible to set $T_D \to \infty$ and therefore let $\tilde{A}(r_S, T_D)$ be the total number of nuclear disintegrations taking place in the source region after the time of application. Since the temporal behavior of the activity in a source $A(r_S, t)$ has the unit s^{-1}, $\tilde{A}(r_S, T_D)$ as its integral over time is dimensionless.

A quantity often referred to in Nuclear Medicine is the time-integrated activity coefficient $\tilde{a}(r_S, T_D)$ for a source region r_S, better known as residence time and defined as

$$\tilde{a}(r_S, T_D) = \frac{\tilde{A}(r_S, T_D)}{A_0} \tag{3.5}$$

where A_0 is the total activity administered to the patient. The division of a dimensionless quantity by an activity gives $\tilde{a}(r_S, T_D)$ the unit of time. In clinical practice $\tilde{A}(r_S, T_D)$ for a specific source region is determined by a sequential PET- or SPECT scan yielding the temporal progress of the TAC (see figure 3.2). The area underneath the TAC corresponds to $\tilde{A}(r_S, T_D)$ (see figure 3.3). The TAC

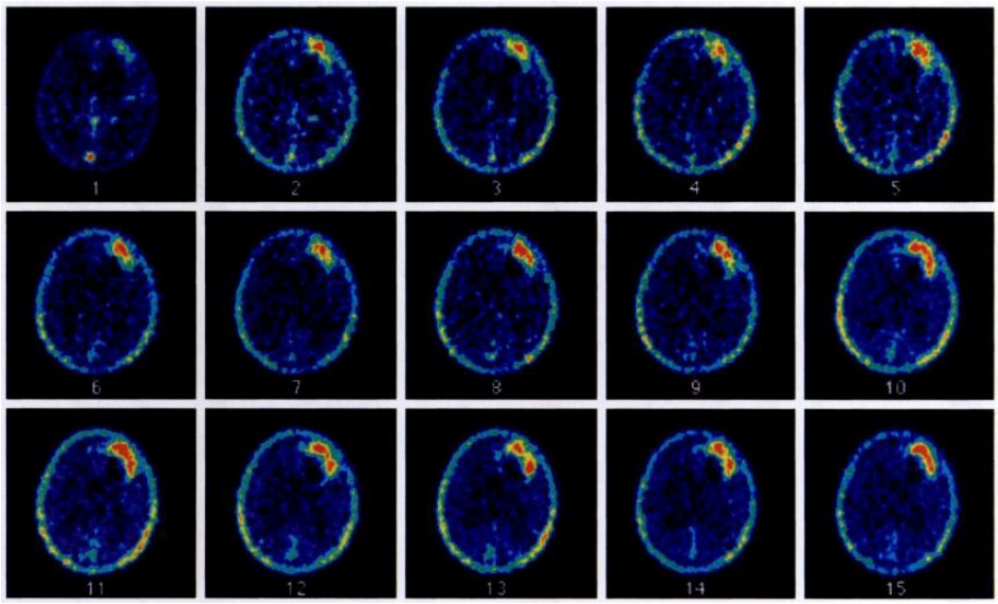

Figure 3.2: Sequential PET-scan of the brain showing the chronology of the tumor's uptake in the frontal lobes. Published in Ref. [53].

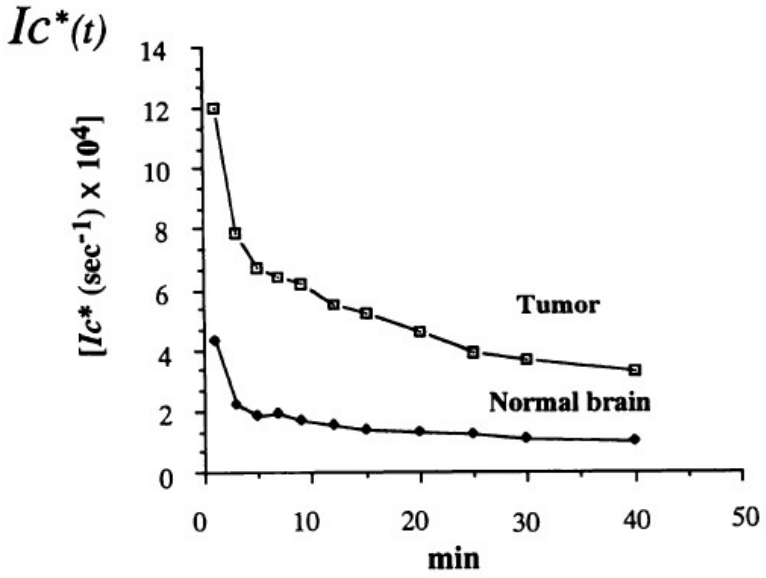

Figure 3.3: TAC for brain tissue and tumor corresponding to figure 3.2. Published in Ref. [53].

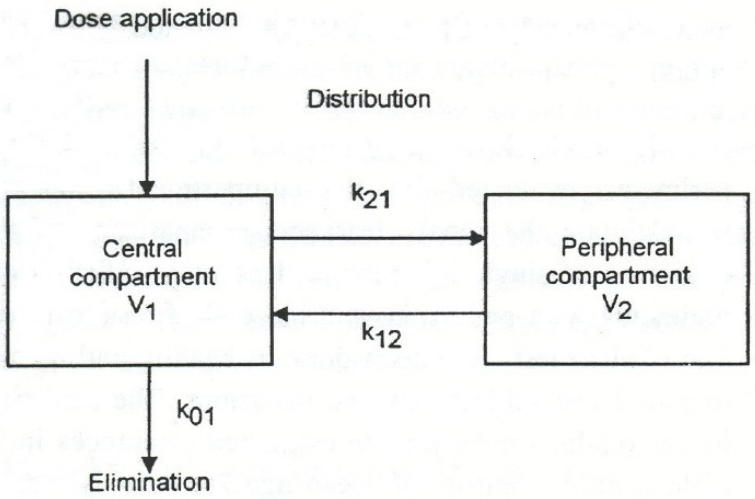

Figure 3.4: Compartment model

is crucially dependent on the radionuclides physical half life $T_{1/2_{\text{phys}}}$ which is the amount of time it takes for half the number of nuclides to undergo radioactive decay as well as the compound's biological half life $T_{1/2_{\text{biol}}}$ that refers to the time it takes for half of the amount of the tracer to get removed from the corresponding source region by means of biological transport. The effective half life $T_{1/2_{\text{eff}}}$ contains both effects and therefore describes the amount of time it takes to remove half the activity from a source region, either by radioactive decay or biological transport. Its definitions is:

$$\frac{1}{T_{1/2_{\text{eff}}}} = \frac{1}{T_{1/2_{\text{phys}}}} + \frac{1}{T_{1/2_{\text{biol}}}} \tag{3.6}$$

A purely phenomenological approach to calculate a source region's $\tilde{A}(r_S, T_D)$ is the application of a numerical fit, using multi-exponential functions in most of the cases. A more generic way to describe the distribution of a tracer within the human body is the concept of **compartment models**. There, every region of the body where the activity distribution is considered to be homogeneous forms a compartment with transfer routes to other compartments. A simple model with two compartments is shown in figure 3.4. The tracer gets injected into the central compartment (e.g. blood circulation) where part of it transfers to the peripheral compartment (e.g. a specific organ) and back whereas at the same time it gets eliminated from the body. In many cases of pharmacokinetics the flux of material between compartments is assumed to be linear which is referred to as first order

kinetics, hence

$$R_{ij}(Q_j) = k_{ij}Q_j, \quad k_{ij} = \text{const.} \tag{3.7}$$

or in the differential form:

$$\frac{dQ_j}{dt} = k_{ij}Q_j \tag{3.8}$$

with

Q_j	quantity of material in compartment j
R_{ij}	flux of material into compartment i from compartment j
k_{ij}	biological transfer constant for the flux of material into compartment i from compartment j

Adapted to the compartment model above (figure 3.4) the notation yields following system of equations:

$$\begin{aligned} \frac{dQ_1}{dt} &= f(t) - (k_{21} + k_{01})Q_1 + k_{12}Q_2 \\ \frac{dQ_2}{dt} &= -k_{12}Q_2 + k_{21}Q_1 \end{aligned} \tag{3.9}$$

$f(t)$ is the input strategy as function of time, i.e. mathematically describes the form of application. In case of a bolus injection usually a immediate uptake is assumed and $f(t)$ is set to 0.

In nuclear medicine the quantity of material Q_j in a compartment is not as interesting as the activity A_j, since the later determines the nuclear transitions per time. The radioactive decay follows the decay law with λ_p as physical decay constant of the respective nuclide:

$$\frac{dA}{dt} = -\lambda_p A \tag{3.10}$$

Since this relation is mathematical equivalent to equation 3.8 the change in time of the compartments' activities can be described as follows:

$$\begin{aligned} \frac{dA_1}{dt} &= -(k_{21} + k_{01})A_1 + k_{12}A_2 - \lambda_p A_1 \\ \frac{dA_2}{dt} &= -k_{12}A_2 + k_{21}A_1 - \lambda_p A_2 \end{aligned} \tag{3.11}$$

More generally the activity A_j in compartment j connected to n-1 other compartments can be expressed like this:

$$\frac{dA_j(t)}{dt} = - \sum_{\substack{i=1,\\ i\neq j}}^{n} k_{ij}A_j(t) + \sum_{\substack{i=1,\\ i\neq j}}^{n} k_{ji}A_i(t) - \lambda_p A_j(t) \tag{3.12}$$

$A_j(t)$	activity dependent on the time t elapsed since application
k_{ij}	biological transfer constant from compartment j to i
k_{ji}	biological transfer constant from compartment i to j
λ_p	physical decay constant of radionuclide

If a compartment model consists of n compartments this results in a system of n coupled differential equations:

$$\frac{d\vec{A}}{dt} = M\vec{A} \tag{3.13}$$

with

$$\frac{d\vec{A}}{dt} = \begin{pmatrix} \frac{dA_1(t)}{dt} \\ \vdots \\ \frac{dA_n(t)}{dt} \end{pmatrix} \quad \text{and} \quad \vec{A} = \begin{pmatrix} A_1(t) \\ \vdots \\ A_n(t) \end{pmatrix} \tag{3.14}$$

as well as:

$$\mathrm{M} = \begin{pmatrix} -\left(\sum_{\substack{j=1,\\ j\neq 1}}^{n} k_{j1} + \lambda_p\right) & k_{12} & \dots & k_{1n} \\ k_{21} & \ddots & \dots & \vdots \\ \vdots & \dots & \ddots & \vdots \\ k_{n1} & \dots & \dots & -\left(\sum_{\substack{j=1,\\ j\neq n}}^{n} k_{jn} + \lambda_p\right) \end{pmatrix} \tag{3.15}$$

A system of ordinary differential equations normally is solved by means of computational methods, such as searching the eigenvalues and eigenvectors for M [54] or by means of a series expansion [55]. This yields $A_1(t) \dots A_n(t)$ and respective integration the cumulated activities in each compartment $\tilde{A}_1 \dots \tilde{A}_n$.

The second essential quantity from equation 3.3 is the S-value $S(r_T \leftarrow r_S)$, given as:

$$S(r_T \leftarrow r_S) = \frac{1}{M(r_T)} \sum_i E_i \, Y_i \, \phi(r_T \leftarrow r_S, E_i), \tag{3.16}$$

with

E_i	mean energy of the i$^{\text{th}}$ nuclear transition
Y_i	number of the i$^{\text{th}}$ nuclear transitions per nuclear transformation
$\phi(r_T \leftarrow r_S, E_i)$	the absorbed fraction (AF) , i.e. the fraction of radiation energy E_i emitted within the source region r_S that is absorbed in the target region r_T
$M(r_T)$	mass of the target region r_T

E_i and Y_i are specified by the nuclear decay data of the respective radionuclide whereas $\phi(r_T \leftarrow r_S, E_i)$ depends on the type of radiation, the tissue composition as well as size and spatial relationship of r_S and r_T. The later is defined by the computational phantom used to determine $\phi(r_T \leftarrow r_S, E_i)$, see the next section (3.2). Looking upon the different types of radiation that occur in medical applications (see chapter 2) one can make the following distinction regarding $\phi(r_T \leftarrow r_S, E_i)$:

- $\boldsymbol{\alpha}$-radiation: Because of the small range of α-particles which in human tissue is in the order of microns (10^{-6} m) $\phi(r_T \leftarrow r_S, E_i) = 1$, i.e. the entire energy is absorbed within the source region r_S.
- $\boldsymbol{\beta}$-radiation: For the majority of source regions the assumptions above also applies to β-particles, hence $\phi(r_T \leftarrow r_S, E_i) = 1$. However for walled organs like urinary bladder, stomach or intestines following dose assessment is applied in internal dose calculations: The absorbed dose to the organ wall due to β-radiation from the organ contents is one half of the absorbed dose

to the contents [56]. For the self-irradiation of the organ contents again $\phi(r_T \leftarrow r_S, E_i) = 1$ applies. Another exception concerns the skeletal components like red marrow or compact bone. When being source regions of β-particles their respective AFs are functions of the particle's energy and were determined in the work of Eckerman and Stabin [57].

- $\boldsymbol{\gamma}$-radiation: The penetrating nature of γ-radiation makes simple assessments for $\phi(r_T \leftarrow r_S, E_i)$ like above impossible. The self-irradiation of a γ-emitting source region as well as the cross-irradiation to other target regions has to be calculated using Monte Carlo simulations and body phantoms. The next section (3.2) will discuss this issue in detail.

When applying the MIRD-system to a real scenario equation 3.3 has to be slightly modified. This is due to the fact that one usually picks out the organs with a specific uptake, calculates their respective residence times and additionally determines the residence time of the whole body (including also the source regions chosen before). Based on this choice of data the absorbed dose coefficient $d(r_T, T_D)$, i.e. the absorbed dose to a target region r_T per unit administered activity then can be expressed as [58, 59]:

$$\begin{aligned} d(r_T, T_D) &= \sum_{r_S} \tilde{a}(r_S, T_D) S(r_T \leftarrow r_S) + \tilde{a}(r_{REM}, T_D) \\ &\quad \times \left(\frac{M(r_{TB}) S(r_T \leftarrow r_{TB}) - \sum_{r_S} M(r_S) S(r_T \leftarrow r_S)}{M(r_{REM})} \right). \end{aligned} \tag{3.17}$$

TB and *REM* stand for "total body" and "remaining tissue" respectively. Furthermore

$$M(r_{REM}) = M(r_{TB}) - \sum_{r_S} M(r_S), \tag{3.18}$$

and

$$\tilde{a}(r_{REM}, T_D) = \tilde{a}(r_{TB}, T_D) - \sum_{r_S} \tilde{a}(r_S, T_D), \tag{3.19}$$

with $M(r_S)$ as the mass of the source region.
Finally as an estimate for the total radiation burden it is possible to calculate the so called effective dose E which constitutes itself as the sum of the weighted equivalent doses of the organs and tissues.

$$E = \sum_T w_T H(r_T, T_D). \tag{3.20}$$

The corresponding weighting factors w_T take into account the organs' different radiosensitivities and are published by the ICRP [60, 49]. In order to calculate the equivalent dose $H(r_T, T_D)$ to target region r_T from the absorbed dose $D(r_T, T_D)$ one simply has to apply relation 3.2.

3.2 Absorbed Fractions and Phantoms

As discussed in the previous section one of the essential quantities included in the S-value $S(r_T \leftarrow r_S)$ is the absorbed fraction (AF) $\phi(r_T \leftarrow r_S, E_i)$ for γ-photons. Another term cited very often is the specific absorbed fraction (SAF) $\Phi(r_T \leftarrow r_S, E_i)$ that represents the AF per unit mass of the target region

$$\Phi(r_T \leftarrow r_S, E_i) = \frac{\phi(r_T \leftarrow r_S, E_i)}{M(r_t)}, \tag{3.21}$$

and has the SI unit kg^{-1}. The way to determine AFs and SAFs leads to the concept of Monte Carlo Simulations of radiation transport phenomena. This mathematical technique is based on the concept of sampling individual trajectories of charged and uncharged particles and described in detail in section 4.1.

The input for the Monte Carlo simulation, i.e. the particular geometrical and physical setup is determined by the used computational body model, also called **phantom** which not only specifies the masses of organs and tissues but also their spatial extensions, elemental compositions and geometrical arrangements. In the following a brief history of phantoms used for dose assessment in Nuclear Medicine is presented.

Snyder et al. published the first S-values in the mid-1970s [61], which are based on SAFs calculated previously [62]. A mathematical phantom was introduced that describes the human body via simple geometric forms, such as cones and ellipsoids (see figure 3.5) Cristy and Eckerman at Oak Ridge National Laboratory (ORNL) further designed mathematical phantoms representing adults and children at ages 1, 5, 10, and 15 years as well as a newborn model. Values of SAFs were calculated for internal photon emitters for each of the ORNL series of phantoms [63]. Finally, Stabin and co-workers completed a series of phantoms representing the pregnant and nonpregnant adult female [64]. A more sophisticated way to model the human body is demonstrated by voxel phantoms. They are based on photographic images of dissected bodies, as well as computed tomographic or magnetic resonance (MR) tomographic data of real persons to provide a three-dimensional representation of the human body. Various institutions constructed voxel models from the early

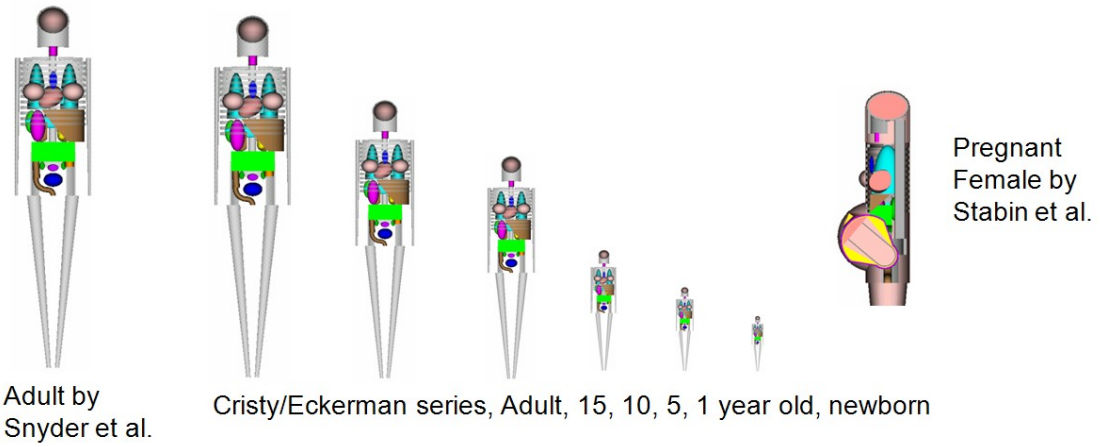

Figure 3.5: Mathematical phantoms.

1990s onward, for example, the GSF (National Research Center for Environment and Health) in Munich, where a whole family of voxel models was created (see figure 3.6), [65, 66, 67, 56] or Yale University, where Zubal developed a head and torso phantom, [68, 69] just to name a few. Likewise, Monte Carlo calculations yielded SAFs for different energies and organ pairs, with the voxel representation allowing the estimation of doses to be based on a much more realistic model [59]. The third and most advanced generation of phantom technology is represented by NURBS-based hybrid phantoms (see figure 3.7), which use nonuniform rational B-spline (NURBS) or polygon mesh surfaces to define body and organ topology [71, 72, 73, 70]. They combine the voxel phantoms anatomic realism and spatial fine resolution with the ability to resculpt presegmented hybrid phantoms in order to match individual patient body morphometry. Monte Carlo calculations performed with hybrid phantoms for the purpose of the determination of SAFs for nuclear medicine dosimetry haven't been realized yet.

3.3 State of the art and motivation of work

3.3.1 State of the art

In daily clinical practice, dose-assessment software is utilized, the widest spread being OLINDA/EXM (Organ Level INternal Dose Assessment with EXponential Modeling). This code was launched originally in 1984 as MIRDOSE 1 [74]

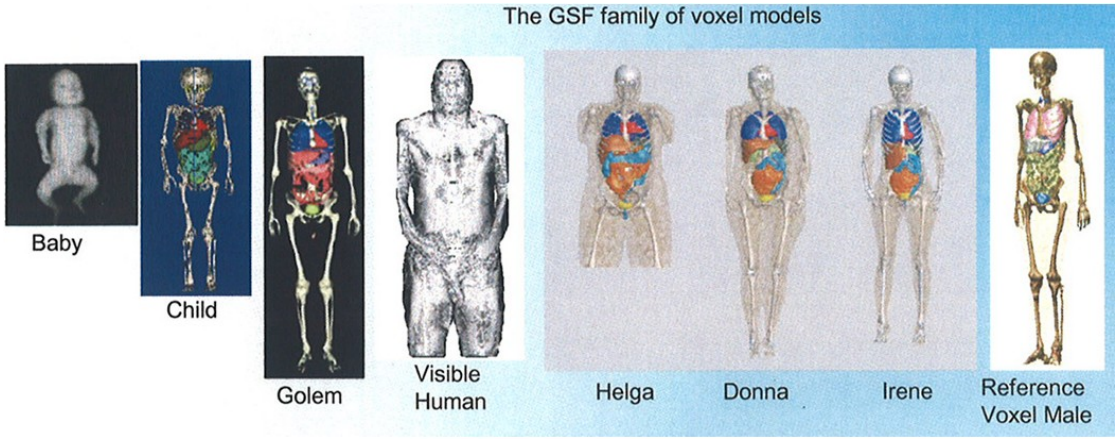

Figure 3.6: GSF "family" of voxel phantoms.

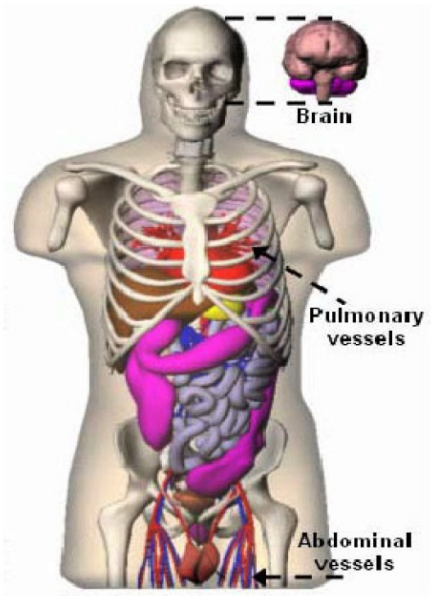

Figure 3.7: NURBS-based adult male model. Published in [51] and [70].

and marked the start of a series until MIRDOSE 3.1 [75]. Finally its programmer, Michael Stabin rewrote the whole code using the Java programming language, renamed it OLINDA/EXM [76] and got it approved by the U.S. Food and Drug Administration (FDA) . Independently of its version, MIRDOSE and later OLINDA/EXM have been widely used in clinical protocols, trials, pre-clinical studies as well as a tool for teaching internal dosimetry in universities and professional training centers for over 25 years. There is hardly any alternative software that deals specifically with the calculation of dose to individual organs as well as the whole body resulting from the administration of radiopharmaceuticals. However MABDOSE [77, 78] should be mentioned at this point although its dissemination is small compared to the MIRDOSE series.

OLINDA/EXM (as wells as MABDOSE) uses S-values in its calculation that are based on SAFs derived from the ORNL stylized phantoms by Cristy and Eckerman (see page 36). Given the huge amount of variations in individual anatomy and the known dependence of the SAF on the organs' size and spatial relationship, the limitation of using a total amount of seven mathematical phantoms (not counting the models for different stages of pregnancy) representing the total population like done by OLINDA/EXM becomes obvious. There exist a fair amount of approaches how to implement more patient-individualized models for dose calculations:

1. **MIRD 11 guidance:**
   OLINDA/EXM itself allows corrections for patient-specific organ masses [76]. The respective mathematical relations origin in recommendations formulated in MIRD pamphlet No. 11 [61] and can be summarized like this: (in this context the index ρ represents the reference phantom whereas χ stands for the individual patient)

   - Since in the case of α- and β-particles $\phi(r_T \leftarrow r_S, E_i) = 1$ the SAF varies linearly with the mass of the source region:

   $$\phi_{\alpha,\beta}(\chi) = \phi_{\alpha,\beta}(\rho) = 1 \quad \text{and} \quad \Phi_{\alpha,\beta}(\chi) = \left(\frac{M(r_S,\rho)}{M(r_S,\chi)}\right) \Phi_{\alpha,\beta}(\rho). \tag{3.22}$$

   - For organ self-irradiation by photons ($r_T = r_S$) the following approach is suggested:

   $$\phi_\gamma(\chi) = \left(\frac{M(r_S,\chi)}{M(r_S,\rho)}\right)^{\frac{1}{3}} \phi_\gamma(\rho) \quad \text{and} \quad \Phi_\gamma(\chi) = \left(\frac{M(r_S,\chi)}{M(r_S,\rho)}\right)^{\frac{2}{3}} \Phi_\gamma(\rho). \tag{3.23}$$

   - For organ cross-irradiaon by photons ($r_T \neq r_S$) MIRD 11 argues that the SAF should not be scaled with the target region mass $M(r_T)$ since

the AF would increase or decrease with larger or smaller $M(r_T)$ which results in:

$$\phi_\gamma(\chi) = \left(\frac{M(r_T,\chi)}{M(r_T,\rho)}\right)\phi_\gamma(\rho) \quad \text{and} \quad \Phi_\gamma(\chi) = \Phi_\gamma(\rho). \tag{3.24}$$

However this assumption is restricted to the cases where source- and target regions are far apart.

2. **Scaling based on reference voxel phantoms**
One can approximate the patients individual SAFs by interpolation of data sets from stored voxel reference models. Petoussi-Henss and co-workers investigated this issue by analyzing the SAFs for the GSF voxel phantom series (see page 37). The result was that for self-irradiaon relation 3.23 stays valid for photon energies above 100 keV. The only exception is the red bone marrow (RM) where the results are inconclusive. For cross-irradiaon relation 3.24 was validated even for the case of source- and target region being close to each other and for RM. The conclusion was drawn that the organ masses do not account for the observed SAF variability between voxel phantoms but rather the inter-organ distances [79].

3. **Individual hybrid- or voxel phantom of patient**
Of course the most accurate way of determining an individual patient's SAFs is to build them upon the patient's individual anatomy. This requires the segmentation of a whole body CT or MR of the patient, i.e. the construction of the patient's very own hybrid or voxel phantom, assigning every voxel certain properties like the kind of tissue and the density as well as model the organ surfaces in case of hybrid phantoms. This complex data then has to be submitted to a Monte Carlo code in order to calculate the absorbed photon fractions.

4. **Scaling of pre-segmented hybrid phantoms**
Lee and co-workers demonstrated that by defining body and organ surfaces using NURBS or polygon mesh surfaces they can be non-uniformly scaled and thus can be sculpted much more quickly to match individual patient body morphometry without the need to re-segment original CT or MR images [71, 73].

3.3.2 Motivation of work

Approach No. 1 was suggested quite a while ago but eventually was validated by the comparison with SAFs derived from voxel phantoms [79]. Yet the same study indicates that the inter-organ geometry is the main factor influencing the SAFs

rather than the organ masses. However MIRD pamphlet No. 11 does not provide geometry-related correction guidance.

With regard to approach No. 2 it's apparent that it enables the deduction and verification of guidelines for patients-specific scaling. However, the advantage of the much more realistic phantoms is accompanied by the disfavor of limited available numbers of voxel phantoms and the effort in producing new ones as well as performing the respective Monte Carlo simulations.

The third option is clearly impossible at the present state, since it takes months to construct a whole-body voxel- or hybrid phantom. But even under the assumption that in the near or far future software becomes so advanced that automatic segmentation within a reasonable time frame is possible, one still would have to perform a radiation transport calculation in a complex geometric environment. Therefore, the construction of an individual patient's whole-body voxel phantom in nuclear medicine may be questionable for therapeutic applications with higher activities, but as for purely diagnostic applications, the effort is clearly far beyond its use. For the sake of clarity and differentiation, one has to add that the construction of hybrid or voxel models out of *partial* body CT or MR scans can be done in a reasonable amount of time. This is performed in case of therapeutic procedures, such as TRT, for the purpose of treatment planning based on image-based fine resolution dosimetry (see section 2.2.3). Nevertheless this does not replace whole-body dosimetry as a means for assessing the overall radiation burden.

As for the fourth approach one might add that this technology is not yet implemented in clinical software. More precisely the non-uniform scaling of presegmented hybrid phantoms was realized but works on patients-specific SAF are still due.

The most important aspect of the approaches listed above is that they all require the knowledge of the organs' masses, i.e. detailed knowledge of the patient's anatomy in form of a whole body CT or MR. The fact is that in nuclear diagnostics for the majority of applications, accompanying anatomical imaging is neither performed nor justified (e.g., examinations in neurology or cardiology, see chapter 2). So, in the case of the absence of a CT or MR scan of the patient, one has to rely on reference models

Therefore in this thesis the author suggests the use of an *ensemble* of mathematical phantoms and their respective calculated S-values and SAFs to cover the spectrum of human anatomy. In calculations relying on the MIRD schema, one then selects the phantom that matches the patient closest according to physiognomic parameters, such as height and weight (see figure 3.8). As a first step toward such an ensemble, in this thesis the Cristy and Eckerman series was expanded into 21 phantoms and submitted to Monte Carlo simulations. The Cristy and Eckerman data [63] comprised 12 discrete photon energies and 28 source regions. As will

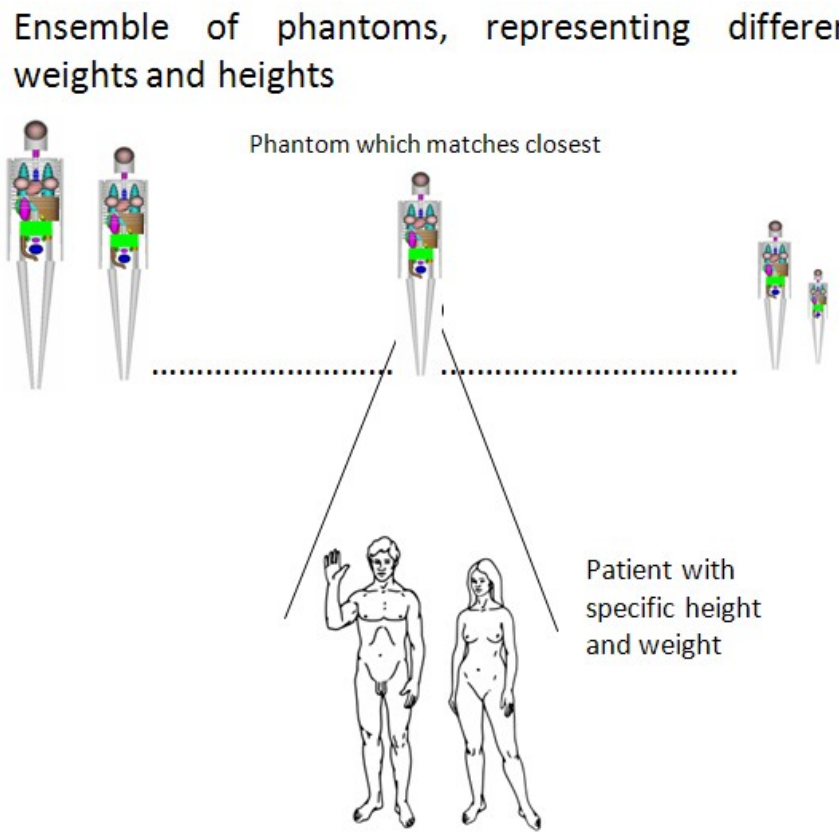

Figure 3.8: Principle of ensemble of mathematical phantoms: The phantom (and therefore the SAFs) which matches closest the patient in weight and height is chosen from the ensemble.

be discussed in section 4.3 for the nominal age groups 1-15 separate simulations of male and female models were performed which results in 36 individual simulations per photon energy and source region. In other words the consideration of the entire energy range spanned by the Cristy and Eckerman series would result in $12 \times 28 \times 36 = 12096$ simulations! This huge amount of calculation work- and time is only feasible if a real chance exists that the ensemble really provides a more patient specific dose assessment.

Therefore this study focuses on one energy line, namely the annihilation radiation of 511 keV which emerges with every PET examination. Moreover the source regions are restricted to the organs and tissue which have a documented specific uptake of ^{18}F-flourodeoxyglucose (^{18}F-FDG), the most common PET-tracer. This reduces the number of simulations to $9 \times 36 = 324$, a manageable amount.

For comparison and validation a full internal dose calculation is performed and compared with results of MIRD Dose Estimate Report No. 19 [80], the ICRP Publication No. 80 [81] and concurrent calculations performed with OLINDA/EXM. Shortly summarized the model calculations can be broken down into following steps:

Monte Carlo simulations of the phantom ensemble
to calculate SAFs for annihilation radiation.

⇓

Calculation of S-values for ^{18}F out of SAFs.

⇓

Dose calculation for the intravenous administration of ^{18}F-FDG,
using the biokinetic data from MIRD Dose Estimate Report No. 19
and the ICRP Publication No. 80.

⇓

Comparison with data from the publications cited above and with
calculations performed with OLINDA/EXM.

If, and only if the usage of ensemble proves to provide a more patient specific dose assessment an extension to other photon energies is feasible.

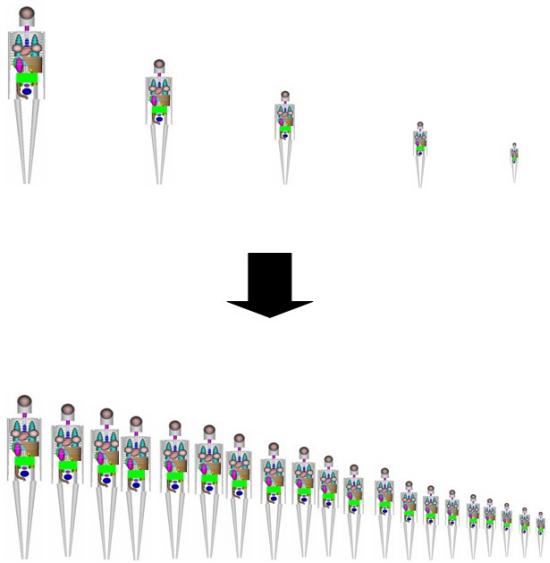

Figure 3.9: Expansion of Cristy and Eckerman into a ensemble of 21 phantoms, representing different age groups.

Chapter 4

Simulation Model

4.1 Principle of Monte Carlo simulation

The first time Monte Carlo simulations were applied was during the "Manhattan project", the secret program during World War II with the aim to develop the atomic bomb. Their purpose was to simulate the expected neutron flux within the bomb. Since the Monte Carlo method relies on statistical sampling based on the selection of random numbers, it resembles gambling in a casino which is why this numerical method was named after the city best known for its casinos, Monte Carlo. Nowadays a huge range of Monte Carlo techniques is utilized in different fields of science, such as radiation transport and nuclear reactions, quantum chromodynamics, stellar evolution, traffic simulation, prediction for the stock exchange market, weather forecast, chip design and many more.

Numerical methods can roughly be categorized into deterministic and stochastic ones, Monte Carlo simulations being part of the later. In order to describe a specific radiation transport phenomena one has to solve the transport- or Boltzmann equation:

$$\begin{aligned} \frac{1}{\nu_i}\frac{\partial \varphi_i}{\partial t} &= \Omega\ grad\ \varphi_i \\ &+ \left[\int d^3\Omega' dE_B \sigma_{ij}(x, E_B \rightarrow E, \Omega \rightarrow \Omega')\varphi_j \right. \\ &- \left. \int d^3\Omega' dE_B \sigma_{ij}(xE \rightarrow E_B, \Omega \rightarrow \Omega')\varphi_j \right] \sigma_i(x, E)\varphi_i \\ &+ \left(\frac{\partial}{\partial E}\varphi_i S\right) - \frac{1}{\lambda_i} + Y_i(x, E, \Omega, t). \end{aligned} \tag{4.1}$$

with

φ_i	angular flux
Ω	unit vector in the particles direction
ν_i	particle velocity
E, E_B	particle energies with $E_B > E$
σ_{ij}	cross section for the production of a particle with a given energy
λ_i	decay probability per unit path length
S	stopping power
Y	term describing particles produced by external sources

A deterministic method to solve it would be the discrete ordinates method that solves the transport equation for the average particle behavior. In contrast stochastic methods like Monte Carlos calculations simulate individual particles and register certain required aspects of their average behavior like energy deposition or flux. The average behavior of particles in the physical system is then deducted from the average behavior of the simulated particles using the central limit theorem that states that the variation of mean values approaches a normal distribution about the true mean with a certain variance that decreases with increasing statistical precision. In this sense a Monte Carlo simulation doesn't literally solve an equation but rather provides physical quantities by simulating particle histories, i.e. actually following each of many particles from a source throughout its life to its death in some terminal category (absorption, escape, etc.). Probability distributions are randomly sampled, using transport data to determine the outcome at each step on its trajectory [82](see figure 4.1).

4.2 Software

In this section the software packages are discussed that were used in the simulation model.

4.2.1 MCNP

As for Monte Carlos codes on radiation transport there is actually quite a range of products. In his review on nuclear medicine dosimetry [51] Stabin mentions MCNP (Monte Carlo N-Particle) [83] or EGS4 [84, 85] as "well-supported radiation transport codes". Nevertheless also GEANT4 [86], FLUKA [87], GEPTS and EGSnrc [88] proved to be suitable for certain applications. Few deterministic solutions with regard to radiation transport simulation exist, one of them being ATTILA [89].

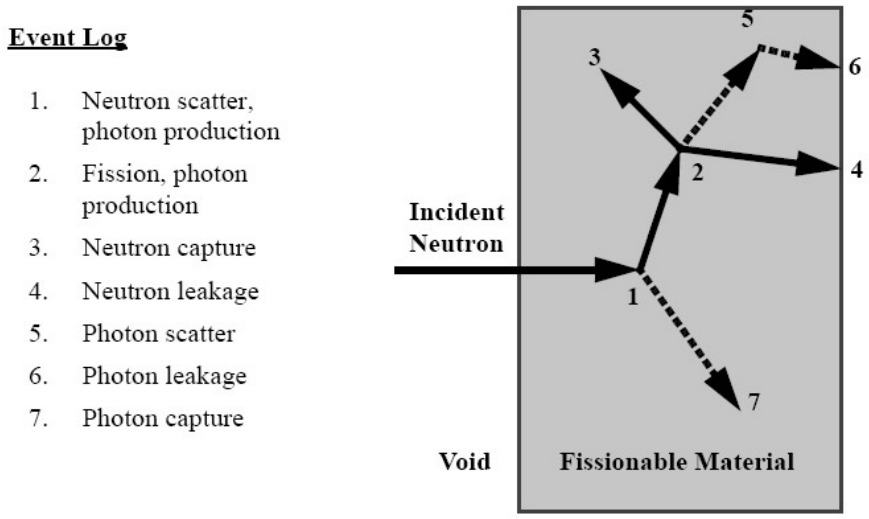

Figure 4.1: Monte Carlo sampling of a neutron entering a material that can undergo fission. The possible physical interactions (1-7) are selected randomly, based on their respective probabilities. Published in [83].

The particular choice of MCNP for this study bases on its long history as Monte Carlo code in nuclear medicine, the many validation studies showing the good agreement between actual dose measurements and MCNP simulations [85, 88, 84] as well as the advantage of supplementary software for building MCNP models (see subsection 4.2.2). The simulations were performed with the 4c2 version of MCNP. However test simulations with MCNP5 were run and showed no statistical significant differences to the former version.

The amount of MCNP documentation by its creators as well as users is copious which is why the description of the code here will be limited to a minimum. For detailed information the MCNP manual is recommended [83] and for a qualitatively high but quick overview of the most important features one should refer to the report of Shultis and Faw [90]. MCNP is a FORTRAN code that has been under constant development for decades. Editing and re-compiling the code is not necessary since MCNP uses a special scripting language that defines the simulation parameters in the so called input file which consists on three major parts, also called "cards" in MCNP lingo:

1. Cell cards: This entry section indexes the volumetric entities, called cells, and denotes the enclosing surfaces. Additionally the cell is associated with a material number (the composition of the material is defined within the data

cards, see below), the density, importance concerning particular particles and optionally a numerical value of the cell's volume. The importance of a cell with regard to a certain kind of particle reflects the artificial augmentation or reduction of the number of sampled particles in order to improve the statistics.

2. Surface cards: Here the surfaces referred to in the first section are defined by means of standard geometrical forms like planes, spheres, cylinders, cones, ellipsoids and other.

3. Data cards: This block is reserved for the physical boundary conditions of the simulation, i.e. the elemental composition of the defined materials (thus influencing MCNP's choice of cross section data) the number and kind of source particle, preciseness of the transport simulation (e.g. the extent of consideration of secondary produced particles), the specifications of the source like location, size, shape, collimation, energy or spectrum as well as the physical aspect to be investigated which is called *tally* in MCNP.

MCNP provides different sorts of tallies like surface current, flux or energy deposition in cells as well as others.

In order to check the result for its statistical significance several statistical tests have to be applied. If the simulation passes all these tests it is viewed as statistical significant from a MCNP point of view. That doesn't necessarily mean that the simulation yields useful information for the physical model. On the other hand the failure in one or two statistical tests doesn't annul the entire simulation. Rather it is in the experience and the physical foreknowledge of the user to judge the statistical records. For details on all statistical key data MCNP produces the interested reader is referred to the aforementioned documentation. However two statistical quantities that will be mentioned more often throughout this work should be explained briefly. Let x be the physical quantity that is *tallied* by MCNP then x_i is the score resulting from the i^{th} random walk. The expected value of x, $\langle x \rangle$ is approximated by the sample mean $\bar{x}$, i.e. the average of scores of all simulated particle histories. This way the *normed average tally per history* is defined as

$$\bar{x} = \frac{1}{N} \sum_{i=1}^{N} x_i, \tag{4.2}$$

where N denotes the total number of simulated particle histories. For example if one tallies the energy deposition in a specific cell, $\bar{x}$ is the average deposited energy per particle in this volume. Another statistical quantity is the relative error R of a tally mean, defined as

$$R = \frac{S_{\bar{x}}}{\bar{x}}, \tag{4.3}$$

where $S_{\bar{x}}^2$ is the variance of the average $\bar{x}$

$$S_{\bar{x}}^2 = \frac{1}{N} S^2, \tag{4.4}$$

with

$$S^2 = \frac{1}{N-1} \sum_{i=1}^{N} (x_i - \bar{x})^2 \simeq \overline{x^2} - \bar{x}^2, \tag{4.5}$$

and

$$\overline{x^2} = \frac{1}{N} \sum_{i=1}^{N} x_i^2. \tag{4.6}$$

According to the MCNP manual [82] R should be less than 0.1 in order to speak of meaningful results. Clearly, the smaller is R the more reliable is the tally mean $\bar{x}$.

4.2.2 BodyBuilder

In order to expand the Cristy and Eckerman series like described in subsection 3.3.2 the BodyBuilder Software by White Rock Science was used. This tool was developed for the sole purpose to generate MCNP input files describing human mathematical phantoms of arbitrary age, from infant through adult as well as females at different pregnancy states including fetal detail. In doing this BodyBuilder relies on the original phantom data of the Cristy and Eckerman series [63] and Stabin's pregnant and nonpregnant adult female [64]. The software assigns a nominal age to the created phantom. The 1, 5, 10, and 15 years correspond to the respective Cristy/Eckerman phantoms of the same designation, whereas the BodyBuilders 21-year phantom correlates with the Cristy/Eckerman adult. The phantoms with nominal ages in between are constructed via linear two-point interpolation through the use of the respective height for age curve. However, at this point, it should be stressed that the phantoms' nominal age should be seen more as an identifier than as an actual physical parameter.

BodyBuilder offers various options with regard to the phantom's anatomy or attention to detail. In the user interface (see figure 4.2) one can select not only the phantom's nominal age (which then determines height and weight) and gender but also the organs that shall be modeled specifically. Additionally the software offers to add body fat or an alternative phantom in sitting posture instead of the usual upright standing positions. The manual [91] provides more elaborated guidance.

Summarizing BodyBuilder's output defines a MCNP input file in terms of cell- and surface cards. The data cards describe the specific scenario of the radiation transport simulation and thus have to be defined manually by the user.

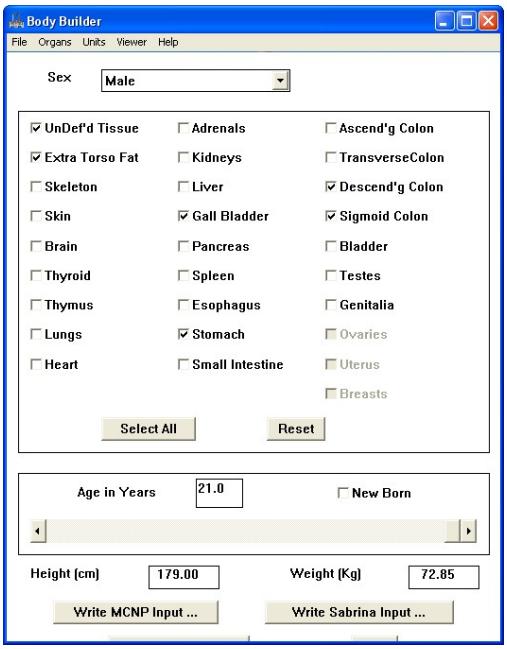

Figure 4.2: Screenshot of BodyBuilder main window.

4.3 Phantom ensemble

In this part the properties of the phantom ensemble suggested in subsection 3.3.2 are described. As mentioned before BodyBuilder is used to generate MCNP input files for 21 different phantoms where the 1, 5, 10, and 15 years-old old phantoms correspond to the respective Cristy/Eckerman phantoms of the same designation and the 21-year phantom correlates with the Cristy/Eckerman adult. The phantoms with nominal ages in between are constructed via linear two-point interpolation. Once again the nominal age should be seen purely as designation. As discussed in the motivation, the idea of an expanded ensemble is that one then selects the phantom that matches the patient closest according to physiognomic parameters, such as height and weight, rather than age. For the ages 16-21, the phantoms were chosen androgynous, meaning that both male and female organs are components of the same model. As for the age groups 1-15, the sexes were split up, still sharing the same height but with slightly different weight. A newborn phantom was not included in this study. Table 4.1 gives an overview over the ensemble's physical properties. Since the results of this study are to be compared with data from the literature (see subsection 3.3.2) it also shows the corresponding data of the Cristy/Eckerman series [63] which is used in ICRP 80 and by OLINDA/EXM as well as the weight of the adult female created by Stabin and

co-workers [64] (also used in the OLINDA/EXM software) and the adult male phantom created by Snyder et al. [62] which is used by MIRD Dose Estimate Report No. 19. The phantoms labeled adult (male and female) by Cristy and Eckerman, Stabin et al. and Snyder et al. respectively have no nominal age which is why they were located in the row that corresponds to the ensemble phantom with the best matching weight. Three different types of tissues were used; adult

		Phantom weight [kg]				
Age	Height	Ensemble		Cristy &	Adult	Adult
[yr]	[cm]	male	female	Eckerman	female (Stabin)	male (Snyder)
1	75	9.37	9.35	9.7		
2	83	11.85	11.83			
3	92	14.32	14.31			
4	101	16.80	16.78			
5	109	19.28	19.26	19.8		
6	115	21.96	21.94			
7	122	24.65	24.62			
8	128	27.33	27.29			
9	134	30.01	29.97			
10	140	32.69	32.65	33.2		
11	146	37.39	37.34			
12	151	42.10	42.03			
13	157	46.80	46.72			
14	162	51.50	51.40			
15	168	56.21	56.09	56.8	56.9	
16	170	59.43				
17	172	62.26				
18	174	65.08				
19	175	67.90				
20	177	70.72				70
21	179	73.54		73.7		

Table 4.1: Weight [kg] of phantom ensemble, Cristy/Eckerman series, the adult female by Stabin et al. and Snyder phantom.

soft tissue, skeleton, and lung tissue with densities of 1.04, 1.4, and 0.296 g/cm^3, respectively. The material compositions of each tissue follow the ones reported in the Oak Ridge Reports [63, 64, 92] and are tabulated in Table 4.2.

	soft tissue	skeleton	lung tissue
densities [g/cm^3]	1.04	1.4	0.296
element	elemental fractions		
H	0.10454	0.07337	0.10134
C	0.22663	0.25475	0.10238
N	0.02490	0.03057	0.02866
O	0.63525	0.47893	0.75752
Na	0.00112	0.00326	0.00184
Mg	0.00013	0.00112	0.00007
Si	0.00030	0.00002	0.00006
P	0.00134	0.05095	0.00080
S	0.00204	0.00173	0.00225
Cl	0.00133	0.00143	0.00266
K	0.00208	0.00153	0.00194
Ca	0.00024	0.10190	0.00009
Fe	0.00005	0.00008	0.00037
Zn	0.00003	0.00005	0.00001
Rb	0.00001	0.00002	0.00001
Sr	-	0.00003	-
Zr	0.00001	-	-
Pb	-	0.00001	-

Table 4.2: Densities and elemental compositions of tissues.

4.4 Calculation of SAFs

As discussed in subsection 3.3.2 the idea of this work is to calculate SAFs for the annihilation photons of 511 keV by means of submitting the phantom ensemble to Monte Carlo simulations. The BodyBuilder Software was used to create the cell- and surface cards as well as the material compositions used in the MCNP simulations. In this section the details of the physical radiation transport model is described which belongs to the data card in the MCNP input file.

One has to understand that in order to investigate the SAFs for a given number of combinations of source- and target regions the determining factor is the number of source regions, since a single Monte Carlo simulation samples the particles from a given source and registers certain required aspects of their average behavior in the entire defined simulation domain. If all the target regions lie within this domain the required quantity (e.g. energy deposition in a target organ) can be determined for all target regions as a function of the source. In other words, 1 simulation corresponds to 1 particular phantom and source region but to a arbitrary number

of target regions. Therefore to reduce the amount of work and the accompanying computation time the source regions were restricted to the organs and tissues which have a documented specific uptake of ^{18}F-flourodeoxyglucose (^{18}F-FDG) according to MIRD Dose Estimate Report No. 19 [80] and ICRP Publication No. 80 [81]. In

Organ	MIRD Report No. 19	ICRP 80
Brain	0.22	0.15
Heart wall	0.12	0.10
Urinary bladder content	0.13*	0.32†
Liver	0.14	-
Lungs	0.06	-
Kidneys	0.03	0.02
Pancreas	0.006	-
Spleen	0.01	-
Whole blood	0.26	-
Total body	2.38	2.13±

* Based on 2 hours void intervals, starting 2 hours after dosing, using the traditional static MIRD model [80] .
† Based on the ICRP model for the bladder representing the voiding period for an adult of 3.5 hours [81].
± Excluding bladder contents .

Table 4.3: Residence times of ^{18}F-FDG in simulated source organs in hours.

table 4.3 whole blood is listed as source organ. As a matter of fact whole blood is not considered to have a specific uptake of ^{18}F-FDG but since direct observational data are unavailable for red marrow the residence time for this organ is assumed to have the same concentration and kinetics as those of whole blood [80].

The SAFs for the annihilation radiation of 511 keV were calculated by applying the MCNP4c2 Monte Carlo code to the phantoms, assuming the respective source organs to be isotropic volume sources of 511 keV photons, thus simulating a homogeneous activity concentration. In order to reduce computation time, the so-called kerma approximation was deployed, meaning that secondary electrons due to inelastic photon interaction were not pursued further and their energy was assumed to be deposited locally. This simplification is very common in radiation transport calculations and justified by the secondary particle equilibrium for points located well within the body and the macroscopic approach [93]. For superficial organs such as the skin, the kerma approximation is valid for energies up to 1 MeV [94, 95]. In MCNP the kerma approximation is realized by applying the so called

"p-mode" to the photons instead of the "e, p -mode" which would induce MCNP to track all the produced secondary electrons. 20 millions photon histories were simulated each run and the F6 tally [90] was used to sample the energy deposition in the target volume. In each phantom up to 45 organs were defined as target organs, using the F6 tally to calculate the absorbed energy fraction. In Appendix A an example of an MCNP input file is displayed.

However the SAFs for the 511 keV photon that result from the red marrow (RM) being a source organ, were interpolated from the Cristy/Eckerman data of the adult, 15-, 10-, 5-, and 1-year-old phantoms. The data analysis software Origin (OriginLab Corporation, Northampton, MA) was used to fit analytic curves to the phantoms' $\Phi(r_T \leftarrow \mathrm{RM}, E_\gamma)$ as a function of their weight. This was done for each target organ considered for absorbed dose estimates (see section 4.5). In the following the fits are tabulated: $\Phi(\text{ovaries} \leftarrow \mathrm{RM}, E_\gamma)$ was approximated with a monoexponential function $y(m)$ where m is the phantom's mass (see table 4.4):

$$y(m) = y(0) + A_1 e^{(-m/t_1)} \tag{4.7}$$

Table 4.5 gives an overview over the SAFs approximated with biexponential functions of the form:

$$y(m) = y(0) + A_1 e^{(-m/t_1)} + A_2 e^{(-m/t_2)} \tag{4.8}$$

Finally the triexponential approximations are as follows (see table 4.6):

$$y(m) = y(0) + A_1 e^{(-m/t_1)} + A_2 e^{(-m/t_2)} + A_3 e^{(-m/t_3)} \tag{4.9}$$

Table 4.7 gives an overview over the organs and tissues modeled in the SAF-simulations. Bold fonts denote source organs which of course are also target organs. As already mentioned in subsection 3.3.2 the total number of individual simulations performed with 9 source organs and 36 different phantoms (6 androgynous, 15 male, 15 female, see section 4.3) mounts up to 324.

organ	$y(0)$	A_1	t_1
ovaries	1.02×10^{-5}	1.72×10^{-5}	25.66

Table 4.4: Parameters describing the monoexponential function that approximates $\Phi(\text{ovaries} \leftarrow \text{RM}, E_\gamma)$.

organ	$y(0)$	A_1	A_2	t_1	t_2
heart wall	4.95×10^{-6}	6.39×10^{-5}	9.50×10^{-6}	2.86	20.48
kidneys	1.46×10^{-7}	1.93×10^{-5}	1.54×10^{-5}	12.02	118.97
lungs	2.46×10^{-6}	3.04×10^{-5}	8.49×10^{-6}	7.34	73.75
pancreas	6.82×10^{-6}	3.71×10^{-5}	1.30×10^{-5}	3.30	21.22
spleen	2.58×10^{-6}	5.63×10^{-5}	1.14×10^{-5}	3.79	42.11
testicles	-3.38×10^{-6}	1.44×10^{-5}	1.05×10^{-5}	5.37	101.16

Table 4.5: Parameters describing the biexponential functions that approximate the SAF for the respective organ.

organ	$y(0)$	A_1	A_2	A_3
brain	-1.17×10^{-5}	1.34×10^{-4}	2.12×10^{-5}	4.27×10^{-7}
liver	3.24×10^{-6}	8.75×10^{-5}	1.02×10^{-5}	1.28×10^{-6}
red marrow	-2.37×10^{-4}	9.48×10^{-5}	5.17×10^{-4}	-2.46×10^{-4}
urinary bladder wall	-1.33×10^{-6}	1.37×10^{-5}	5.29×10^{-4}	-1.81×10^{-6}

organ	t_1	t_2	t_3
brain	4.56	243.33	-1.97×10^{85}
liver	2.92	28.49	-1.39×10^{102}
red marrow	5.80	3595.00	-1.12×10^{85}
urinary bladder wall	110.15	1.95	-8.51×10^{79}

Table 4.6: Parameters describing the triexponential functions that approximate the SAF for the respective organ.

ascending colon wall	arm bones	pelvis
ascending colon contents	skull & face	ribs
sigmoid colon wall	spine	clavicles
sigmoid colon contents	scapulae	**kidneys**
gall bladder wall	esophagus	**liver**
gall bladder contents	**lungs**	**pancreas**
stomach wall	stomach contents	**spleen**
transverse colon wall	legs (soft tissue)	**brain**
transverse colon contents	leg bones	testicles
penis & scrotum	legs skin	thyroid
penis & scrotum skin	thymus	head and neck skin
descending colon wall	adrenals	ovaries
descending colon contents	**heart wall**	breasts
urinary bladder contents	urinary bladder wall	uterus
small intestine	trunk skin	**total body**

Table 4.7: Source (bold) - and target organs considered in the simulations.

4.5 S-Values and Absorbed-Dose Estimates

Having determined the SAFs $\Phi(r_T \leftarrow r_S, E_i)$ for the relevant pairings of source- and target organs the next step is to calculate the corresponding S-value $S(r_T \leftarrow r_S)$ which was defined in equation 3.16 as follows:

$$S(r_T \leftarrow r_S) = \frac{1}{M(r_T)} \sum_i E_i \, Y_i \, \phi(r_T \leftarrow r_S, E_i). \tag{4.10}$$

The nuclear data of ^{18}F were taken from the National Nuclear Data Center at the Brookhaven National Laboratory (New York, NY) [96]. Having a half life of 109.77 min ^{18}F decays into ^{18}O via β^+ transition with a probability of 96.73%, resulting in the emission of 2 annihilation photons of 511 keV. The alternative decay path involving electron capture with its consequent emission of Auger electrons and X-rays was omitted in the calculations of the S-values, since the respective contribution is negligible [80]. Thus the radiation properties relevant to calculate $S(r_T \leftarrow r_S)$ according to its definition can be summarized like this: The mass of the target organ $M(r_T)$ results from the phantom's architecture, i.e. the respective volume and density and is generated by the BodyBuilder software. This leaves $\phi(r_T \leftarrow r_S, E_i)$ as the last missing parameter. The photon contribution was calculated in the Monte Carlo simulation described in the previous section.

Radiation type	E_i [keV]	Y_i
β^+	250	1
photon	511	2

Table 4.8: Decay data relevant for internal dosimetry of ^{18}F.

MCNP's F6 tally determines the energy deposition in a target volume in units of MeV/g per emitted source particle. Because of relation 3.21, the known energy of the emitted photon and $M(r_T)$ the AF $\phi(r_T \leftarrow r_S, E_\gamma)$ can be calculated easily.

As for the β^+ contribution the approximations described in section 3.1 were applied, i.e. $\phi(r_T \leftarrow r_S, E_{\beta^+}) = 1$ in case of organ self-irradiation whereas for cross-irradiation $\phi(r_T \leftarrow r_S, E_{\beta^+}) = 0$. The dose to the urinary bladder wall caused by the radiation of the bladder contents was calculated by using the approximation for walled organs (see page 33).

Dosimetry with regard to the red bone marrow is somewhat more complex. The high radiosensitivity of red marrow makes the respective absorbed dose to one of the most limiting factors in nuclear medicine procedures which is why the red marrow is always listed as target organ of interest. However as documented in table 4.3 the red marrow is also considered as source organ in dose calculations involving ^{18}F-FDG. Therefore following components have to be considered (RM denotes red marrow):

1. $\phi(\mathrm{RM} \leftarrow \mathrm{RM}, E_\gamma)$
2. $\phi(\mathrm{RM} \leftarrow \mathrm{RM}, E_{\beta^+})$
3. $\phi(\mathrm{RM} \leftarrow r_S, E_\gamma)$
4. $\phi(\mathrm{RM} \leftarrow r_S, E_{\beta^+})$

Component 1 was interpolated from the Cristy/Eckerman data as described on page 53. Component 4 can be taken to be 0 in consistence with the approximations for β-particles. In order to calculate component 2 and 3 one first has to tackle the issue of the amount of red marrow in the respective bone, a quantity dependent on age and the particular part of the skeleton. Bones of children and adolescents contain much more red marrow because they are still in a growth phase. To account for this effect the following conservative assumption was made for the red marrow as fraction of the total bone mass : The phantoms with the nominal ages 1-3 were assigned the same fraction of red marrow as the 1 year old in the Cristy/Eckerman phantom series, the nominal ages 4-7 as the 5 year old, 8-12 as the 10 year old, 13-17 as the 15 year old, and 18-21 as the adult phantom. For the

numerical values with regard to each bone as tabulated in table 4.7 it is referred to the aforementioned work [63].

With regard to component 2, i.e. the contribution to the S-value, which results from β-particles originating and irradiating the red marrow, the same data was used as by OLINDA/EXM. It origins in the work of Eckerman and Stabin [57] and describes $\phi(\mathrm{RM} \leftarrow \mathrm{RM}, E_{\beta^+})$ for discrete electron energies and for each phantom of the Cristy and Eckerman series. The data for the discrete energy lines was applied to the spectrum of ^{18}F taken from the RADAR webpage [97, 98] and $\phi(\mathrm{RM} \leftarrow \mathrm{RM}, E_{\beta^+})$ was calculated for each phantom of the Cristy and Eckerman series, excluding newborn. Concerning the phantom ensemble $\phi(\mathrm{RM} \leftarrow \mathrm{RM}, E_{\beta^+})$ was assigned to the respective phantoms using the same association as described in the paragraph above.

Component 3, the dose received by the red bone marrow by photon cross-irradiation can be calculated using different methods. As described more detailed in the article of Kramer and co-workers [99] there are three major approaches:

1. **The CT number (CTN) method:** This method is also referred to as the voxel method in some parts of the literature, stemming from the fact that it was developed for the skeletal dosimetry of voxel phantoms. Originally introduced by Zankl and Wittmann [66] it was further developed by Kramer et al [100, 101]. The principle is to create a heterogeneous tissue distribution among the skeletal voxels by using the grey values of the original CT images. This way each skeletal voxel is assigned to cortical bone, spongiosa or marrow, thereby allowing to observe the energy deposition in marrow separately. However in the case of the spongiosa the 3CF-method (see below) has to help out since this tissue is considered to be a homogeneous mixture of trabecular bone and marrow.

2. **Fluence-to-dose response (FDR) function:** Contrary to the previous paragraph mathematical phantoms have a homogeneous skeleton, i.e. consist of a homogeneous mixture of bone and marrow. In the work of Cristy and Eckerman [63] already cited a couple of times the authors developed bone-specific functions that relate the computed photon fluence to the dose of the red marrow (Fluence-to-dose response (FDR) functions). In a recent work [102] the FDRs were revised in order to be applicable to skeletal subdivisions of voxel phantoms.

3. **The three correction factor (3CF) method:** This method was applied in the present work and was developed by Kramer et al [103]. Just as the FDRs the 3CF method relates to a composition of the skeleton that is a homogeneous mixture of bone and marrow. The energy deposited in the red bone marrow E_{rm} can then be calculated according to following relation

[104]:

$$E_{rm} = E_b \cdot r_{rm} \cdot \frac{\left(\frac{\mu_{en}}{\rho}(E)\right)_{rm}}{\left(\frac{\mu_{en}}{\rho}(E)\right)_b} \cdot S(E). \tag{4.11}$$

E_b is the amount of energy deposited in the homogeneous mixture of bone and marrow. The approach is named after the three correction factors applied, namely the red marrow fraction of the total bone mass r_{rm}, the mass energy absorption coefficient $\left(\frac{\mu_{en}}{\rho}(E)\right)_i$ at photon energy E for medium i and the so called King-Spiers factor $S(E)$ [105]. The later represents a dose enhancement correction factor that compensates for the photo-electrons released in trabecular bone and entering the marrow cavities. Following the relation

$$\left(\frac{\mu_{en}}{\rho}(E)\right)_b = r_{hb} \cdot \left(\frac{\mu_{en}}{\rho}(E)\right)_{hb} + r_{rm} \cdot \left(\frac{\mu_{en}}{\rho}(E)\right)_{rm} + r_{ym} \cdot \left(\frac{\mu_{en}}{\rho}(E)\right)_{ym}, \tag{4.12}$$

where the index b stands for the homogeneous mixture of bone and marrow used in the simulation model, hb for hard bone and rm as well as ym for red and yellow marrow respectively. The absorbed dose to the red marrow of a particular bone was calculated by applying relation 4.11 and 4.12. E_b is the F6 tally for the respective bone determined by the simulation whereas the correction factors are documented in the literature. r_{hb}, r_{rm} and r_{ym} ($r_{hb} + r_{rm} + r_{ym} = 1$) are taken from the work of Cristy and Eckerman (cf. page 55), $S(E)$ from the aforecited source and the mass energy absorption coefficients $\left(\frac{\mu_{en}}{\rho}(E)\right)_i$ from International Commission of Radiation Units and Measurements (ICRU) report No. 44 [106].

The King and Spiers factors cannot be used for the calculation of the absorbed dose to the bone surface. As described in the work of Kramer and co-workers [103] usually the average absorbed dose to the skeletal mixture is taken as a conservative estimate for the dose to bone surface when relying on the 3CF method. This approximation is also applied in this study, i.e. the F6 tally used for the energy deposition within bone.

Having described the calculation of the SAFs, S-values and their associated approximations with regard to the dose calculations the only essential input missing is the biokinetic data of ^{18}F-FDG. As described in section 3.3.2 the documented residence times of MIRD Dose Estimate Report No. 19 [80] and the ICRP Publication No. 80 [81] as tabulated before in table 4.3 were applied. However in case of the residence times for the urinary bladder ICRP 80 relies on different voiding

Phantom	1 yr	5 yr	10 yr	15 yr	adult
Voiding period [h]	2	2	3	3.5	3.5

Table 4.9: Voiding periods for urinary bladder in ICRP 80

periods for different age groups, see table 4.9. For the established ensemble of 21 phantoms, the voiding periods between nominal age 15 and 5 were interpolated. The Origin software was used to fit an analytic curve $\nu(a)$ to the three voiding periods of the 15-, 10-, and 5 year old as a function of their nominal age a:

$$\nu(a) = 0.5 + 0.35a - 0.01a^2. \tag{4.13}$$

The phantoms with nominal ages ≥ 15 and ≤ 5 have the voiding period set to 3.5 and 2 hours, respectively.

Finally $d(r_T, T_D)$, the absorbed dose to a target region per unit administered activity was calculated using the MIRD equation 3.17 (page 34).

The effective dose E (equation 3.20) was calculated as defined by ICRP Publication No. 60 [60]. The reason why the weighting factors from ICRP 60 were chosen rather than the new ones from ICRP 103 [49] lies in the fact that in this study the calculated effective dose was compared to the values of absorbed dose per unit administered activity ^{18}F-FDG provided in ICRP 80 [81]. However, ICRP 80 relies on ICRP 60 when calculating the effective dose. So, in order to make the results in this study comparable to the ones in ICRP 80, the same assumption basis has to be kept, which, in this case, implies relying on ICRP 60.

Almost immediately after the publication of the paper this thesis is based on [1] a new ICRP report was published, namely ICRP Publication 106 [107] that revises the radiation dose to patients from radiopharmaceuticals. The only real difference to ICRP 80 is that ICRP 106 uses different biokinetic data whereas the effective dose, its definition as wells as the calculation, stills refers to ICRP 60. Therefore applying the new biokinetic data of ICRP 106 and subsequent comparison of the doses would not yield any new perception since this work focuses on the expansion of available phantoms and thereby SAFs and their impact on internal dose calculations. However the applied phantoms, SAFs and dose definitions of ICRP 106 and ICRP 80 are identical.

Chapter 5

Results

5.1 Simulation results of SAFs

The simulations on the phantom ensemble with 9 different source organs yielded a total of 324 simulations (cf. page 52). With the number of target regions being 45 in each simulation (see table 4.7) the entire study produced a total number of 14580 SAFs. In order to give meaningful statements rather than getting lost in the sheer amount of individual results it is necessary to focus on the big picture.

First of all let's explore the statistical significance of the results, i.e. the normed average tallies (cf. page 46). MCNP considers a tally mean as a meaningful result if the relative error R as defined in equation 4.3 is less than 0.1 [82, 90]. Taking into account all the relative errors of all the tallies calculated in this study the average relative error of the SAFs has a value of 0.00584 ± 0.00869, ranging from 0 to the maximum of 0.0921. That means that all simulated SAFs not only fulfill the quality criteria of the MCNP statistical test with regard to R but that their relative error is astonishingly low and thereby their stochastic accuracy very high. The reason for this is the large number of particles histories that were run in the simulations (see section 4.4), a measure that could be taken because of the availability of a parallel processing computer grid.

Analyzing the different dependencies of R produces valuable insight to the radiation transport calculations. Figure 5.1 shows R as a function of the respective tally value which in our case has the unit of a dose [MeV/g]. Although there is a lot of statistical noise a clear tendency towards lower R can be seen with increasing tally value. This can be understood easily when looking at equations 4.2 to 4.6 and considering that a target organ with a small tally has fewer scores x_i and therefore most likely a larger variance $S_{\bar{x}}^2$ whereas a big tally results from a much higher number of x_i and therefore produces a smaller R. Another aspect is the behavior of R in dependence of the phantom's size. In figure 5.2 R is averaged over

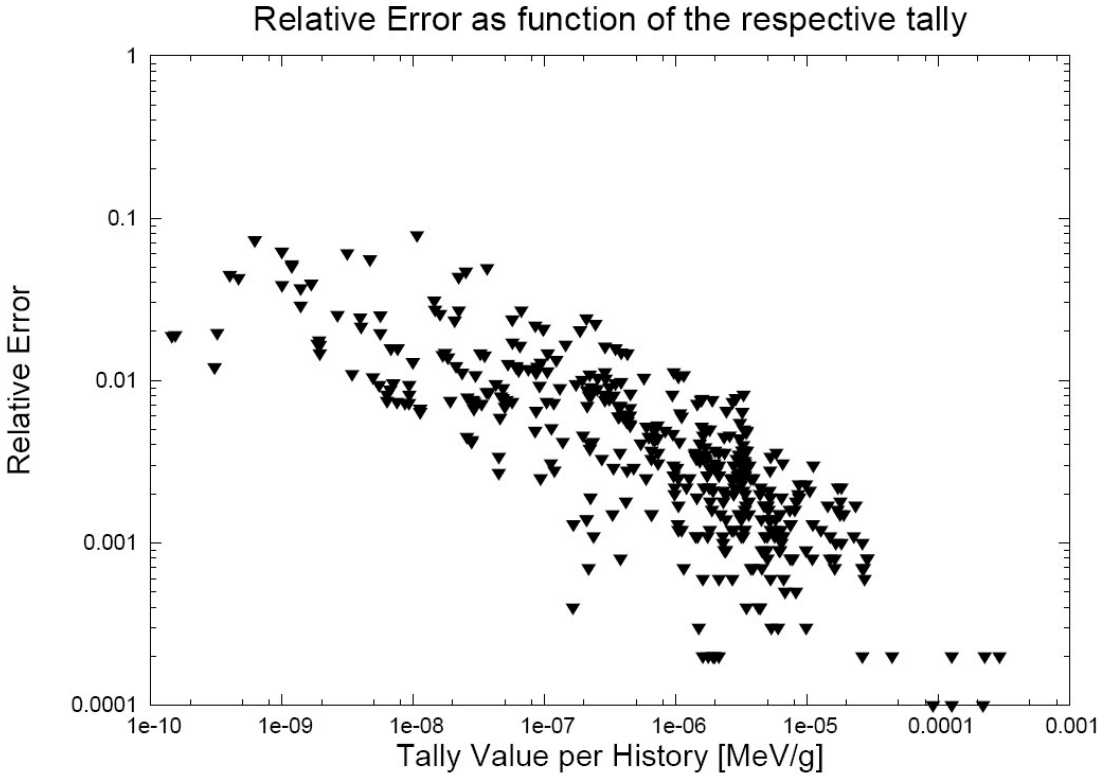

Figure 5.1: R as a function of the respective tally. The graph shows the results of the simulation series with different source organs applied to the phantom with nominal age 21.

an age group. i.e. the arithmetic mean of all the tallies' relative errors produced associated with one age group regardless of sex and source organ. The oscillating decrease of R with decreasing age becomes monotone decreasing with the phantom having a nominal age ≤ 11 yr. The improvement of the statistics with decreasing phantoms size can be explained with the smaller dimensions of the phantom that implicates a higher average photon flux at a constant number of particle histories.

Still another perspective is the role of the source organ. Figure 5.3 shows R averaged over all tally results from one simulation, i.e. one specific phantom and source organ. Comparing the results of the biggest and smallest phantom one can clearly see following relations:

- The results of the 1 year old show much less deviation between the different source organs than in the case of the 21 year old phantom. Whereas the ratio of values stemming from the source organ causing the highest relative errors (brain) to the region causing the lowest relative errors (total body) is

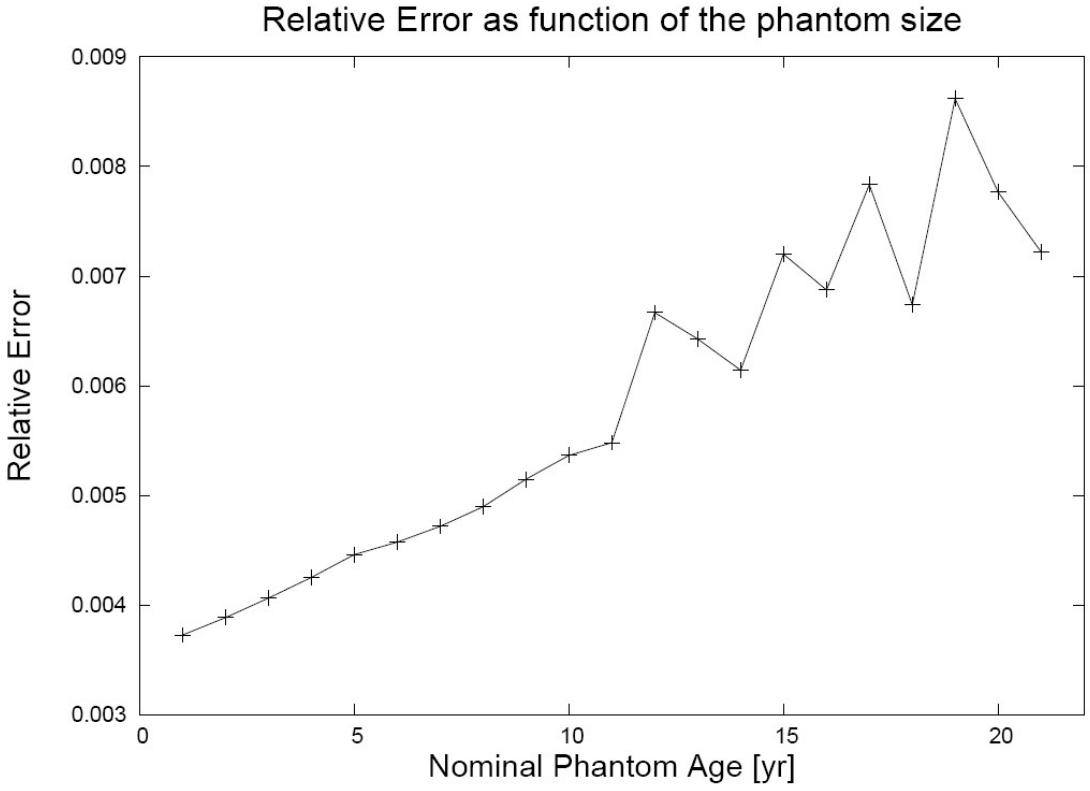

Figure 5.2: R as a function of the phantom size.

4.7 in case of the 21 year old phantom it's only 2.7 in the case of 1 year old.

- The relative error is considerably smaller in case of 1 year old phantom with regard to all source regions. This and the relation above are a logical consequence of the smaller phantom size as already discussed before

- In the case of both the 1 year as well as the 21 year old phantom the total body as source organ causes the lowest relative error whereas the brain causes the highest, followed by the urinary bladder wall. Also this result is consistent with fundamental physical considerations. In case of the entire body as source organ every target organ is a source organ as well and has other source organs as immediate neighbors, thus causing a homogeneous photon flux throughout the whole body. On the contrary if one single organ acts as source the photon flux will decrease with the distance between source and target organ. An organ like the brain is spatially much more separated from the rest of the organs than for example lung or liver. This applies also

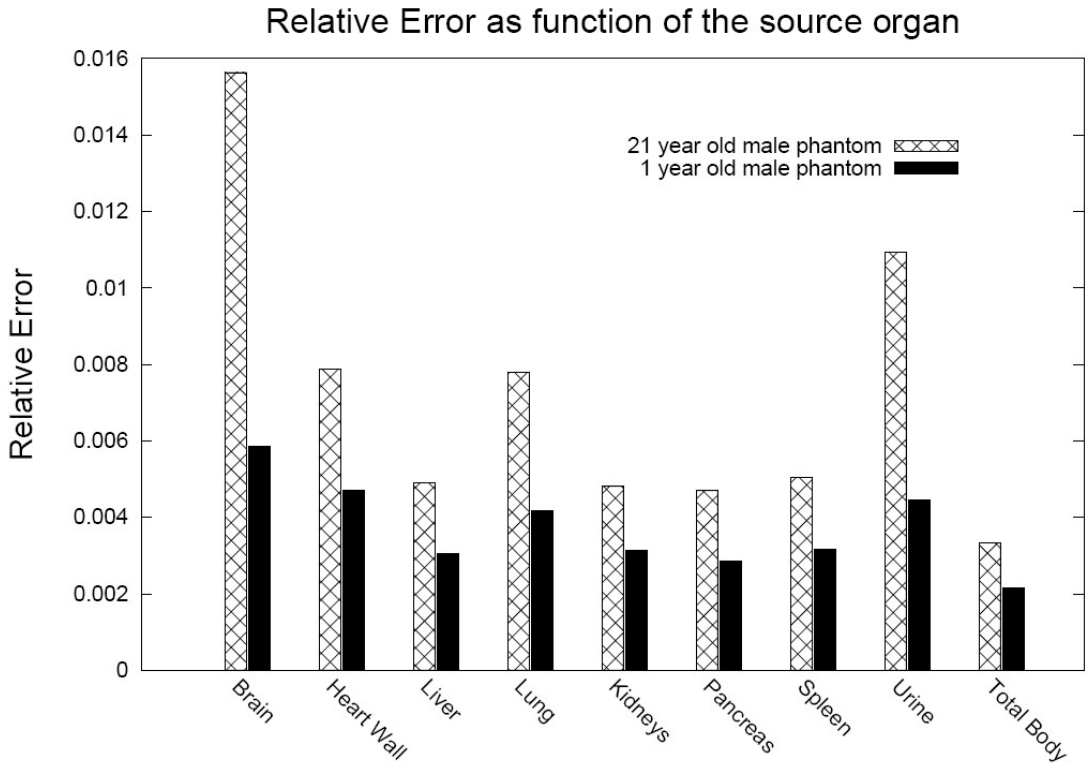

Figure 5.3: R as a function of the source organ. Comparison of biggest and smallest phantom

for the urinary bladder which is situated on the pelvic floor.

Concluding one can say that the statistics of the simulations conducted show very small errors (cf. page 59) and that their dependence of parameters like tally value, phantom size or source organ correspond to the physical model.

As stated in the beginning of this section 14580 SAFs were calculated. Individual comparison with the Cristy/Eckerman series is neither manageable nor useful which is why the comparison is done in the framework of a complete internal dose calculation of ^{18}F-FDG as outlined in subsection 3.3.2.

5.2 Comparison with ICRP 80

Before the presentation of the calculated absorbed organ doses of the phantom ensemble and the subsequent comparison with the respective results of the ICRP 80 and MIRD Dose Estimate Report No. 19 an important issue has to be addressed,

namely the uncertainties of the calculated quantities. As can be seen in the big amount of data presented in this chapter only two tables (5.13 and 5.14) indicate the uncertainties specifically. This is due to the following reason: When performing internal dose calculations for reference models, the uncertainties mainly derive from the biokinetic input [108], hence the residence times. Since neither the biokinetic models of ICRP nor the weighted mean residence times in MIRD Dose Estimate Report No. 19 state any uncertainties, an accurate assessment of the overall error of the absorbed dose to the organs in question is not possible. The only exception is the dose to gonads when reducing the biokinetic input to urinary bladder and remainder. In this case, the data of Hays and Segall [109] was used as was done in MIRD Dose Estimate Report No. 19. The results can be seen in table 5.13 and 5.14. Theoretically one still could list the uncertainties that emerge from the radiation transport calculation. However as described in the previous section on page 59 the use of a sufficient number of particle histories in the Monte Carlo simulations ensures a considerably small error in the calculations of the SAFs and hence the S-values. In fact the resulting errors are so small (less than 1%) that compared to realistic uncertainties of biokinetic models (up to 20% [109]) a specific mentioning doesn't make a lot of sense.

ICRP Publication No. 80 [81] provides the results for the adult, 15-, 10-, 5-, and 1-year-old phantoms with regard to 25 different organs and tissues. In order to compare the results of the SAF-calculations of the phantom ensemble in this study with the data series of ICRP 80 the dose estimates for the aforementioned phantoms and organs are matched. This is straightforward for the age groups of the 15-, 10-, 5-, and 1-year-old phantoms. However the ICRP's adult phantom is matched with this study's phantom of nominal age 20 since they have a comparable weight . Among the 25 organs cited by ICRP 80 there are also dose estimates for the esophagus and the muscles. However since there was no dosimetric model for the esophagus at the time ICRP 80 was published the dose to the thymus then was used as a surrogate. Therefore a comparison of the dose values for the esophagus is not very plausible at this point however listed in table. In return the muscles were not incorporated in the simulation model presented in this study. With regard to the effective dose value that has the absorbed dose to muscles as input parameter, the respective values were interpolated biexponentially from the Cristy/Eckerman data as a function of the phantom's weight. Also listed in the ICRP 80 is the dose value for the so called "Remainder." The remainder is defined in ICRP 60 [60] as being composed of adrenals, brain, upper large intestine, small intestine, kidney, muscle, pancreas, spleen, thymus and uterus. The exact assignment of the tissue weighting factor w_T (cf. eq. 3.20) can be looked up there. This is especially important if one of the remainder tissues receives a dose in excess of the highest dose in any of the twelve organs for which w_T is defined explicitly.

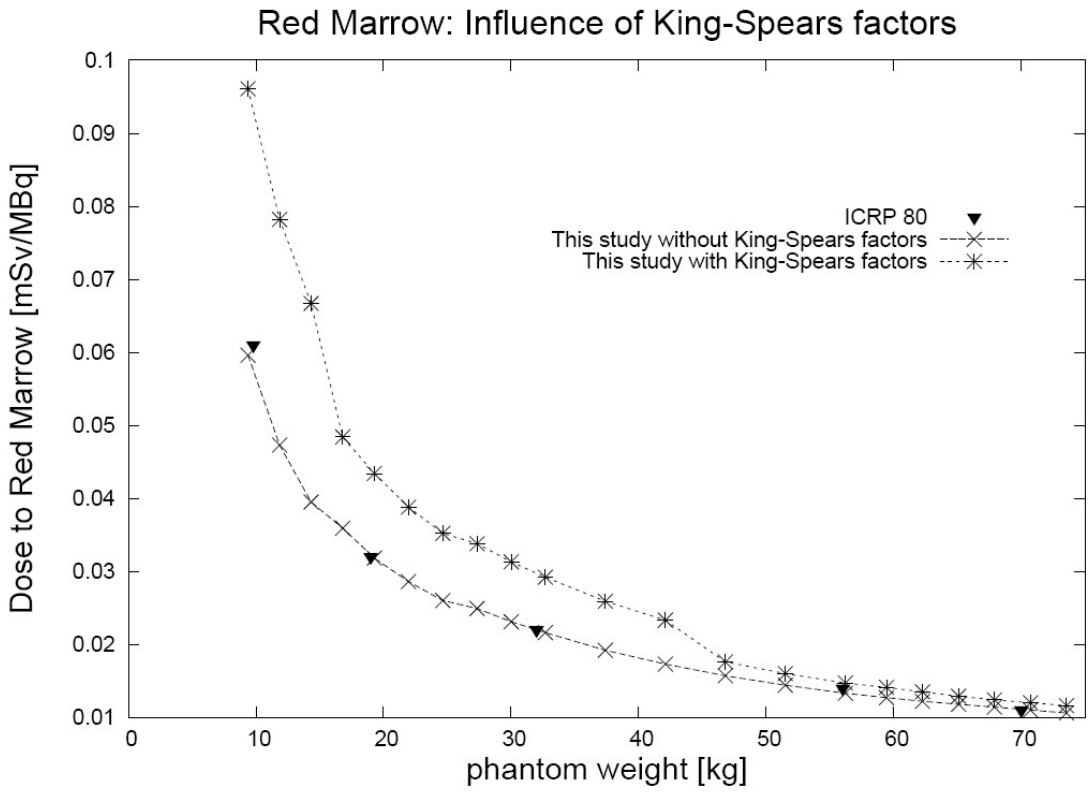

Figure 5.4: Absorbed dose to red marrow using biokinetics reported in ICRP 80 with and without applying King-Spiers factors.

Before taking a look at the overall accordance with the ICRP 80 values the most interesting result concerning an individual organ shall be outlined, namely the absorbed dose to the red bone marrow. Figure 5.4 shows the calculated values with and without applying the King-Spiers factors (cf. page 57) demonstrating that their omission rather then their inclusion leads to a astoundingly good accordance. The relative deviations to the ICRP 80 without the factors are only $+0.3\%, -4.8\%, -1.6\% - 0.2\%$ and -2.1% for the adult, 15-, 10-, 5-, and 1-year-old phantom respectively (see table 5.1 to 5.3) whereas they rise to $+9.1\%, +5.0\%, +32.7\% + 35.6\%$ and even $+57.5\%$ when including them. This overestimation especially for pediatric phantoms cannot be found anywhere else in scientific literature which is why for the present study the 3CF method without the King-Spiers factors is assumed to yield the most reliable results. Hereafter all dose values to the red bone marrow correspond to this assumption.

Having 23 remaining organs and each of them five different phantoms leaves

Organ	Adult		15 yr	
	Ensemble	IRCP 80	Ensemble	IRCP 80
Adrenals	12.0	12	14.7	15
Brain	26.2	28	26.8	28
Gall bladder wall	12.3	12	15.1	15
Esophagus*	12.7	11	15.4	15
Stomach wall	11.5	11	14.2	14
Small intestine	13.3	13	16.4	17
Heart Wall	65.9	62	81.7	81
Kidneys	21.0	21	24.7	25
Liver	11.4	11	14.1	14
Lungs	12.1	10	14.9	14
Pancreas	12.5	12	15.3	16
Spleen	11.3	11	13.9	14
Testicles	12.3	12	15.7	16
Thymus	11.6	11	13.9	15
Thyroid	10.8	10	13.4	13
Urinary bladder wall	162.4	160	201.0	210
Breasts	8.7	8.6	10.7	11
Ovaries	15.7	15	19.5	20
Uterus	21.3	21	25.4	26
Red bone marrow	11.0	11	13.3	14
Skin	6.6	8	8.2	10
Bone surface	10.0	11	12.0	14
Colon	13.9	13	17	17
Remainder	11.9	11	14.4	14

*Equated with the dosimetric model of the thymus in ICRP 80

Table 5.1: Comparison of absorbed organ doses in μSv/MBq with regard to adult male and 15-years old phantom for organs and tissues listed in IRCP 80. Green coloring indicates a relative deviation to the ICRP 80 of $< \pm 5\%$, blue between $\pm 5\%$ and $\pm 10\%$ and red $> \pm 10\%$

a total number of 115 absorbed dose values to compare. In 79 cases (69%) the relative deviation to the ICRP 80 is $< \pm 5\%$, for 18 cases (16%) it's between $\pm 5\%$ and $\pm 10\%$ and for the same amount of cases the relative deviation is $> \pm 10\%$. Tables 5.1 to 5.3 tabulate the calculated organ doses of this study and ICRP 80, identifying the three different groups by the help of coloring. Most noticeable in 58 cases the deviation is even $< \pm 3\%$, that's more than 50% of all the cases.

Organ	10 yr Ensemble	10 yr IRCP 80	5 yr Ensemble	5 yr IRCP 80
Adrenals	23.5	24	37.4	38
Brain	23.5	24	32.2	34
Gall bladder wall	24.1	23	38.9	35
Esophagus	25.0	22	39.1	35
Stomach wall	22.5	22	36.4	36
Small intestine	25.2	27	40.1	41
Heart Wall	127.8	120	203.1	200
Kidneys	35.6	36	52.6	54
Liver	22.5	22	36.2	37
Lungs	23.8	21	37.3	34
Pancreas	23.9	25	38.1	40
Spleen	22.4	22	35.8	36
Testicles	20.0	26	37.8	38
Thymus	22.1	22	34.4	35
Thyroid	23.5	21	39.7	35
Urinary bladder wall	271.7	280	304.0	320
Breasts	17.5	18	28.5	29
Ovaries	29.4	30	43.9	44
Uterus	31.4	39	53.9	55
Red bone marrow	21.7	22	31.9	32
Skin	13.3	16	21.9	27
Bone surface	19.0	22	29.8	35
Colon	26.0	27	50.4	50
Remainder	21.9	22	34.8	34

*Equated with the dosimetric model of the thymus in ICRP 80

Table 5.2: Comparison of absorbed organ doses in μSv/MBq with regard to 10-years and 5-years old phantom for organs and tissues listed in IRCP 80. Green coloring indicates a relative deviation to the ICRP 80 of $< \pm 5\%$, blue between $\pm\,5\%$ and $\pm\,10\%$ and red $> \pm 10\%$.

No general relation can be found between the phantom's size and the deviations to ICRP 80. Rather the deviations with regard to particular organ doses are owed to the specific dosimetric model. In the following the relative deviations to the ICRP 80 of $> \pm 5\%$ (the doses colored red and blue in tables 5.1 to 5.3) are dealt with in detail.

Organ	Ensemble	IRCP 80
Adrenals	71.2	72
Brain	45.6	48
Gall bladder wall	74.1	66
Esophagus	73.5	68
Stomach wall	70.2	68
Small intestine	76.6	77
Heart Wall	369.3	350
Kidneys	93.6	96
Liver	69.7	70
Lungs	70.8	65
Pancreas	72.1	76
Spleen	68.8	69
Testicles	72.4	73
Thymus	65.0	68
Thyroid	78.4	68
Urinary bladder wall	567.3	590
Breasts	56.0	56
Ovaries	81.6	82
Uterus	98.4	100
Red bone marrow	59.7	61
Skin	44.4	52
Bone surface	58.1	66
Colon	76.7	74
Remainder	64.7	63

*Equated with the dosimetric model of the thymus in ICRP 80

Table 5.3: Comparison of absorbed organ doses in μSv/MBq with regard to the 1-year old phantom for organs and tissues listed in IRCP 80. Green coloring indicates a relative deviation to the ICRP 80 of $< \pm 5\%$, blue between $\pm 5\%$ and $\pm 10\%$ and red $> \pm 10\%$.

Colon and remainder

With regard to the colon as well as the pool of organs and tissues defined as the remainder by the ICRP the deviations exceed 5% only in case of a single phantom, namely the adult. To be precise it's +6.9% for the colon and +8.5% for the remainder. However the accordance of the other age groups is very good, ranging from ±0.2% to ±3.7% in case of the colon and ±0.5% to ±3.1% in case

of the remainder.

Esophagus and thymus

As mentioned in the beginning of this section the ICRP didn't have a specific dosimetric model for the esophagus on hand but instead used the absorbed dose to the thymus as an approximation. The comparison with the ensemble with regard to the later shows only slight deviations ranging from ±0.6% to ±7.4%.

Brain

Phantom	Deviations to ICRP 80 [%]	Deviations to OLINDA/EXM [%]
Adult	-6.5	-1.9
15 yr	-4.4	-0.9
10 yr	-5.3	-1.3
5 yr	-5.2	-2.1
1 yr	-5.1	-0.5

Table 5.4: This studies' deviations to the values tabulated in ICRP 80 and calculations with OLINDA/EXM with regard to the absorbed dose in brain.

As can be seen in table 5.4 the deviations between the ensemble and ICRP 80 with respect to the absorbed dose values for brain are almost all $> \pm 5\%$. Control calculations with OLINDA/EXM however have yielded almost a perfect accordance to the ensemble (table 5.4, second column) which strongly suggests the accuracy of both this studies results and the OLINDA/EXM calculations.

Heart wall

Similar to brain more than one phantom values shows deviation $> \pm 5\%$. However contrary to before the concurrent calculations with OLINDA/EXM increase the differences as tabulated in table 5.5. This observation and its cause will be discussed in-depth in the next chapter (see page 89).

Uterus, testicles and gall bladder wall

With respect to these three organs a particular phenomena can be observed. Whereas for the majority of age groups there is an excellent agreement very large differences can be made out for certain phantom sizes. Table 6.2.2 shows that

Phantom	Deviations to ICRP 80 [%]	Deviations to OLINDA/EXM [%]
Adult	6.3	9.7
15 yr	0.8	10.0
10 yr	6.5	5.6
5 yr	1.5	6.9
1 yr	5.5	9.3

Table 5.5: This studies' deviations to the values tabulated in ICRP 80 and calculations with OLINDA/EXM with regard to the absorbed dose in the heart wall.

Phantom	Uterus	Testicles	Gall bladder wall
Adult	1.3	2.1	2.3
15 yr	-2.2	-1.6	0.5
10 yr	-19.4	-23.0	4.7
5 yr	-1.9	-0.6	11.0
1 yr	-1.6	-0.8	12.3

Table 5.6: This studies' deviations to the values tabulated in ICRP 80 with regard to the absorbed dose for uterus, testicles and gall bladder wall.

for example the uterus and the testicles have deviations of no more than 2.2% with regard to the adult, 15-, 5-,and 1-year-old phantom but jolt up to 20% and more for the 10-year-old phantom. The gall bladder on the other side shows a good agreement for adult, 15-, and 10-year-old but differs considerably for the 5-,and 1-year-old phantom. The possible reasons for this individual outliers will be discussed in the next chapter on page 89.

Lung, skin, bone surface and thyroid

These organs show an overall poor agreement which is why they all were cross-checked with OLINDA/EXM calculations as can be sees table 5.7. The agreement with the OLINDA/EXM values is by no means better, in many cases (e.g. bones surface and lung) even worse. Interestingly enough there are cases where the agreement between the values tabulated in ICRP 80 and OLINDA/EXM is as bad as the agreement of this study and ICRP 80, e.g. the absorbed dose to lung at the pediatric stages and to bone surface for all age groups. A detailed discussion of these big deviations follows on page 93.

Organ	Phantom	Deviations to ICRP 80 [%]	Deviations to OLINDA/EXM [%]
Lung	Adult	21.4	22.3
	15 yr	6.7	15.8
	10 yr	13.4	20.8
	5 yr	9.6	21.0
	1 yr	8.9	21.2
Skin	Adult	-17.5	-13.9
	15 yr	-18.5	-13.3
	10 yr	-16.7	-10.6
	5 yr	-18.9	-8.8
	1 yr	-14.5	-3.8
Bone surface	Adult	-9.5	-33.4
	15 yr	-14.2	-38.4
	10 yr	-13.4	-31.0
	5 yr	-15.0	-29.1
	1 yr	-12.0	-33.9
Thyroid	Adult	8.2	10.9
	15 yr	2.8	7.7
	10 yr	11.7	19.0
	5 yr	13.5	23.8
	1 yr	15.3	29.0

Table 5.7: This studies' deviations to the values tabulated in ICRP 80 and calculations with OLINDA/EXM with regard to the absorbed dose for lung, skin, bone surface and thyroid.

Effective dose

The effective dose (see eq. 3.20) as dosimetric indicator for the total body's radiation burden was calculated according to ICRP 60 [60] and compared to the values tabulated in ICRP 80. As can be seen in figure 5.5 (the numerical values are listed in table 5.8) the accordance in excellent, never exceeding a relative deviation of ±3.7%.

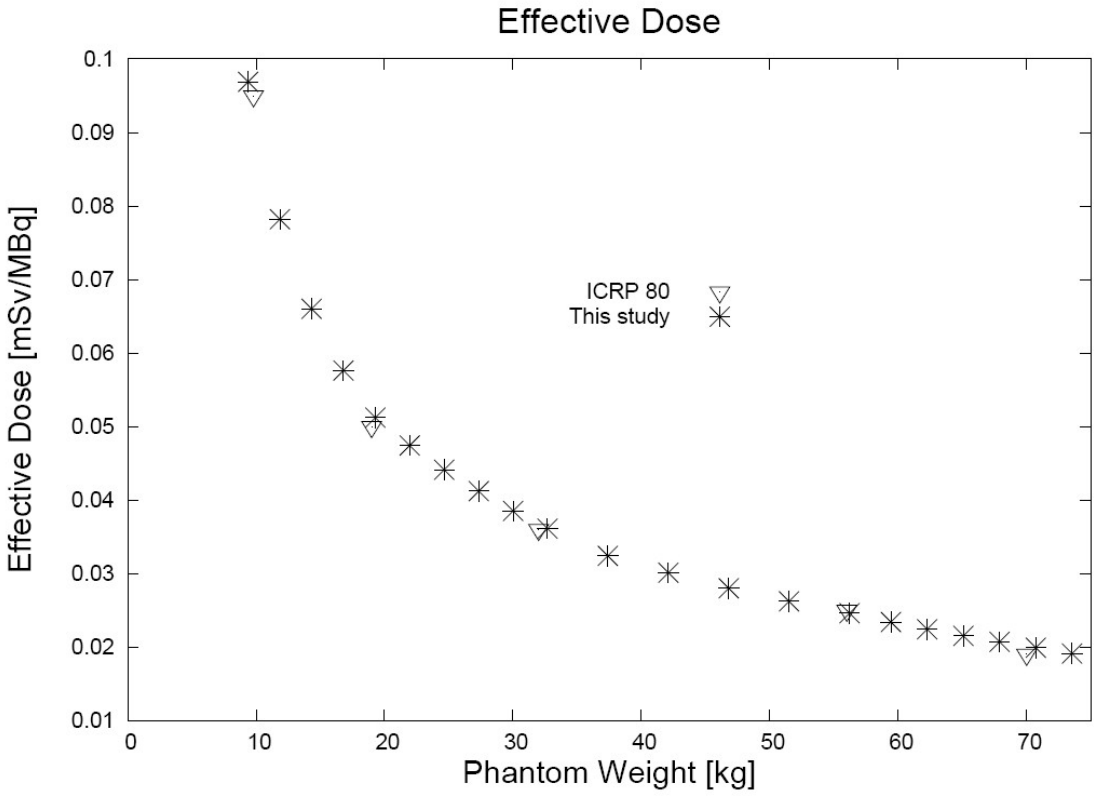

Figure 5.5: Calculated effective doses using biokinetics reported in ICRP 80.

	Effective Dose [mSv/MBq]	
Age	Ensemble	ICRP 80
1	9.77E-02	9.5E-02
2	7.87E-02	-
3	6.65E-02	-
4	5.81E-02	-
5	5.17E-02	5.0E-02
6	4.81E-02	-
7	4.51E-02	-
8	4.23E-02	-
9	3.95E-02	-
10	3.71E-02	3.6E-7
11	3.35E-02	-
12	3.10E-02	-
13	2.88E-02	-
14	2.68E-02	-
15	2.50E-02	2.5E-02
16	2.38E-02	-
17	2.28E-02	-
18	2.19E-02	-
19	2.10E-02	-
20	2.03E-02	1.9E-02*
21	1.94E-02	-

*see remark on page 63

Table 5.8: Calculated Effective Dose with biokinetics from [81] and subsequent comparison.

5.3 Comparison with MIRD 19 and OLINDA/EXM.

To compare the present calculations with the MIRD Dose Estimate Report No. 19, the weighted mean residence times reported there were used as biokinetic input, see table 4.3. The same data were used for the validation performed with OLINDA/EXM. Figure 5.6 compares our results, the concurrent calculations with OLINDA/EXM, and the reported dose estimates from MIRD Dose Estimate Report No. 19 for an adult phantom of approximately the same weight. The doses to testes and ovaries only consider residence times in urinary bladder and remainder of body, as done in MIRD 19 [80] and tabulated in the work of Hays and Segall [109].

All numerical values discussed in the following can be found in tables 5.9 to 5.15 on page 80 - 86. The most relevant finding certainly is that the doses calculated in this work almost all agree with the ones returned by OLINDA/EXM but considerably differ from MIRD Dose Estimate Report No. 19, as shown very clearly in Figure 5.7 on page 76. Once again, the dose to red marrow perfectly coincides when the King-Spiers factors are omitted (cf. page 64). With the exception of the lung the deviation between the results of the ensemble and the OLINDA/EXM calculations never exceed ±6.7%. Taking the average deviation of all the phantoms of all the target organs listed in MIRD 19 excluding the lung yields a value of only ±1.6%! This means that with regard to OLINDA/EXM this study's simulations show an astonishing agreement. Analogous to ICRP 80 the calculated absorbed doses for the lung show large disagreements which stretch up to ±16.4%. Figure 5.8 shows a three-dimensional depiction of the deviations to OLINDA/EXM including all age groups. The outlier with regard to the lung can be clearly seen on the right hand side. A more detailed discussion about the deviations for lung follows in the next section on page 94.

Another recognizable fact in figure 5.8 and of course in the numeric data tables is that the deviations with regard to testes and heart wall are much smaller than the ones observed in the comparison with ICRP 80 (cf. table 5.5 and 5.6). For example the huge discrepancy for the 10 year old phantom in the comparison with ICRP 80 (−23.0%) is only −5.3% in case of the comparison with OLINDA/EXM, applying the biokinetic input of MIRD 19. This seems highly paradox since both the ICRP and OLINDA/EXM rely on the same SAFs published by Cristy and Eckerman [63]. The origin of this discrepancy is explained in the discussion chapter on page 90.

As mentioned before and depicted in figure 5.7 the good agreement between the ensemble's results and OLINDA/EXM calculations faces the observation that the absorbed dose estimates reported in MIRD Dose Estimate Report No. 19

demonstrate a fairly good accordance for the liver, urinary bladder wall, spleen, and testes but tend to deviate by ±9% to ±43% with respect to all others. A detailed discussion about this can be found on page 88.

MIRD Dose Estimate Report No. 19 states the doses to ovaries and testes include only contributions from residence times in the urinary bladder and remainder of body, as calculated from data in Hays and Segall [109]. For the sake of completeness, an additional set of absorbed doses to the gonads was calculated with our simulation data and OLINDA/EXM considering all tabulated source organs. This leads to lower doses, as shown in figures 5.9 and 5.10 (numerical values see table 5.13 and 5.14). This can be easily explained. Since neither testes nor ovaries are considered source organs, the contribution from the remainder of the body plays a crucial role (cf. discussion on the absorbed dose to heart wall in section 6.2.2). The larger the number of source organs, the lower the estimated residence time for the remainder. Whereas the use of a complex biokinetic system with many source organs may cause a more precise dose assessment, the reduction to fewer source organs leads to a more conservative one.

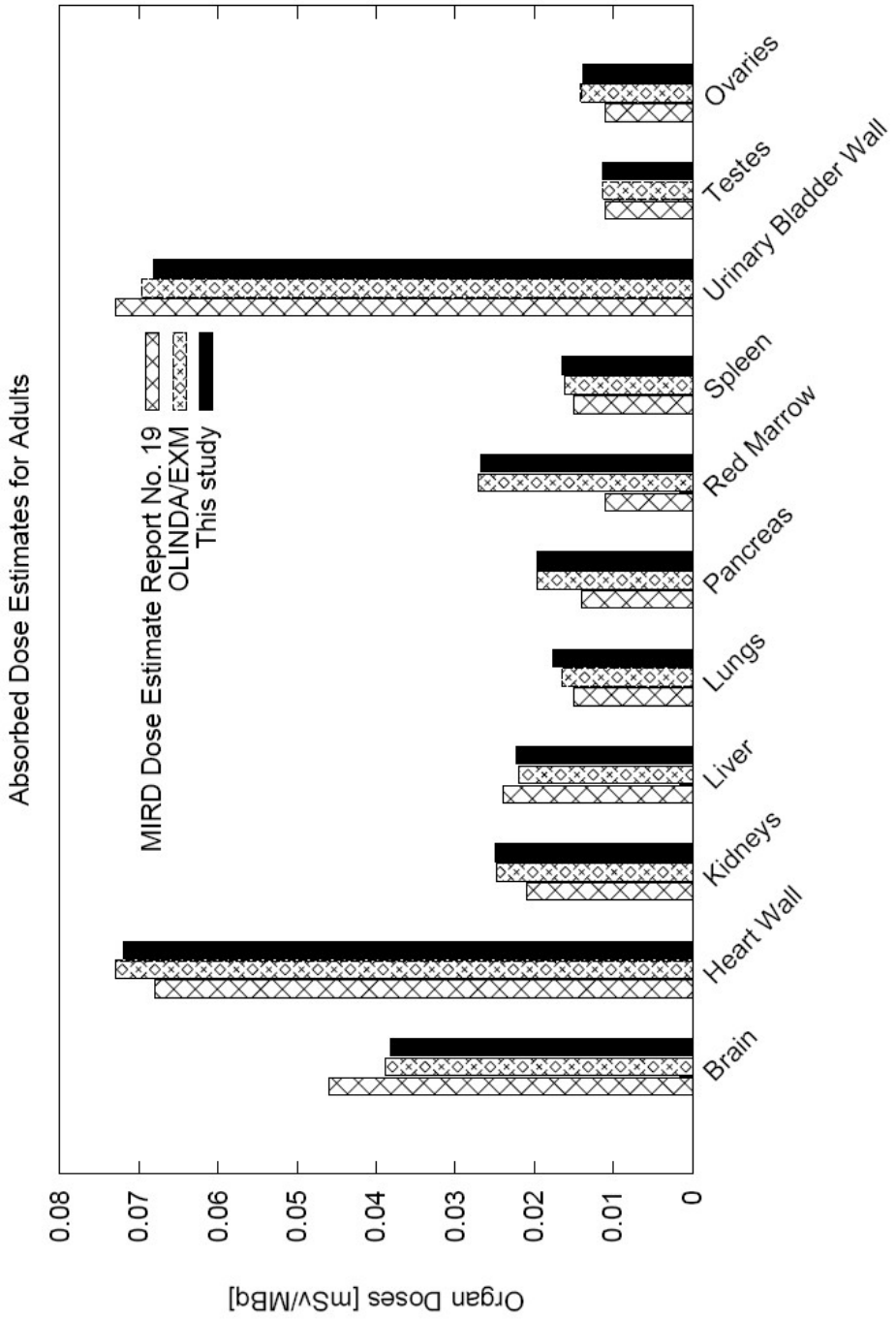

Figure 5.6: Absorbed doses using biokinetics reported in MIRD Dose Estimate Report No. 19 for this study's phantom with nominal age 21, OLINDA/EXMs adult, and MIRD Dose Estimate Report No. 19 data.

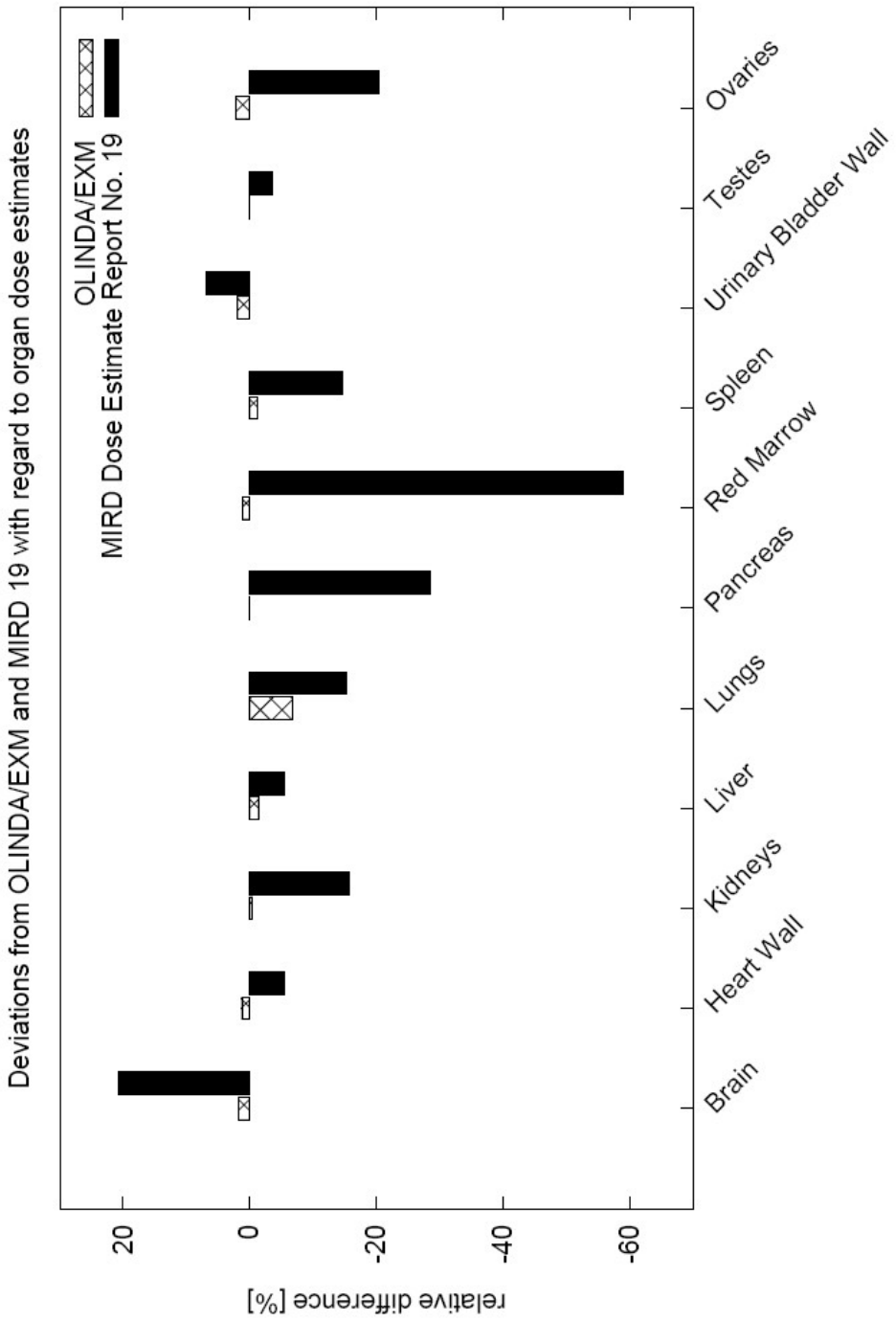

Figure 5.7: Relative differences in percent between this study, MIRD Dose Estimate Report No. 19 and calculations with OLINDA/EXM for this study's phantom with nominal age 21, OLINDA/EXMs adult, and MIRD Dose Estimate Report No. 19 data.

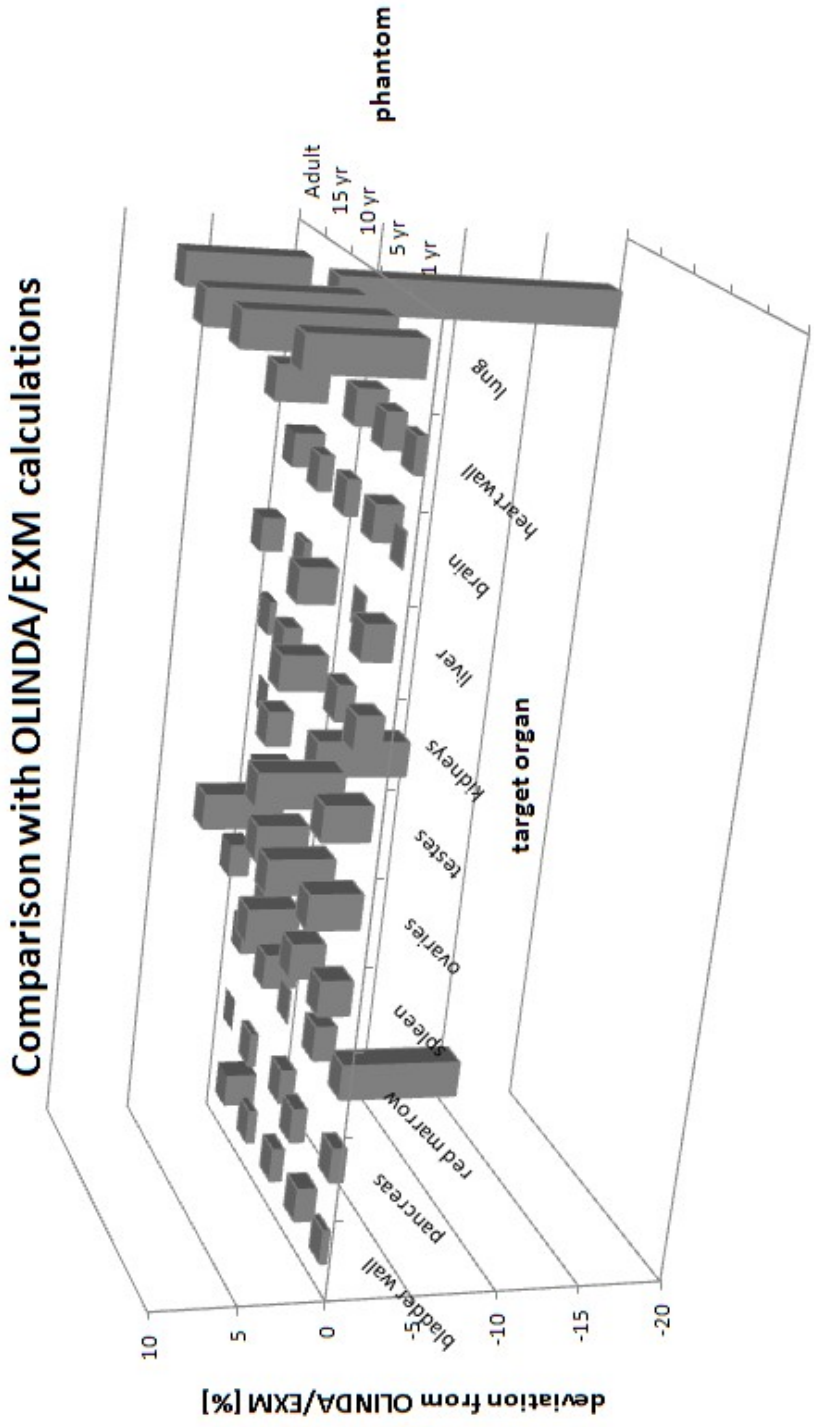

Figure 5.8: Relative differences in percent between this study and the concurrent calculations with OLINDA/EXM. The phantoms correspond to the Cristy/Eckerman series.

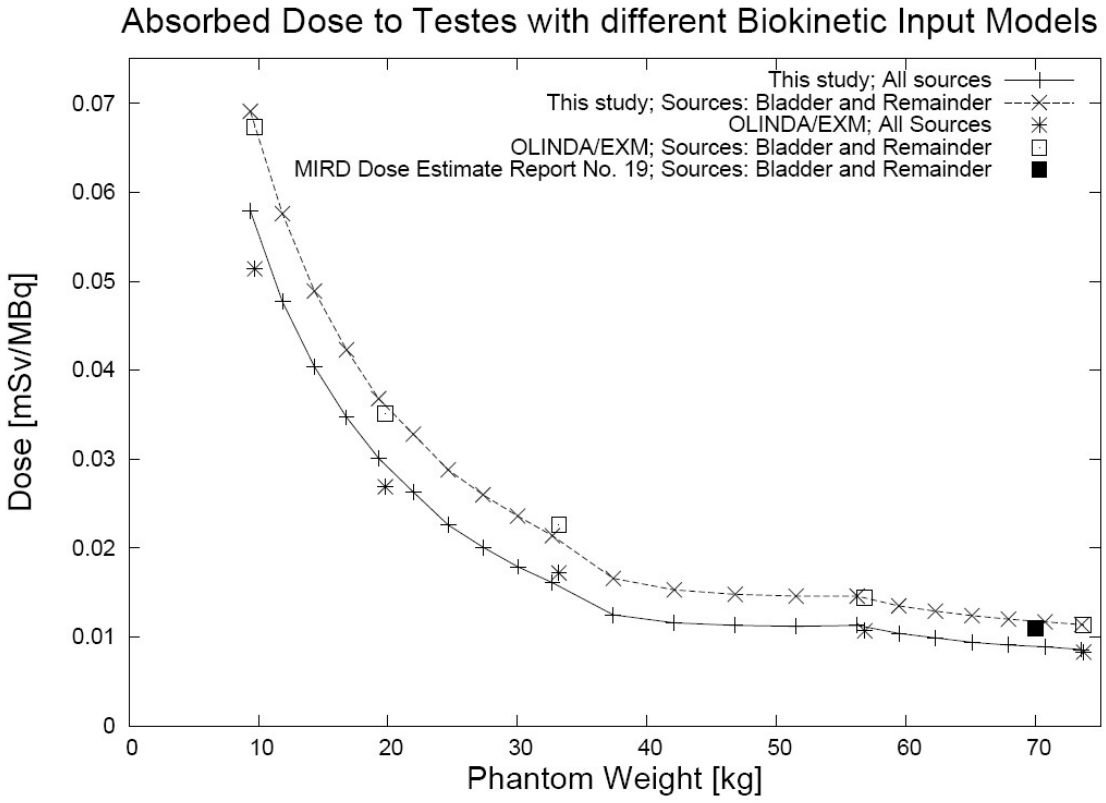

Figure 5.9: Absorbed doses to testes using biokinetics reported in MIRD Dose Estimate Report No. 19.

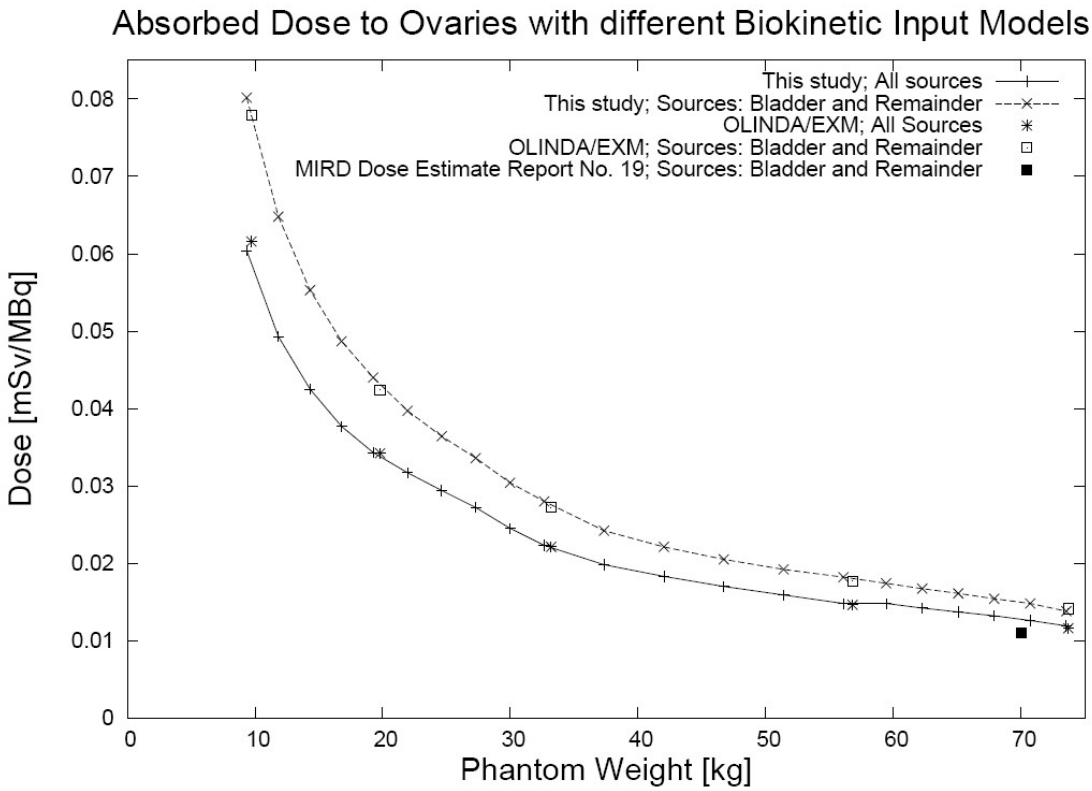

Figure 5.10: Absorbed doses to ovaries using biokinetics reported in MIRD Dose Estimate Report No. 19.

	Lungs [μSv/MBq]			**Pancreas [μSv/MBq]**		
Age[yr]	Ensemble	OLINDA/ EXM	MIRD 19	Ensemble	OLINDA/ EXM	MIRD 19
1	101	94.9	-	130	131	-
2	81.9	-	-	101.2	-	-
3	69.3	-	-	83.8	-	-
4	60.4	-	-	72.1	-	-
5	53.8	49.7	-	63.8	63.3	-
6	48.5	-	-	59.7	-	-
7	44.4	-	-	56.2	-	-
8	40.9	-	-	52.7	-	-
9	35.8	-	-	50.4	-	-
10	35.8	32.9	-	47.8	48.2	-
11	32.7	-	-	40.3	-	-
12	30.2	-	-	35.1	-	-
13	28.2	-	-	31.4	-	-
14	26.4	-	-	28.5	-	-
15	24.9	29.8	-	26.3	26.2	-
16	23.3	-	-	24.8	-	-
17	24.8	-	-	23.5	-	-
18	20.6	-	-	22.4	-	-
19	19.6	-	-	21.3	-	-
20	18.6	-	15†	20.4	-	14†
21	17.7	16.5*	-	19.6	19.6*	-

*OLINDA's default adult phantom has a weight of 73.7 kg (the ensemble phantom of nominal age 21 having 73.54).
†The phantom whose S-values were used in MIRD 19 has 70 kg (the ensemble phantom of nominal age 20 having 70.72)

Table 5.9: Absorbed Doses for **Lungs** and **Pancreas** with Biokinetics from MIRD Dose Estimate Report No. 19 [80]. This studies' results are refereed to as "Ensemble".

	Red Marrow[μSv/MBq]			**Spleen [μSv/MBq]**		
Age[yr]	Ensemble	OLINDA/ EXM	MIRD 19	Ensemble	OLINDA/ EXM	MIRD 19
1	205.3	220	-	96.6	94.9	-
2	155.4	-	-	79.7	-	-
3	125.3	-	-	68.1	-	-
4	104.6	-	-	59.7	-	-
5	91.3	92.4	-	53.8	52.8	-
6	80.8	-	-	48	-	-
7	72.6	-	-	43.7	-	-
8	58.1	-	-	40	-	-
9	53.5	-	-	37.2	-	-
10	49.7	49.7	-	34.7	33.7	-
11	44	-	-	31.2	-	-
12	39.7	-	-	28.4	-	-
13	35.8	-	-	26.1	-	-
14	32.9	-	-	24.2	-	-
15	30.5	31.1	-	22.5	22.4	-
16	29.2	-	-	21.1	-	-
17	28	-	-	19.9	-	-
18	29.9	-	-	18.8	-	-
19	28.8	-	-	17.9	-	-
20	27.8	-	11†	17.1	-	15†
21	26.8	27.1*	-	16.4	16.2*	-

*OLINDA's default adult phantom has a weight of 73.7 kg (the ensemble phantom of nominal age 21 having 73.54).
†The phantom whose S-values were used in MIRD 19 has 70 kg (the ensemble phantom of nominal age 20 having 70.72)

Table 5.10: Absorbed Doses for **Red Marrow** and **Spleen** with Biokinetics from MIRD Dose Estimate Report No. 19 [80]. This studies' results are refereed to as "Ensemble".

	Brain [μSv/MBq]			**Heart Wall [μSv/MBq]**		
Age[yr]	Ensemble	OLINDA/ EXM	MIRD 19	Ensemble	OLINDA/ EXM	MIRD 19
1	65.5	65.5	-	405.7	408	-
2	58.9	-	-	337.3	-	-
3	53.7	-	-	289.2	-	-
4	49.4	-	-	253.7	-	-
5	45.8	46.5	-	226.5	229	-
6	44.6	-	-	20.2	-	-
7	43.7	-	-	183.1	-	-
8	42.8	-	-	167.3	-	-
9	42	-	-	154.3	-	-
10	41.1	41.4	-	143.5	146	-
11	40.7	-	-	128.8	-	-
12	40.2	-	-	117.1	-	-
13	39.6	-	-	107.6	-	-
14	39.4	-	-	99.5	-	-
15	39	39.3	-	97.2	94.4	-
16	38.9	-	-	88.5	-	-
17	38.7	-	-	84.6	-	-
18	38.6	-	-	81.1	-	-
19	38.4	-	-	77.8	-	-
20	38.3	-	46†	74.9	-	68†
21	38.1	38.8*	-	72	72.9*	-

*OLINDA's default adult phantom has a weight of 73.7 kg (the ensemble phantom of nominal age 21 having 73.54).
†The phantom whose S-values were used in MIRD 19 has 70 kg (the ensemble phantom of nominal age 20 having 70.72). MIRD 19 states to neglect all sources but the brain, whereas the calculations for the ensemble and the concurrent ones with OLINDA/EXM consider all of them.

Table 5.11: Absorbed Doses for **Brain** and **Heart Wall** with Biokinetics from MIRD Dose Estimate Report No. 19 [80]. This studies' results are refereed to as "Ensemble".

	Kidney [μSv/MBq]			**Liver [μSv/MBq]**		
Age[yr]	Ensemble	OLINDA/ EXM	MIRD 19	Ensemble	OLINDA/ EXM	MIRD 19
1	110.6	109	-	117.9	116	-
2	92.4	-	-	96.1	-	-
3	79.7	-	-	81.6	-	-
4	70.3	-	-	71.3	-	-
5	63.1	62.5	-	63.6	63.3	-
6	57.6	-	-	58	-	-
7	53	-	-	53.4	-	-
8	49	-	-	49.5	-	-
9	45.9	-	-	46.3	-	-
10	43	41.9	-	43.4	42.5	-
11	39.5	-	-	39.3	-	-
12	36.6	-	-	36	-	-
13	34.1	-	-	33.2	-	-
14	32	-	-	30.9	-	-
15	30.1	29.8	-	28.9	28.8	-
16	29	-	-	27.5	-	-
17	28.1	-	-	26.2	-	-
18	27.2	-	-	25.1	-	-
19	26.4	-	-	24	-	-
20	25.6	-	21†	23.1	-	21†
21	24.9	24.8*	-	22.2	21.9*	-

*OLINDA's default adult phantom has a weight of 73.7 kg (the ensemble phantom of nominal age 21 having 73.54).
†The phantom whose S-values were used in MIRD 19 has 70 kg (the ensemble phantom of nominal age 20 having 70.72)

Table 5.12: Absorbed Doses for **Kidney** and **Liver** with Biokinetics from MIRD Dose Estimate Report No. 19 [80]. This studies' results are refereed to as "Ensemble".

	All [μSv/MBq]		Bladder and Remainder [μSv/MBq]		
Age[yr]	Ensemble	OLINDA/ EXM	Ensemble	OLINDA/ EXM	MIRD 19
1	60.4	61.6	80.2 ± 2.3	77.9	-
2	49.3	-	64.8 ± 1.9	-	-
3	42.5	-	55.3 ± 1.7	-	-
4	37.7	-	48.7 ± 1.5	-	-
5	34.3	34.2	44 ± 1.4	42.4	-
6	31.7	-	39.7 ± 1.3	-	-
7	29.4	-	36.4 ± 1.2	-	-
8	27.2	-	33.6 ± 1.1	-	-
9	24.5	-	30.4 ± 1.0	-	-
10	22.3	22.1	28 ± 0.9	27.2	-
11	19.8	-	24.2 ± 0.8	-	-
12	18.3	-	22.1 ± 0.8	-	-
13	17	-	20.5 ± 0.7	-	-
14	15.9	- [Fem. Adult]* (15-yr)	19.2 ± 0.6	- [Fem. Adult]* (15-yr)	-
15	14.8	[14.4]* (14.6)	18.2 ± 0.6	[17.4]* (17.7)	-
16	14.8	-	17.4 ± 0.6	-	-
17	14.2	-	16.7 ± 0.6	-	-
18	13.7	-	16.1 ± 0.6	-	-
19	13.2	-	15.4 ± 0.5	-	-
20	12.6	-	14.8 †± 0.5	-	11 †
21	11.9	11.6*	13.8 ± 0.5	14.1*	-

*OLINDA's default adult phantom has a weight of 73.7 kg (the ensemble phantom of nominal age 21 having 73.54).
†The phantom whose S-values were used in MIRD 19 has 70 kg (the ensemble phantom of nominal age 20 having 70.72)

Table 5.13: Absorbed Doses for **Ovaries**. The left column shows results considering all source organs listed in MIRD Dose Estimate Report No. 19 [80], the right column only urinary bladder and remainder of body as tabulated in the work of Hays and Segall [109]. This studies' results are refereed to as "Ensemble".

	All [μSv/MBq]		Bladder and Remainder [μSv/MBq]		
Age[yr]	Ensemble	OLINDA/ EXM	Ensemble	OLINDA/ EXM	MIRD 19
1	57.9	51.4	69.1 ± 2.0	67.3	-
2	47.7	-	57.6 ± 1.7	-	-
3	40.4	-	48.9 ± 1.5	-	-
4	34.7	-	42.3 ± 1.3	-	-
5	30.1	26.9	36.8 ± 1.1	35.1	-
6	26.3	-	32.8 ± 1.0	-	-
7	22.6	-	28.8 ± 0.8	-	-
8	20.1	-	26.0 ± 0.7	-	-
9	17.9	-	23.6 ± 0.7	-	-
10	16.1	17.2	21.4 ± 0.6	22.6	-
11	12.5	-	16.6 ± 0.4	-	-
12	11.6	-	15.3 ± 0.4	-	-
13	11.3	-	14.8 ± 0.4	-	-
14	11.2	-	14.6 ± 0.4	-	-
15	11.3	10.7	14.6 ± 0.5	14.4	-
16	10.4	-	13.5 ± 0.4	-	-
17	9.9	-	12.9 ± 0.4	-	-
18	9.4	-	12.4 ± 0.4	-	-
19	9.1	-	12.0 ± 0.4	-	-
20	8.9	-	11.7 ± 0.4	-	11†
21	8.6	8.3*	11.4 ± 0.4	11.4*	-

*OLINDA's default adult phantom has a weight of 73.7 kg (the ensemble phantom of nominal age 21 having 73.54).
†The phantom whose S-values were used in MIRD 19 has 70 kg (the ensemble phantom of nominal age 20 having 70.72)

Table 5.14: Absorbed Doses for **Testes**. The left column shows results considering all source organs listed in MIRD 19, the right column only urinary bladder and remainder of body as tabulated in Hays and Segall [109]. This studies' results are refereed to as "Ensemble".

	Urinary Bladder Wall [μSv/MBq]		
Age[yr]	Ensemble	OLINDA	MIRD 19
1	379.6	381	-
2	309.4	-	-
3	262.3	-	-
4	228.3	-	-
5	202.7	205	-
6	183.8	-	-
7	167.5	-	-
8	154.2	-	-
9	142.5	-	-
10	132.1	133	-
11	120.3	-	-
12	110.2	-	-
13	101.7	-	-
14	94.3	-	-
15	87.8	88.2	-
16	83.7	-	-
17	80.0	-	-
18	76.7	-	-
19	73.7	-	-
20	70.9	-	73†
21	68.3	69.6*	-

*OLINDA's default adult phantom has a weight of 73.7 kg (the ensemble phantom of nominal age 21 having 73.54.
†The phantom whose S-values were used in MIRD 19 has 70 kg (the ensemble phantom of nominal age 20 having 70.72)

Table 5.15: Absorbed Doses for **Urinary Bladder Wall**. with Biokinetics from MIRD Dose Estimate Report No. 19 [80]. This studies' results are refereed to as "Ensemble".

Chapter 6

Discussion

The aim of this work was to establish the basis toward an expansion of available reference phantoms in nuclear medicine by providing SAFs for an ensemble of 21 mathematical phantoms with differing weight and height and to test its validity by comparing it with calculations of previous reports by the example of ^{18}F-FDG. In the following the results presented in the previous chapter are discussed.

6.1 Dose to Red Marrow

The results for the red marrow (see figure 5.4, page 64) deserve a closer look. Both in the case of a pure target and in the case of being a source and target organ, the calculations show a very good agreement with ICRP 80 and OLINDA/EXM when the King-Spiers factors are omitted in the three-factor method. Interestingly enough, the SAFs published in the Oak Ridge reports were calculated by using a different method, namely the fluence to dose-response functions. The accordance of the particular calculation method chosen in this study with another procedure, based on a different approach using an unequal Monte Carlo code, is unlikely to be a coincidence. It is more likely that for calculations with MCNP, the energy deposition in the homogeneous mixture multiplied by the red bone marrow fraction for each particular bone and the ratios of mass energy absorptions coefficients of red marrow and skeletal mixture, respectively, reflects satisfactorily the absorbed dose in red marrow for photons of energy similar to that for annihilation radiation. Concerning the red marrow, another refinement for the dose assessment has to be taken into account apart from purely anatomic parameters, namely the actual age, but more precisely, the fact whether a patient is considered to be an adolescent or a grownup, which determines the total mass of red marrow. As seen in table 5.10 on page 81, there is a discontinuity between nominal ages 18 and 17, simply because the former is considered an adult and the later a juvenile, causing the

fraction and hence the mass of red marrow to increase and, therefore, the dose to decrease.

6.2 Observed deviations

6.2.1 MIRD Dose Estimate Report No. 19

To begin with the deviations to the available sources are discussed in detail. The worst agreement was observed between the ensemble's phantom with nominal age 21 and the data reported in MIRD Dose Estimate Report No. 19 [80] which corresponds to an adult phantom (see figure 5.7). MIRD 19 does not provide any data for pediatric phantoms. The differences are even more remarkable when taking into account that the agreement with concurrent OLINDA/EXM calculations is excellent! The big discrepancies of MIRD 19 can be explained by the fact that the data published there are averaged means from individual estimates rather than calculations with reference phantoms. The very good agreement with OLINDA/EXM therefore supports the use of reference phantoms for dose assessment of a patient with given weight and height since they are modeled to represent a certain population whereas averaging over individuals introduces a certain arbitrariness.

Moreover the dose to the brain stated in MIRD 19 cannot not be explained with any documented S-values. The tabulated value for the absorbed dose to brain in MIRD Dose Estimate Report No. 19 states 4.6×10^2 mGy/MBq with the remark that this value neglects all sources but the brain and that the brain mass was assumed to be 1400 g. This does not agree with all other data available. With a given residences time of 0.22 hours, the phantom with a comparable weight in this study yields 3.6×10^2 mGy/MBq and OLINDA/EXM 3.7×10^2 mGy/MBq. Applying S-values from yet another study exclusively dedicated to head and brain, namely MIRD Pamphlet No. 15 [110], results in 3.6×10^2 mGy/MBq. If all source organs are considered, this study yields 3.8×10^2 mGy/MBq. The values stated by MIRD 19 is therewith 24% to 28% higher than any documented value and beyond that mathematically not replicable. In addition to this, the contribution from the other sources but the brain cannot said to be completely negligible as claimed by MIRD 19 since they make up 5.2% of the dose absorbed in brain.

The bottom line of the comparison with MIRD 19 is that a dose assessment with the help of averaged means from individual estimates does not yield reproducible results in the way calculations with reference phantoms do. Facing the inconsistency with regard to the listed absorbed dose in brain MIRD Dose Estimate Report No. 19 should be revised.

6.2.2 OLINDA/EXM and ICRP 80

When discussing the differences to the values stated by ICRP and the OLINDA/EXM calculations two groups are identified:

1. **Outliers:** This group contains organs showing one or both of the following phenomena: (I) One or two phantoms show a poor agreement whereas the majority has a very good accordance or (II) absorbed dose values show considerable deviations when applying the bionkinetic data from ICRP 80 but demonstrate a good agreement with biokinetic data from MIRD 19.

2. **General discrepancies:** This group contains organs for which the absorbed dose shows a poor agreement with regard to ICRP 80 and OLINDA/EXM calculations as well as all phantoms.

Outliers

This group contains the results of heart wall, testicles, uterus and gall bladder. The latter two are listed by ICRP 80 but not by MIRD 19 which is why with regard it concurrent OLINDA/EXM calculations only biokinetics of ICRP 80 were applied. As mentioned on page 69 the dose to testicles show a huge outlier with regard to the 10-years old phantom that appears when comparing it to both the results of ICRP 80 (see table 5.6) as well as concurrent OLINDA/EXM calculations applying IRCP's biokinetic data (see table 6.1). Investigating the entire dose calculation procedure, hence checking the different SAFs contribution to the absorbed dose of the testicles one finds out that $\Phi(\text{testicles} \leftarrow \text{urinary bladder content}, E_\gamma)$ is responsible for the huge deviation. The same goes for the absorbed dose to uterus where $\Phi(\text{uterus} \leftarrow \text{urinary bladder content}, E_\gamma)$ is virtually the main cause for the observed deviations. Figure 6.1 shows the deviation of the aforementioned SAFs when compared to the Cristy and Eckerman values. A close inspection of the pediatric anatomy BodyBuilder creates at the age group of 10 reveals that for no particular reason the bladder is situated more in the rear section of the trunk. The organ's different anatomic placement starts at about the phantom age of 13 and again is moved towards the front section of the trunk for phantoms younger than 10 years, the deviation with regard to the 5- years old phantom returning to small values like before. This geometrical discontinuity has of course a big impact on the SAFs in question since enlarging the distance between source and target organ, i.e. urinary bladder on the one side and testicles as well as uterus on the other, naturally decreases the respective $\Phi(r_T \leftarrow r_S, E_i)$. Since there is no anatomic justification for this misplacement it has to be an errors caused somewhere in the BodyBuilder routines. Interesting enough when comparing this studies results with concurrent OLINDA/EXM calculations referring to biokinetics of MIRD 19 rather

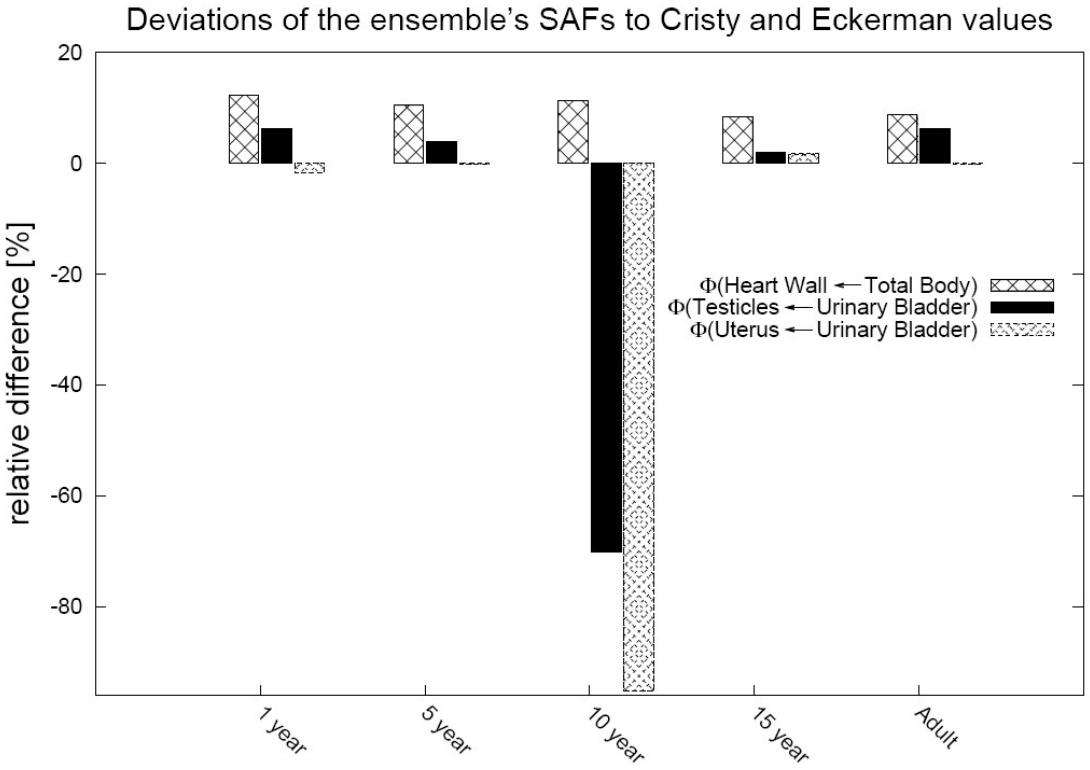

Figure 6.1: Deviation of this studies' SAFs responsible for the outliers to the Cristy and Eckerman values.

than ICRP 80 (see table 6.1) the difference in the absorbed dose to testicles for the 10 years-old phantom becomes much smaller, shrinking from -17% to -1.7%, a factor of 10! Bearing in mind that in all the calculations the very same SAFs were used this seems totally unexplainable at first glance. However when analyzing the biokinetic data of ICRP 80 and MIRD 19 the cause becomes evident. As mentioned in the paragraph above the cause for the deviations are $\Phi(\text{testicles} \leftarrow \text{urinary bladder content}, E_\gamma)$ as well as $\Phi(\text{uterus} \leftarrow \text{urinary bladder content}, E_\gamma)$. Taking a look at the outer right columns of table 6.1 one can see that the fraction of the residence time of the urinary bladder contents with regard to the residence time of the total body is much smaller in the case of MIRD 19's biokinetics than in the case of ICRP 80. Consequently the sharp discontinuity of the respective SAfs for the 10 years-old phantoms is much more weighted with the biokinetics of ICRP 80. The same explanation can be applied to the observed effects in the absorbed dose to the uterus which is not listed in MIRD Dose Estimate Report

		Deviation to Ensemble[%]		τ_{UB}/τ_{TB}	
Organ	Phantom	Biokinetics ICRP 80	Biokinetics MIRD 19	Biokinetics ICRP 80	Biokinetics MIRD 19
Testicles	Adult	5.6	-1.2	0.76	0.59
	15 yr	3.6	3.0	0.76	0.59
	10 yr	-17.0	-1,7	0.77	0.59
	5 yr	8.5	-1,1	0.79	0.59
	1 yr	8.9	-0.6	0.79	0.59
		Deviation to Ensemble[%]		τ_{REM}/τ_{TB}	
Organ	Phantom	Biokinetics ICRP 80	Biokinetics MIRD 19	Biokinetics ICRP 80	Biokinetics MIRD 19
Heart wall	Adult	9.7	-1.2	0.76	0.59
	15 yr	10.0	3.0	0.76	0.59
	10 yr	5.6	-1,7	0.77	0.59
	5 yr	6.9	-1,1	0.79	0.59
	1 yr	9.3	-0.6	0.79	0.59

Table 6.1: This study's deviations to calculations with OLINDA/EXM with regard to the absorbed dose in testicles and heart wall. Biokinetics reported in ICRP 80 and MIRD 19 are applied. The two columns on the right show the respective fraction of the residence time in the remaining tissue with regard to the total body for the case of the heart wall and the fraction of the residences time in the urinary bladder with regard to the total body for the case of the testicles.

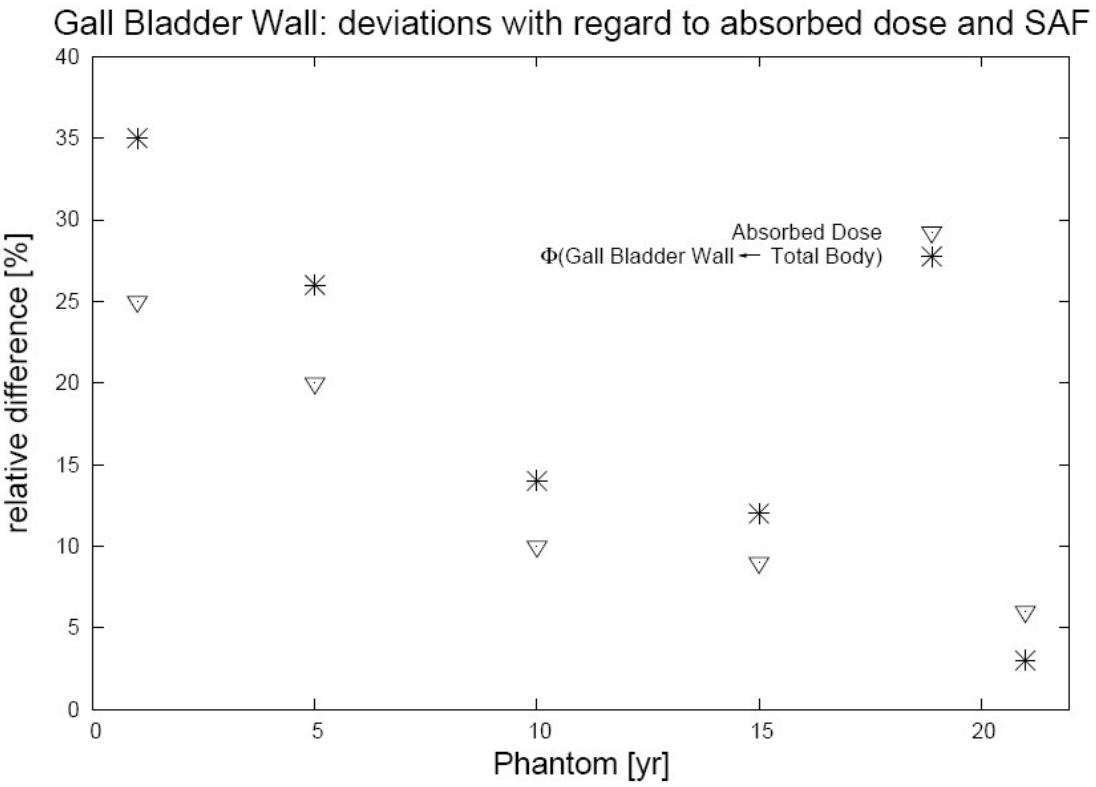

Figure 6.2: Deviations of this study's Φ(gall bladder wall $\leftarrow$ total body, E_γ) to the Cristy and Eckerman values as well as this study's absorbed dose for the gall bladder wall when applying biokinetics from ICRP 80 to concurrent OLINDA/EXM calculations.

No. 19. The heart wall on the other side is listed in MIRD Dose Estimate Report No. 19 and shows the same phenomena as testicles and uterus: When comparing OLINDA/EXM calculations and this study applying biokinetics from ICRP 80 the deviations are high but when applying MIRD 19 data they are very low (see table 6.1). In this case the responsible SAF is Φ(heart wall $\leftarrow$ total body, E_γ) which deviates to the Cristy/Eckerman values $\approx +9\%$ to $+12\%$ (see Figure 6.1). Analogous to the previous discussion about testicles and uterus the fraction of the corresponding residence times tips the balance (see table 6.1). For this purpose one has to understand that in a dosimetric calculation according to the MIRD system $\Phi(r_T \leftarrow$ total body, $E_\gamma)$ is situated within the term that gets multiplied with the residence time of the remaining tissue as can be seen in equation 3.17.

Hence the lower the contribution of the residences times of the distinctive source organs the higher τ_{REM} and the bigger its influence on the absorbed dose.

Finally the last organ with outliers in the calculation is the gall bladder wall where the 1- and 5-years old phantoms show considerable divergences. Analysis of the dose calculation showed $\Phi(\text{gall bladder wall} \leftarrow \text{total body}, E_\gamma)$ to be responsible factor. One can see in Figure 6.2 the deviation with regard to the absorbed does and $\Phi(\text{gall bladder wall} \leftarrow \text{total body}, E_\gamma)$ run pretty much parallel. As for the cause for this observation it has to be the specific modeling of the gall bladder in the pediatric stages of BodyBuilder.

General discrepancies

The organs whose calculated absorbed doses show discrepancies to the values listed by ICRP 80 and concurrent OLINDA/EXM calculations with regard to all phantom ages are lung, skin, bone surface and thyroid. Table 5.7 on page 70 cites the deviations. Additionally the lung, an organ also listed in MIRF 19, shows discrepancies when inserting MIRD 19 biokinetics into OLINDA/EXM, see figure 5.8 on page 77.

The results with regard to the absorbed dose to bone surface are way off the records as listed in table 5.7. Although mentioned in literature [99], the method of applying a well established Monte Carlo code and referring to the absorbed dose to the skeletal mixture as a conservative estimate for the dose to bone surface clearly fails since it results in a considerable underestimation of the dose, i.e. the contrary to a conservative estimate. The question remains if a different Monte Carlo code would yield a better agreement, however for future dose calculation it seems recommendable to use more sophisticated bone dosimetry models like the Fluence-to-dose response (FDR) functions (cf. page 56) as performed by OLINDA/EXM. Since the ICRP also relies on the FDR-functions and the corresponding SAFs $\Phi(\text{bone surface} \leftarrow r_S, E_\gamma)$ developed by Cristy and Eckerman the disagreement between the values listed in ICRP 80 and OLINDA/EXM calculations using the same biokinetics should be investigated.

Absorbed dose values to skin and thyroid also show big general discrepancies, see table 5.7. Although there is a slight tendency to smaller errors for phantoms of a younger age group in the case of skin and the reverse trend in case of thyroid it is not meaningful to derive a general behavior. Rather the investigation of the different SAFs $\Phi(\text{skin} \leftarrow r_S, E_\gamma)$ shows that all of them tend to underestimate the SAF. The skin is unique among the organs considered for dose calculations because it has a very small extension in one particular dimension which is the skin's thickness. Hence, an isotropic radiation source within a human body produces very short photon tracks within the skin, lowering the energy deposition as well as the statistical significance. For future works extended studies on using different Monte

Carlo codes, different modes of tracking secondary electrons and different skin models are recommended. In the case of the thyroid it is possible to identify a single SAF mainly responsible for the deviations, namely $\Phi(\text{thyroid} \leftarrow \text{total body}, E_\gamma)$. As in the case of the gall balder wall the specific model produced by BodyBuilder should be revised.

Finally the organ whose absorbed doses do not agree with any of the available data in literature is the lung . The reason can be found in the SAF $\Phi(\text{lung} \leftarrow \text{total body}, E_\gamma)$. Whereas MIRD 11 [61] tabulates $5.36 \times 10^6 \text{g}^{-1}$ and Cristy and Eckerman [63] calculated 4.9×10^6 , the calculations in this study yielded $6.76 \times 10^6 \text{g}^{-1}$. An obvious explanation would be differences in calculation methods for photon interaction in the lung tissue between MCNP and the Monte Carlo code at Oak Ridge Laboratories, which was used to asses the SAFs, ICRP and OLINDA/EXM are relying on. In spite of that, the SAFs $\Phi(\text{lung} \leftarrow \text{lung}, E_\gamma)$ of the aforementioned sources show a good agreement. Moreover the voxel phantom "Golem" from the GSF [65, 66, 67, 56] for example has an SAF $\Phi(\text{lung} \leftarrow \text{total body}, E_\gamma)$ of $6.9 \times 10^6 \text{g}^{-1}$ in this energy domain. The discrepancy of all these sources suggest that this quantity may vary somewhat due to phantom geometry and Monte Carlo codes used and should be investigated more closely in future work.

6.3 Limitations, Reliability and Applicability

Limitations of simulation model

A factor limiting the accuracy of our results certainly is the assumption of a homogeneous activity distribution throughout the source organs and the use of mean absorbed organ doses. Although there do exist studies relying on heterogeneous activity distribution as well as heterogeneous dose distributions for certain source- and target organs, this study used homogeneous models in order to compare it with comprehensive data given in both MIRD Dose Estimate Report No. 19 and ICRP Publication 80. Also it has to be mentioned at this point that the SAFs by references [61] and [63] were calculated for discrete steps of monoenergetic photons, whereas in this study, we ran a simulation with photons of exactly 511 keV. However the effects from that should be negligible, especially when incorporated in a full internal dose calculation.

Reliability

A very essential issue of this work is to discuss the general reliability of mathematical, stylized phantoms when it comes to SAFs. One could argue that that theses

kind of phantoms incorrectly assess organ-to-organ photon cross-fire as the simplistic geometric shapes used to model individual organs disallow realistic modeling of the surface-to-surface contact, their 3D shape, depth, and position within the body. Thus creating a series of new mathematical phantoms would be outdated and prolong known deficiencies rather than improve the ability to correctly assess individual and patient-specific organ dosimetry in nuclear medicine.

However several studies proved otherwise: Petoussi-Henss and co-workers [56] performed calculations for the mathematical MIRD phantom and several voxel phantoms regarding the absorbed dose per administration of certain radiopharmaceuticals. The results clearly showed that the doses were comparable and that deviations between voxel and MIRD organ doses are of the same order as the deviations between the various voxel models. In other words, choosing a particular voxel phantom as a reference models equally leads to dose deviations because of their individual anatomy.

Other studies confirm that calculations with stylized mathematical phantoms lead to comparable results with voxel models. Petoussi-Henss and Zankl [111] showed that for the calculation of organ equivalent dose voxel- and MIRD-type phantoms lead to comparable results, also and especially for pediatric phantoms. In the same study it is also noted that large discrepancies in SAFs occur for photon energies < 50 keV, whereas the agreement for higher energies is much better (cf. this study: 511 keV).

As for the effective dose, both studies above, as well as Zankl et al. [112] state clearly that regarding this quantity the differences between voxel and MIRD-type phantoms vary even less. Therefore using mathematical phantoms like in this study in order to assess the effective dose seems more than reasonable. To round up the justification of using stylized phantoms another recent publication should be pointed out which emphasizes the continuing need for stylized pediatric phantoms in medical dosimetry, namely the work of Han, Bolch and Eckerman [113]. There the continuing need for mathematical approximation is outlined, filling the gaps left open by voxel phantoms, i.e. the missing of a comprehensive series of reference pediatric tomographic phantoms and their disability to simulate very fine anatomic structures.

Applicability

As outlined in detail in subsection 3.3.2 the basis idea of this study was to expand the Cristy and Eckerman series into a whole ensemble in order to enable a more individual dose assessment by selecting the phantom that matches the patient closest according to physiognomic parameters, such as height and weight. (see figure 3.8). Therefore the primary aim of this study was definitely achieved since for the first time SAFs can be calculated for an ensemble ranging from the physiognomy

of a 1 year old up to an adult with a discretization into so many phantoms, that the absorbed dose to an organ or to the whole body as a function of a phantom parameter such as weight can be depicted as a smooth curve. This is demonstrated in figures like 5.5 (page 71), 5.9 (page 78) and 5.10 (page 79). In principle every single one of the tables 5.9 to 5.15 represents such a smooth curve of the absorbed dose as a function of a specific physiognomic parameter.

Reviewing the motivation of this study in subsection 3.3.2 it should be clarified once more at this point that this work aims towards a more individual whole body dose assessment in those applications of nuclear medicine, which *do not necessarily perform CT or MR scans* as a part of their clinical routine. In nuclear diagnostics for the majority of applications accompanying anatomical imaging is not performed. Therefore techniques that base on voxel- or hybrid phantoms (see page 38) can't be applied. Without the information of the individual anatomy of the patient one therefore has to rely on reference models.

When it comes to therapeutic procedures like TRT one could argue that treatment planning based on voxel models or hybrid phantoms of only a few primary organs will address the issue of individualizing organ dosimetry and normal organ toxicity by processing *partial* body CT or MR scans in a few hours. However this argument misses two essential facts. First of all this technology is not yet implemented in clinical infrastructure. Secondly and more important, applying the MIRD-system implies adding up the contribution from *all source organs* which is realized in OLINDA/EXM by entering the residence time of the explicit source organs and the remainder, hence the activity that distributes within the rest of the body. By focusing only on the contribution of a few primary organs and neglecting the rest one consequently underestimates the dose, which clearly is not in the interest of the patient. Admittedly, there are many cases in TRT where only a few or even a single source organ contributes to the bulk of the organ dose and where the remainder's contribution remains minimal, but there are plenty of examples appearing otherwise. Let's just consider the case of radiotoxicity of red marrow, one of the crucial tissues in TRT. Especially in the therapy of bone metastases and bone pain with radiopharmaceuticals the dose to red marrow is the major limiting factor [33, 114]. Since in the course of such a treatment the bone seeking radionuclides will enrich on the surface of all bone, an accurate dosimetry requires data of the whole skeleton.

Of course treatment planning in TRT is primarily focused on the organs at risk, hence the organs that contain tumors or become source organs due to other biokinetic reasons. But that doesn't mean that whole body dosimetry is not important for assessing the *overall radiation burden*. Even when applying small amounts of tracer material, like e.g. in nuclear diagnostics medical physicists routinely should asses the dose to the whole body by defining regions of interest (ROIs), estimating the residence times and performing calculations with software like OLINDA/EXM.

Last but not least whole body dosimetry is also a legal issue. In the EU Council Directive 97/43/Euratom [115] on health protection of individuals against the dangers of ionizing radiation in relation to medical exposure (member states of the EU have to transpose EU Council Directives into national law) patient dosimetry is embedded as a part of the optimization and refers to the dose the patient receives as a whole. Therefore focusing only on a few primary organs does not comply with these requirements. Moreover there are cases where an assessment of individual patient dose is explicitly prescribed, more precisely, if patients voluntarily accept to undergo an experimental diagnostic or therapeutic practice. This applies for example to clinical studies which test new tracers.

Concluding the use of an expanded ensemble of phantoms is reasonable for whole body dosimetry, most notable in nuclear diagnostics with the absence of CT or MR scans. Numerous studies prove the values for absorbed organ dose to be comparable with realistic voxel models. In this way, this study - the expansion of the Cristy and Eckerman series into 21 phantoms - should be seen as an alternative way to cope with the challenge of a more patient-specific does assessment. It serves as a complementation for the individualization option of OLINDA/EXM. MCNP is a long-established radiation transport code, and our results are a confirmation for the widely used SAFs produced by Cristy and Eckerman. The enlargement of the available array of phantoms creates a bigger diversity and, therefore, enables a more individual dose assessment. The next logical step is to extend the current work to develop SAFs and dose factors for photons across a broad energy range.

Chapter 7

Concluding Remarks

This study aimed to provide a more individual dose assessment in nuclear medicine as compared to the existing methods by broadening the supply of phantoms and their respective SAFs. An ensemble of 21 mathematical phantoms was submitted to the Monte Carlo Code MCNP4c2 for the purpose of calculation of SAFs for annihilation radiation. These values were incorporated into an internal dose assessment following the Medical Internal Radiation Dose (MIRD) schema and relying on published biokinetic data by ICRP Publication No. 80 [81] and MIRD Dose Estimate Report No. 19 [80] for intravenous administration of ^{18}F-FDG. The results were compared to organ absorbed dose values listed in ICRP 80, MIRC 19 and concurrent calculations with OLINDA/EXM applying the respective biokinetics.

The very good statistical properties of the simulations demonstrated the mathematical reliability as well as the very small uncertainties for individual SAFs. Comparison of the absorbed organs doses calculated for the ensemble with the values listed in abovementioned literature and complementing OLINDA/EXM calculations in the case of reference models and common age groups showed an extraordinary good accordance. Only 4 out of 25 organs show general deviations to big to label them insignificant. Additional some individual SAFs show discordances due to non satisfactory anatomic modeling by the BodyBuilder software. Considering the total amount of 14580 calculated SAFs this confirms the widely used SAFs by Cristy and Eckerman that were calculated more than 20 years ago using a different Monte Carlo code and validates the results of the ensemble that considerably increases the number of available reference phantom and hence refines the dose assessment for the individual.

The good accordance of the reference models among themselves with regard to absorbed dose values on the one hand and their comparatively big deviations to

the values of MIRD 19 which are averaged means from individual estimates on the other hand underlines the use of the former. The fact that the majority of nuclear exams don't involve any form of additional anatomic imaging further endorses the use of reference models. The ensemble presented here represents the biggest collection of reference models up to date and therewith the biggest possible level of individual dose assessment in nuclear diagnostics. More detailed, voxel-based dosimetry definitely will prevail in therapeutic applications when it comes to therapy planning of the organs at higher risk but even there the assessment of the overall radiation burden is very unlikely to be carried out on the base of a whole body representation of the individual patient. Hence, the use of a big ensemble will always be of interest as a completing analysis of the expected health hazard. The later complies with the increasing trend towards personalized medicine and quantification of undesired side effects.

List of Figures

List of Tables

Bibliography

[1] M. Blaickner and P. Kindl. Diversification of Existing Reference Phantoms in Nuclear Medicine: Calculation of Specific Absorbed Fractions for 21 Mathematical Phantoms and Validation Through Dose Estimates Resulting from the Administration of ^{18}F-FDG. *Cancer Biother Radiopharm*, 23(6):767–82, 2008.

[2] K. Facey et al. Overview of the clinical effectiveness of positron emission tomography imaging in selected cancers. *Health Technol Assess.*, 11(44):iii-iv, xi-267, 2007.

[3] R. Sabbatini. File:iodine-131-scintigraphy.jpg - wikipedia, the free encyclopedia. http : //en.wikipedia.org/wiki/File : Iodine − 131 − Scintigraphy.jpg, August 2009.

[4] S.R. Cherry, J.A. Sorenson, and M.E. Phelps. *Physics in nuclear medicine*. Saunders, 2003.

[5] A. Elhendy, J.J. Bax, and D. Poldermans. Dobutamine stress myocardial perfusion imaging in coronary artery disease. *J Nucl Med*, 43(12):1634-46, 2002.

[6] F.J. Bonte et al. Tc-99m HMPAO SPECT in the differential diagnosis of the dementias with histopathologic confirmation. *Clin Nucl Med*, 31(7):376-8, 2006.

[7] M.N. Wernick and J.N. Aarsvold. *Emission tomography: the fundamentals of PET and SPECT*. Academic Press, 2004.

[8] J. Langer. File:pet-mips-anim.gif - wikipedia, the free encyclopedia. http : //en.wikipedia.org/wiki/File : PET − MIPS − anim.gif, August 2009.

[9] S.D. Shorvon. A history of neuroimaging in epilepsy 1909-2009. *Epilepsia*, 50 Suppl(3):39–49, 2009.

[10] A.N. Clark and G.A. Beller. The present role of nuclear cardiology in clinical practice. *Q J Nucl Med Mol Imaging*, 49(1):43-58, 2005.

[11] J.M. Stone. Imaging the glutamate system in humans: relevance to drug discovery for schizophrenia. *Curr Pharm Des*, 15(22):2594-602, 2009.

[12] Klinikum der Universität München. Klinikum der Universität München - Urologie - PET-CT beim Prostatakarzinom. http : //uro.klinikum.uni − muenchen.de/pet − ct.html, December 2004.

[13] C. Kuntner et al. Limitations of small animal PET imaging with [18F]FDDNP and FDG for quantitative studies in a transgenic mouse model of alzheimer's disease. *Mol Imaging Biol*, 11(4):236-40, 2009.

[14] M.E. Phelps. *PET: physics, instrumentation, and scanners*. Springer, 2006.

[15] D. Delbeke and O. Israel. *Hybrid PET/CT and SPECT/CT Imaging: A Teaching File*. Springer, 2009.

[16] W.H. Beierwaltes. The treatment of thyroid carcinoma with radioactive iodine. *Semin Nucl Med*, 8(1):79-94, 1978.

[17] R. A. Pattillo et al. Phosphorus-32-chromic phosphate for ovarian cancer: I. fractionated low-dose intraperitoneal treatments in conjunction with platinum analog chemotherapy. *J Nucl Med*, 36(1):29–36, 1995.

[18] A.J. Jacobs et al. A phase I trial of a rhenium 186-labeled monoclonal antibody administered intraperitoneally in ovarian carcinoma: toxicity and clinical response. *Obstet Gynecol*, 82(4 Pt 1):586–93, 1993.

[19] P. Riva et al. Intralesional radioimmunotherapy of malignant gliomas. an effective treatment in recurrent tumors. *Cancer*, 73(3 Suppl):1076–82, 1994.

[20] B. Shapiro et al. Radiopharmaceutical therapy of malignant pheochromocytoma with [131I]metaiodobenzylguanidine: results from ten years of experience. *J Nucl Biol Med*, 35(4):269–76, 1991.

[21] A. Frilling et al. Role of radiolabeled octreotide therapy in patients with metastatic neuroendocrine neoplasms. *Exp Rev Endocrinology Metabolism*, 2(4):517–27, 2007.

[22] G.L. DeNardo et al. Pharmacokinetic characterization in xenografted mice of a series of firstgeneration mimics for HLA-DR antibody, lym-1, as carrier molecules to image and treat lymphoma. *J Nucl Med*, 48(8):1338–47, 2007.

[23] B.J. Hicke et al. Tumor targeting by an aptamer. *J Nucl Med*, 47(4):668–78, 2006.

[24] T.A. Waldmann. Monoclonal antibodies in diagnosis and therapy. *Science*, 252(5013):1657–62, 1991.

[25] J.W. Park. Liposome-based drug delivery in breast cancer treatment. *Breast Cancer Res*, 4(3):95–99, 2002.

[26] J.F. Kukowska-Latallo et al. Nanoparticle targeting of anticancer drug improves therapeutic response in animal model of human epithelial cancer. *Cancer Res*, 65(12):53517–24, 2005.

[27] G. Liu et al. Successful radiotherapy of tumor in pretargeted mice by 188re-radiolabeled phosphorodiamidate morpholino oligomer, as synthetic DNA analogue. *Clin Cancer Res*, 12(16):4958–64, 2006.

[28] R.J. Lewandowski et al. ^{90}Y microsphere (TheraSphere) treatment for unresectable colorectal cancer metastases of the liver: Response to treatment at targeted absorbed doses of 135 - 150 Gy as measured by 18F-fluorodeoxyglucose positron emission tomography and computer tomographic imaging. *J Vasc Interv Radiol*, 16(12):1641–51, 2005.

[29] A.S. Kennedy et al. Resin ^{90}Y-microsphere brachytherapy for unresectable colorectal liver metastases: Modern USA experience. *Int J Radiat Oncol Biol Phys*, 65(2):412–25, 2006.

[30] L.E. Williams, G.L. DeNardo, and R.F. Meredith. Targeted radionuclide therapy. *Med Phys*, 35(7):3062–68, 2008.

[31] S. Pauwels et al. Practical Dosimetry of Peptide Receptor Radionuclide Therapy with ^{90}Y-labeled Somatostatin Analogs. *J Nucl Med*, 46(1 suppl):92S–98, 2005.

[32] Y. Dewaraja et al. Accurate Dosimetry in ^{131}I Radionuclide Therapy Using Patient-Specific, 3-Dimensional Methods for SPECT Reconstruction and Absorbed Dose Calculation. *J Nucl Med*, 46(5):840–849, 2005.

[33] S. M. Goddu et al. Marrow Toxicity of ^{33}P- versus ^{32}P-Orthophosphate: Implications for Therapy of Bone Pain and Bone Metastases. *J Nucl Med*, 41(5):941–951, 2000.

[34] K. Knogler et al. Copper-67 radioimmunotherapy and growth inhibition by anti-L1-cell adhesion molecule monoclonal antibodies in a therapy model of ovarian cancer metastasis. *Clin Cancer Res*, 13(2):603–11, 2007.

[35] J.N. Bryan et al. A two-antibody model for copper-64 radioimmunotherapy: biodistributions and tumor dosimetry in a mouse model of cancer. *Vet Comp Oncol*, 2(2):82–90, 2004.

[36] W. E. Bolch et al. MIRD Pamphlet No. 17: The Dosimetry of Nonuniform Activity Distributions–Radionuclide S Values at the Voxel Level. *J Nucl Med*, 40(1):11S–36, 1999.

[37] W. V. Prestwich, J. Nunes, and C. S. Kwok. Beta Dose Point Kernels for Radionuclides of Potential Use in Radioimmunotherapy. *J Nucl Med*, 30(6):1036–46, 1989.

[38] P. Bernhardt, H. Ahlman, and E. Forssell-Aronsson. Model of metastatic growth valuable for radionuclide therapy. *Med Phys*, 30(12):3227–32, 2003.

[39] P. Anderson and R. Nuñez. Samarium lexidronam (153Sm-EDTMP): skeletal radiation for osteoblastic bone metastases and osteosarcoma. *Expert Rev Anticancer Ther*, 7(11):1517–27, 2007.

[40] J. Carlsson et al. Tumour therapy with radionuclides: assessment of progress and problems. *Radiother Oncol*, 66(2):107–17, 2003.

[41] M.W. Brechbiel. Targeted alpha-therapy: past, present, future? *Dalton Trans*, 21(43):4918–28, 2007.

[42] A. Lechner et al. Targeted radionuclide therapy: theoretical study of the relationship between tumour control probability and tumour radius for a $^{32}P/^{33}P$ radionuclide cocktail. *Phys Med Biol*, 53(7), 1961-1974, 2008.

[43] I.F. Ciernik et al. Radiation treatment planning with an integrated positron emission and computer tomography (PET/CT): a feasibility study. *Int J Radiat Oncol Biol Phys*, 57(3):853–63, 2003.

[44] G. Sgouros et al. Patient-Specific Dosimetry for 131I Thyroid Cancer Therapy Using 124I PET and 3-Dimensional-Internal Dosimetry (3D-ID) Software. *J Nucl Med*, 45(8):1366–72, 2004.

[45] G. Flux et al. The impact of PET and SPECT on dosimetry for targeted radionuclide therapy. *Z Med Phys*, 16(1):47–59, 2006.

[46] S. Palm et al. Pharmacokinetics and Biodistribution of 86Y-Trastuzumab for 90Y Dosimetry in an Ovarian Carcinoma Model: Correlative MicroPET and MRI. *J Nucl Med*, 44(7):1148–55, 2003.

[47] J. C. Johnson et al. Calculation of Radiation Dose at a Bone-to-Marrow Interface Using Monte Carlo Modeling Techniques (EGS4). *J Nucl Med*, 33(4):623–28, 1992.

[48] H. Yoriyaz, M. G. Stabin, and A. dos Santos. Monte Carlo MCNP-4B-Based Absorbed Dose Distribution Estimates for Patient-Specific Dosimetry. *J Nucl Med*, 42(4):662–669, 2001.

[49] International Commission of Radiological Protection. *Recommendations of the ICRP. ICRP Publication 103*. Elsevier Science, 2007.

[50] R. Loevinger, T. Buchinger, and E. Watson, editors. *MIRD Primer for Absorbed Dose Calculations*. Society of Nuclear Medicine, 1988.

[51] M. Stabin. Nuclear medicine dosimetry. *Phys Med Biol*, 51(13):R187–R202, 2006.

[52] W. E. Bolch et al. MIRD Pamphlet No. 21: A Generalized Schema for Radiopharmaceutical Dosimetry–Standardization of Nomenclature. *J Nucl Med*, 50(3):477–84, 2009.

[53] Y. Imahori et al. Positron emission tomography-based boron neutron capture therapy using boronophenylalanine for high-grade gliomas: part I. *Clin Cancer Res*, 4(8):1825–32, 1998.

[54] H.P. Press et al. *Numerical Recipes in C++. The Art of Scientific Computing*. Cambridge University Press, 2002.

[55] A. Birchall and A. C. James. A microcomputer algorithm for solving first-order compartmental models involving recycling. *Health Phys*, 56(6):857–68, 1989.

[56] N. Petoussi-Henss, M. Zankl, and D. Nosske. Estimation of patient dose from radiopharmaceuticals using voxel models. *Cancer Biother Radiopharm*, 20(1):103–9, 2005.

[57] K. F. Eckerman and M. G. Stabin. Electron absorbed fractions and dose conversion factors for marrow and bone by skeletal regions. *Health Phys*, 78(2):199–214, 2000.

[58] R. J. Cloutier et al. Calculating the Radiation Dose to an Organ. *J Nucl Med*, 14(1):53–55, 1973.

[59] T. Smith, N. Petoussi-Henss, and M. Zankl. Comparison of internal radiation doses estimated by MIRD and voxel techniques for a "family" of phantoms. *Eur J Nucl Med*, 27(9):1387–98, 2000.

[60] International Commission of Radiological Protection. *ICRP Publication 60: 1990 Recommendations of the International Commission on Radiological Protection*. Pergamon Press, 1991.

[61] W.S. Snyder et al. *MIRD Pamphlet No. 11: S, Absorbed Dose per Unit Cumulated Activity for Selected Radionuclides and Organs*. Society of Nuclear Medicine, 1975.

[62] W.S. Snyder et al. Estimates of absorbed fractions for monoenergetic photon sources uniformly distributed in various organs of a heterogeneous phantom. *J Nucl Med*, Suppl 3:7–52, 1969.

[63] M. Cristy and K.F. Eckerman. Specific absorbed fractions of energy at various ages from internal photon sources. Technical Report ORNL/TM-8381, Oak Ridge National Laboratory, Oak Ridge, TN, 1987.

[64] M.G. Stabin et al. Mathematical models and specific absorbed fractions of photon energy in the nonpregnant adult female and at the end of each trimester of pregnancy. Technical Report ORNL/TM-12907, Oak Ridge National Laboratory, Oak Ridge, TN, 1995.

[65] N. Petoussi-Henss et al. The GSF family of voxel phantoms. *Phys Med Biol*, 47(1):89–106, 2002.

[66] M. Zankl and A. Wittmann. The adult male voxel model Golem segmented from whole-body CT patient data. *Radiat Environ Biophys*, 40(2):153–62, 2001.

[67] M. Zankl et al. The construction of computer tomographic phantoms and their application in radiology and radiation protection. *Radiat Environ Biophys*, 27(2):153–64, 1988.

[68] I.G. Zubal et al. Computerized three-dimensional segmented human anatomy. *Med Phys*, 21(2):299–302, 1994.

[69] I.G. Zubal et al. Two dedicated software, voxel based, anthropomorphic (torso and head) phantoms. In P.J. Dimbylow, editor, *Proceedings of a Workshop on Voxel Phantom Development*, pages 6–7, Chilton, UK, 1996. National Radiation Protection Board (NRPB).

[70] Segars W. *Development and application of the new dynamic NURBS-based cardiac-torso (NCAT) phantom*. PhD thesis, The University of North Carolina, 2001.

[71] C. Lee et al. Hybrid computational phantoms of the male and female newborn patient: NURBS-based whole-body models. *Phys Med Biol*, 52(12):3309–33, 2007.

[72] X.G. Xu et al. A boundary-representation method for designing whole-body radiation dosimetry models: pregnant females at the ends of three gestational periods—RPI-P3, -P6 and -P9. *Phys Med Biol*, 52(23):7023–44, 2007.

[73] C. Lee et al. Hybrid computational phantoms of the 15-year male and female adolescent: Applications to CT organ dosimetry for patients of variable morphometry. *Med Phys*, 35(6):2366–82, 2008.

[74] E.W. Watson and M. G. Stabin. In *Computer Applications in Health Physics: Proc. 17th Midyear Topical Symposium of the Health Physics Society*, pages 7.79–7.86, Pasco,WA, 1984.

[75] M. G. Stabin. MIRDOSEthe personal computer software for use in internal dose assessment in nuclear medicine. *J Nucl Med*, 37(3):53846, 1996.

[76] M. G. Stabin, R. B. Sparks, and E. Crowe. OLINDA/EXM: The Second-Generation Personal Computer Software for Internal Dose Assessment in Nuclear Medicine. *J Nucl Med*, 46(6):1023–27, 2005.

[77] T.K. Johnson, D. McClure, and S. McCourt. MABDOSE. I: Characterization of a general purpose dose estimation code. *Med. Phys*, 26(7):1389–95, 1999.

[78] T.K. Johnson, D. McClure, and S. McCourt. MABDOSE. II: Validation of a general purpose dose estimation code. *Med. Phys*, 26(7):1396–1403, 1999.

[79] N. Petoussi-Henss et al. Patient-specific scaling of reference S-values for cross-organ radionuclide S-values: what is appropriate? *Radiat Prot Dosimetry*, 127(1-4):192–96, 2007.

[80] M. T. Hays et al. MIRD Dose Estimate Report No. 19: Radiation Absorbed Dose Estimates from 18F-FDG. *J Nucl Med*, 43(2):210–14, 2002.

[81] International Commission of Radiological Protection. *Radiation dose to patients from radiopharmaceuticals. ICRP Publication 80, Addendum 2 to ICRP 53*. Pergamon Press, 1999.

[82] J.F. Briesmeister. MCNP A general Monte Carlo N-particle transport code, Version 4C. Technical Report LA-13709-M, Los Alamos National Laboratory, 2000.

[83] X-5 Monte Carlo Team. MCNP A General Monte Carlo N-Particle Transport Code, Version 5. Technical Report LA-UR-03-1987, Los Alamos National Laboratory, 2003.

[84] P.A. Love et al. Comparison of EGS4 and MCNP Monte Carlo codes when calculating radiotherapy depth doses. *Phys Med Biol*, 43(5):1351–57, 1998.

[85] R. Jeraj, P.J. Keall, and P.M. Ostwald. Comparisons between MCNP, EGS4 and experiment for clinical electron beams. *Phys Med Biol*, 44(3):705–17, 1999.

[86] H. Yoriyaz et al. Physical models, cross sections, and numerical approximations used in MCNP and GEANT4 Monte Carlo codes for photon and electron absorbed fraction calculation. *Med Phys*, 36(11):5198–213, 2009.

[87] J. Soderberg, G. Alm Carlsson, and A. Ahnesjo. Monte carlo evaluation of a photon pencil kernel algorithm applied to fast neutron therapy treatment planning. *Phys Med Biol*, 48(20):3327–44, 2003.

[88] O. Chibani and X.A. Li. Monte Carlo dose calculations in homogeneous media and at interfaces: a comparison between GEPTS, EGSnrc, MCNP, and measurements. *Med Phys*, 29(5):835–47, 2002.

[89] Transpire, Inc. *ATTILA - 3D multi-group Sn particle transport code*, Version 6 edition, 2006.

[90] J.K. Shultis and R.E. Faw. *An MCNP Primer*. Kansas State University, 2004.

[91] K.A. van Riper. *BodyBuilder Users Guide*. White Rock Science, Version 1.3.0 edition, 2004.

[92] M. Cristy, K.F. Eckerman, and J.C. Ryman. The ORNL Mathematical Phantom Series. Technical report, Oak Ridge National Laboratory Report, Oak Ridge, TN, 1996. Online document at: http://homer.hsr.ornl.gov/VLab/VLabPhan.html (April 2007).

[93] U.A. Fill et al. Adult female voxel models of different stature and photon conversion coefficients for radiation protection. *Health Phys*, 86(3):253–72, 2004.

[94] T.C. Chao, A. Bozkurt, and X.G. Xu. Conversion coefficients based on the VIP-Man anatomical model and EGS4-VLSI code for external monoenergetic photons from 10 keV to 10 MeV. *Health Phys*, 81(2):163–83, 2001.

[95] K. Saito et al. Construction of a computed tomographic phantom for a Japanese male adult and dose calculation system. *Radiat Environ Biophys*, 40(1):69–75, 2001.

[96] Brookhaven National Laboratory. NuDat 2.3, National Nuclear Data Center. Online at: www.nndc.bnl.gov/nudat2, April 2007.

[97] Vanderbilt University. RADAR - Radiation Dose Assessment Resource. Online at: http : //www.doseinfo − radar.com, April 2007.

[98] M. G. Stabin. Developments in the internal dosimetry of radiopharmaceuticals. *Radiat Prot Dosimetry*, 105(1-4):575–80, 2003.

[99] R. Kramer et al. Skeletal dosimetry in the MAX06 and the FAX06 phantoms for external exposure to photons based on vertebral 3D-microCT images. *Phys Med Biol*, 51(24):6265–89, 2006.

[100] R. Kramer et al. All about MAX: a male adult voxel phantom for Monte Carlo calculations in radiation protection dosimetry. *Phys Med Biol*, 48(10):1239–62, 2003.

[101] R. Kramer et al. All about FAX: a Female Adult voxel phantom for Monte Carlo calculation in radiation protection dosimetry. *Phys Med Biol*, 49(23):5203–16, 2004.

[102] K. F. Eckerman et al. Response functions for computing absorbed dose to skeletal tissues from photon irradiation. *Radiat Prot Dosimetry*, 127(1-4):187–91, 2007.

[103] R. Kramer. Ermittlung von Konversionsfaktoren zwischen Körperdosen und relevanten Strahlungskenngröen bei externer Röntgen- und Gamma-Bestrahlung. Technical Report GSF-Report-S-556, Institut für Strahlenschutz, GSF-Forschungszentrum für Umwelt und Gesundheit, Neuherberg-Muenchen, 1979.

[104] M. Zankl et al. Organ dose conversion coefficients for external photon irradiation of male and female voxel models. *Phys Med Biol*, 47(14):2367–85, 2002.

[105] S.D. King and F.W. Spiers. Photoelectron enhancement of the absorbed dose from X rays to human bone marrow: Experimental and theoretical studies. *Br J Radiol*, 58:345–56, 1985.

[106] Tissue Substitutes in Radiation Dosimetry and Measurement, ICRU Report No. 44. Technical report, International Commission of Radiation Units and Measurements, Bethesda, MD, 1989.

[107] International Commission on Radiological Protection. *ICRP Publication 106: Radiation Dose to Patients from Radiopharmaceuticals; A Third Adendum to ICRP Publication 53.* Elsevier Science, 2009.

[108] International Commission of Radiological Protection. *Radiation Dose to Patients from Radiopharmaceuticals. ICRP Publication 53.* Pergamon Press, 1987.

[109] M. T. Hays and G. M. Segall. A Mathematical Model for the Distribution of Fluorodeoxyglucose in Humans. *J Nucl Med*, 40(8):1358–1366, 1999.

[110] L. G. Bouchet et al. MIRD Pamphlet No. 15: Radionuclide S Values in a Revised Dosimetrie Model of the Adult Head and Brain. *J Nucl Med*, 40(3):62S–101, 1999.

[111] N. Petoussi-Henss and M. Zankl. Voxel Anthropomorphic Models as a Tool for Internal Dosimetry. *Radiat Prot Dosimetry*, 79(1-4):415–18, 1998.

[112] M. Zankl et al. The application of voxel phantoms to the internal dosimetry of radionuclides. *Radiat Prot Dosimetry*, 105(1-4):539–48, 2003.

[113] E.Y. Han, W.E. Bolch, and Eckerman K.F. Revisions to the ORNL series of adult and pediatric computational phantoms for use with the MIRD schema. *Health Phys*, 90(4):337–56, 2006.

[114] M. Lenarczyk et al. Biologic Dosimetry of Bone Marrow: Induction of Micronuclei in Reticulocytes After Exposure to 32P and 90Y. *J Nucl Med*, 42(1):162–69, 2001.

[115] Council Directive 97/43/Euratom of 30 June 1997 on health protection of individuals against the dangers of ionizing radiation in relation to medical exposure, and repealing Directive 84/466/Euratom . Online at: http : //eur − lex.europa.eu/RECH$_{l}$egislation.do?ihmlang = en, June 1997.

Appendix A

Example of MCNP input file

Above an example of an MCNP input file used for the simulation model is displayed. It represents an androgynous phantom with a nominal age of 21 years and the liver as source organ.

```
Androgynous Phantom at  21.0 Years
C ++++++++++++++++++++++++++++++++++++++++
C
C    File Prepared by Body Builder
C    CopyRight 1996-2004, White Rock Science
C
C    This input file is for the use of
C    BodyBuilder License holder only.
C    Distribution is Prohibited.
C
C ++++++++++++++++++++++++++++++++++++++++
C
C ++++++++++++++++++++++++++++++++++++++++++++++++
C           CELLS
C ++++++++++++++++++++++++++++++++++++++++++++++++
c SkeletonVolume = 7218.700000, skel_vol = 7142.857143
C
C         LEG BONES
50      2 -1.40     -4 53 (-51 : -52)
                 vol=  2800.00 imp:p = 1
C
C         ARM BONES
70     2 -1.40      4 -73 (-71 : -72)
                 vol=   956.00 imp:p = 1
C
C         PELVIS
90     2 -1.40      91 -92 93 4 -101 (95 : -94)
                 vol=   606.00 imp:p = 1
C
C         SPINE
100    2 -1.40   -100 -103 101 imp:p = 1
101    2 -1.40   -100 -8   103 imp:p = 1
102    2 -1.40   -105 -102 8   imp:p = 1
C               Total Spine vol=   983.00
```

```
c
c         SKULL & FACE
110    2 -1.40   (111 -110):(121 -120 122 -1 -123 110)
                 vol=   923.00 imp:p = 1
c
c         RIBS
130    2 -1.40    132 -131 ((134 -133):(136 -135):(138 -137):(74 -139):
                 (76 -75):(78 -77):(80 -79):(82 -81):(332 -83):
                 (86 -85):(88 -87):(98 -89))
                 vol=   694.00 imp:p = 1
c
c         CLAVICLES
140    2 -1.40    -140 ((141 -143):(-142 144))
                 vol=    54.70 imp:p = 1
c
c         SCAPULAE
150    2 -1.40     131 -156 154 -155 ((150 -152):(-151 153))
                 vol=   202.00 imp:p = 1
c
c         ADRENALS
160     1 -1.04     162 (-160:-161)
                  vol=    15.70 imp:p = 1
c
c         BRAIN
180     1 -1.04    -111
                 vol=  1370.00 imp:p = 1
c
c         BREASTS
190   1  -1.04      11 (-192 : -193) imp:p = 1
            vol=  337.00
c
c         GALL BLADDER
200   1 -1.04       (-202 -200):(202 -201 -203)
                 vol=    63.70 imp:p = 1
c
c         ESOPHAGUS
212   1 -1.04       (213 -212 322 -8 100) :
                    (-216 217 -218 210 350 100)
                 vol=   44.70 imp:p = 1
c           Air in Upper Esophagus
213   4 -0.001293   -213 322 -8
                        imp:p = 1
c
c         STOMACH
210   1 -1.04       -210
                 vol=   402.00 imp:p = 1
c
c         SMALL INTESTINE
220   1 -1.04       -91 221 -222 223 -7
C                exclude         Ascending Colon
                        (232:230:-223)
c                exclude         Transverse Colon
                        (240 :241 : -242 : -221 : -232 )
c                exclude         Descending Colon
                        (232:250:-223)
                  vol=  1060.00 imp:p = 1
c
```

```
c
c          ASCENDING COLON
230   1 -1.04        -230 231 -232
                   vol=   187.50 imp:p = 6
c
c          TRANSVERSE COLON
240   1 -1.04        -240 -241 242 232 221
             vol=   248.00 imp:p = 1
c
c          DESCENDING COLON
250   1 -1.04        -250 251 -232
               vol=  191.90 imp:p = 1
c
c          SIGMOID COLON
280   1 -1.04        (-280 282 -251):(-281 -282 4)
               vol=  106.00 imp:p = 6
c
c          HEART
290     1 -1.04      (290((-291 -292):(291 -293))):
                     (-290((-291 -295):(291 -294)))
                   vol=   740.00 imp:p = 1
c
c          KIDNEYS
310     1 -1.04      (-310 312 -162):(-311 -313 -162)
                    vol=   288.00 imp:p = 1
c
c          LIVER
320     1 -1.04      -320 -321 7 -322 -132
                     vol=  1830.00 imp:p = 1
c
c          LUNGS
330     3 -0.296   332 ((-331 (-335:336:334:-333)):
                          (-330 ( 339:338:337)))
                   vol=  3380.00 imp:p = 1
c moritz st c 330 s
c
c          OVARIES
340    1 -1.04        -340:-341
               vol=    8.38 imp:p = 1
c
c          PANCREAS
350   1 -1.04        -350 351 (352:-312)
                   vol=    90.70 imp:p = 1
c
c          SPLEEN
360   1 -1.04        -360
                   vol=  176.00 imp:p = 1
c
c          TESTICLES
370   1 -1.04        -370:-371
               vol=   37.60 imp:p = 6
c
c          THYMUS
380     1 -1.04  -380
                 vol=    20.10 imp:p = 1
```

```
c         THYROID
390     1 -1.04     -390 391 -392 -393 8
                  vol=    19.90 imp:p = 1
c
c         URINARY BLADDER
410   1 -1.04        -410
            vol=  248.70 imp:p = 6
c
c             UTERUS
420   1 -1.04        -420 421
            vol=   76.00 imp:p = 1
c
c         PENIS & SCROTUM
40     1 -1.04        -1 -4 47 -45 49 -48 37 38
c                 exclude         Testicles
                   370 371
            vol=  158.40 imp:p = 6
c
c         SKIN
c
c               Head & Neck Skin
22    1 -1.04        ((-21 22 9):(-20 23 -9 12))
                    imp:p = 1
28    1 -1.04         28 -27 8 -12
            vol=  318.00 imp:p = 1
c           (Above Volume for Head + Neck Skin Combined
c
c           Trunk Skin
17    1 -1.04        (-8 18 20 -10)
                     : (4 -18 -10 11
c                 exclude         Breasts
                          192 193
                     )
            vol= 1440.00 imp:p = 1
c            Breast Skin
192   1  -1.04       10 ((-190 192):(-191 193))
            vol=   51.00 imp:p = 1
c
c         Penis & Scrotum Skin
41     1 -1.04        -1 -4  41 -42 43 -44 31 32 #40
c                 exclude         Testicles
                   370 371
            vol=   23.40 imp:p = 6
c        Legs Skin
34    1 -1.04       -4 34 -31 36 32 : -31 33 -36 32
            vol=  605.00 imp:p = 6
35    1 -1.04       -4 35 -32 36 31 : -32 33 -36 31
            vol=  605.00 imp:p = 6
c
c           HEAD
c
20    1 -1.04        ((-22 9):(-23 -9 12))
c                 exclude         Skull & Brain
                         110
c                 exclude         Face Bones
                          (-121:120:-122:1:123:-110)
c                 exclude         Spine
```

```
                    (105:-8:102)
c                exclude          Thyroid
                    (390:-391:392:393:-8)
                 imp:p = 1
c
c            NECK
c
27    1 -1.04       -28 8 -12
c                exclude          Spine
                     105
c                exclude          Thyroid
                    (390:-391:392:393:-8)
                 imp:p = 1
c
c         OUTER TRUNK---ARMS & SCAPULAE
c
10    1 -1.04       4 131 -18 -11
c                exclude          Scapulae
                    (-131:156:-150:152:-154:155)
                    (-131:156:151:-153:-154:155)
c                exclude          Arm Bones
                    (-4:71:73) (-4:72:73)
c                exclude           Uterus
                    (420:-421)
                 imp:p = 1
c
c         UPPER TRUNK---ABOVE RIBS
c
11    1 -1.04   ((-18 -131 133) : (-8 18 -20 -10))
c                 exclude          Spine
                       (105:102:-8)(100:8:-133)
c                 exclude          Clavicles
                       (140:-141:143) (140:142:-144)
c                 exclude          Upper Lungs
                       (-133:330) (-133:331)
c                 exclude           Thymus
                       380
c                 exclude           Esophagus
                      #212 #213
                  imp:p = 1
c
c
c         UPPER RIB CAGE
c
12    1 -1.04       -131 132 79 -133
c                exclude          Ribs 1-9
                  (131:-132:133:-134) (131:-132:135:-136) (131:-132:137:-138)
                  (131:-132:139:-74) (131:-132:75:-76) (131:-132:77:-78)
                 imp:p = 1
c
c
c         LOWER RIB CAGE
c
13    1 -1.04       -131 132 -79 98
c                exclude          Ribs 10-12
                  (131:-132:85:-86) (131:-132:87:-88) (131:-132:89:-98)
                  (131:-132:79:-80) (131:-132:81:-82) (131:-132:83:-332)
```

```
                imp:p = 1
c
c
c         HIGH CHEST ORGANS
c
14    1 -1.04       -132 -133 332
c                 exclude          Spine
                        (100:133:-332)
c                 exclude          Heart
                        #290
c                 exclude          Lungs
                        (330:133:-332:(-339 -338 -337))
                        (331:133:-332:(335 -336 -334 333))
c                 exclude          Thymus
                        380
c                 exclude          Esophagus
                       #212 #213
                  imp:p = 1
c
c         CHEST---LIVER LEVEL
c
15    1 -1.04       ((-132 -332 98):(-131 -98 7))
c                 exclude          Spine
                        (100:332:-7)
c                 exclude          Adrenals
                      (160:-162) (161:-162)
c                 exclude          Gall Bladder
                        (202:200) (-202:201:203)
c                 exclude          Kidneys
                        (310:-312) (311:313)
c                 exclude          Liver
                        #320
c                       (320:321:322:-7)
c                 exclude         Pancreas
                      (350:-351:(-352 312))
c                 exclude          Spleen
                        360
c                 exclude          Esophagus
                       #212 #213
c                 exclude         Stomach
                      210
                  imp:p = 1
c
c
c         LOWER TRUNK
c
16    1 -1.04       -131 4 -7
c                 exclude           Spine
                        (100:-101:7)
c                 exclude           Pelvis
                       #90
c                 exclude           Small Intestine
                        (91:-221:222:-223:7)
c                 exclude           Ascending Colon
                        (232:230:-231)
c                 exclude           Descending Colon
                        (232:250:-251)
```

```
c                exclude           Sigmoid Colon
                        (280:-282:251) (281:282:-4)
c                exclude           Urinary Bladder
                       410
c                exclude          Uterus
                        (420:-421)
c                exclude           Ovaries
                        340 341
                 imp:p = 1
c
c        LEGS
c
30    1 -1.04       -4 36 (-34 : -35)
c                exclude           Leg Bones
                        (4:51:-53) (4:52:-53)
             vol= 16790.00 imp:p = 1
c
c         SURROUNDING AIR
600    4 -0.001293   -600
c             exclude          HEAD & NECK
                       (21:-9)  (20:9:-8)
c             exclude          TRUNK
                        (-4:10:8)
c                 exclude          BREASTS
                        (-10:(190 191))
c             exclude          LEGS
                        (4:-33:(31 32))
c                 exclude          GENITALIA
                     (1:4:-41:42:-43:44:-31:-32)
              imp:p = 1
c             air             OUTSIDE of NECK
601    4 -0.001293   -20 27 8 -12
              imp:p = 1
c
c         VOID
700   0               600
              imp:p =0

c +++++++++++++++++++++++++++++++++++++++++++++++
c           SURFACES
c +++++++++++++++++++++++++++++++++++++++++++++++
c Planes used in several places
c
1     py 0
4     pz 0
332   pz    43.5000
7     pz    27.0000
8     pz    70.0000
9     pz    91.4500
12    pz    78.4000
c
c          BODY SURFACE
c
c              HEAD
21    sq  5620.5009  3632.4729  6995.6496 0 0 0 -377922.4805 0 0      91.450
22    sq  5112.2500  3271.8400  6400.0000 0 0 0 -327184.0000 0 0      91.450
20    sq   104.0400    67.2400 0 0 0 0 -6995.649600 0 0 0
```

```
23    sq   100.0000    64.0000 0 0 0 0 -6400.000000 0 0 0
c
c
c             NECK
27    cz     5.6000
28    cz     5.4000
c
c
c             TORSO
10    sq   104.0400   408.0400 0 0 0 0 -42452.481600 0 0 0
c             Torso Skin
11    sq   100.0000   400.0000 0 0 0 0 -40000.000000 0 0 0
18    pz    69.8000
c
c             LEGS
31    gq 1 1 0 0 0  -0.2000   -20.2000 0 0 0
32    gq 1 1 0 0 0   0.2000    20.2000 0 0 0
33    pz  -80.200
c                Leg Skin
34    gq 1 1 0 0 0  -0.2000   -20.0000 0 0 0
35    gq 1 1 0 0 0   0.2000    20.0000 0 0 0
36    pz  -80.000
c                Genitalia Skin
37    gq 1 1 0 0 0  -0.2000   -20.4000 0 0 0
38    gq 1 1 0 0 0   0.2000    20.4000 0 0 0
c
c         PENIS & SCROTUM
41    pz    -4.8000
42    p  0 -10.00 -1 100.00
43    p   -10.00 0 1 -100.00
44    p    -10.00 0 -1 100.00
c
c             Penis & Scrotum Skin
47    pz    -4.6000
45    p  0 -10.10 -1 100.00
49    p   -10.10 0 1 -100.00
48    p    -10.10 0 -1 100.00
c
c     SKELETON
c
c
c         LEG BONES
51    gq   1 1  0.009069 0 0  -0.200501   -20.000000
            0   1.785714      87.7500
52    gq   1 1  0.009069 0 0   0.200501    20.000000
            0   1.785714      87.7500
53    pz   -79.8000
c
c         ARM BONES ( left/right) )
71     gq   0.510204     0.137174 0 0 0     0.010352
           -19.489796 0    -0.204969   185.877551
72    gq   0.510204   0.137174 0 0 0    -0.010352
            19.489796 0    -0.204969     185.877551
73    pz     69.0000
c
c         PELVIS
91    sq   127.6900   127.6900 0 0 0 0 -16304.7361
```

```
91    sq   127.6900   127.6900 0 0 0 0 -16304.7361
       0    -3.8000 0
92    sq   144.0000   144.0000 0 0 0 0 -20736.0000 0    -3.0000 0
93    py    -3.0000
94    py     5.0000
95    pz    14.0000
c
c         SPINE
100      sq      6.2500     4.0000 0 0 0 0   -25.0000 0     5.5000 0
105      sq      6.2500     4.0000 0 0 0 0   -25.0000 0     1.4500 0
101      pz    22.0000
102      pz    84.8000
103      pz    35.1000
c
c     SKELETON
c
c
c             SKULL (head)
c
c
c             CRANIUM
110    sq  3991.0806  2487.5156  5076.5625 0 0 0
     -224498.2852 0 0    91.4500
111    sq   2445.3025  1440.2025  3221.6976 0 0 0
         -106517.3769 0 0    91.4500
c
c         FACIAL
120      sq     81.0000    49.0000 0 0 0 0 -3969.0000 0 0 0
121      sq     57.7600    31.3600 0 0 0 0 -1811.3536 0 0 0
c
122      pz    82.4000
123      pz    93.1300
c
c         RIBS
131      sq     96.0400   289.0000 0 0 0 0 -27755.5600 0 0 0
132      sq     86.4900   272.2500 0 0 0 0 -23546.9025 0 0 0
133      pz    67.3000
134     pz    65.9000
135      pz     64.5000
136      pz     63.1000
137      pz     61.7000
138      pz     60.3000
139      pz     58.9000
74       pz     57.5000
75       pz     56.1000
76       pz     54.7000
77       pz     53.3000
78       pz     51.9000
79       pz     50.5000
80       pz     49.1000
81       pz     47.7000
82       pz     46.3000
83       pz     44.9000
85       pz    42.1000
86       pz    40.7000
87       pz    39.3000
88       pz    37.9000
```

```
89      pz    36.5000
98     pz    35.1000
c
c         CLAVICLES
140     tz    0    11.1000    68.2500
           20.0000   0.788300   0.788300
141     p   7.034200 1 0     11.100
142     p   7.034200 -1 0    -11.100
143     p   0.894150 1 0     11.100
144     p   0.894150 -1 0    -11.100
c
c         SCAPULAE
156     sq    96.0400   361.0000 0 0 0 0 -34670.4400
           0 0 0
150   p      0.2500 1 0 0
151   p      0.2500 -1 0 0
152   p      0.8000 1 0 0
153   p      0.8000 -1 0 0
154   pz    50.9000
155   pz    67.3010
c
c         ADRENALS
160   1 sq     6.2500    56.2500     0.5625 0 0 0   -14.0625 0 0 0
161   2 sq     6.2500    56.2500     0.5625 0 0 0   -14.0625 0 0 0
162    pz    38.0000
c
c             BREASTS
c                left
190    sq   325.8928   421.9943   463.6486 0 0 0 -7985.1873
             10.0000    -8.6603    52.0000
c                right
191    sq   325.8928   421.9943   463.6486 0 0 0 -7985.1873
            -10.0000    -8.6603    52.0000
192    sq   268.7141   352.0314   388.5827 0 0 0 -6062.8609
             10.0000    -8.6603    52.0000
193    sq   268.7141   352.0314   388.5827 0 0 0 -6062.8609
            -10.0000    -8.6603    52.0000
c
c         GALL BLADDER
200  3 so     2.1200
201  3 gq 1 1 -0.05175625 0 0 0 0 0   0.964600  -4.494400
202  3 pz 0
203  3 pz     8.0000
c
c         ESOPAHGUS
212    sq     0.1764     1.3689 0  0 0 0    -0.2415 0     2.5750 0
213    sq     0.0144     0.7569 0  0 0 0    -0.0109 0     2.5750 0
216 6  cx     0.7000
217 6  px     0.1000
218 6  px     7.8000
c
c         STOMACH
210    sq   576.0000  1024.0000   144.0000 0 0 0 -9216.0000
             8.0000    -4.0000    35.0000
c extent     4.0000    12.0000    -7.0000    -1.0000    27.0000    43.0000
c
c         SMALL INTESTINE
```

```
221     py     -4.8600
222     py      2.2000
223     pz     17.0000
c
c          ASCENDING COLON
230     sq      6.2500      6.2500 0 0 0 0    -39.0625     -8.5000     -2.3600 0
231     pz     14.4500
232     pz     24.0000
c
c          TRANSVERSE COLON
240     sq  0   2.250000      6.2500 0 0 0    -14.0625 0     -2.3600     25.5000
241     px     10.5000
242     px    -10.5000
c
c
c          DESCENDING COLON
251      pz      8.7200
250     gq   4.536900   3.534400      0.106435 0      1.156545     -0.463191
             -72.816057      -10.085068        2.067006   283.328636
c
c
c          SIGMOID COLON
282     px      3.0000
280     ty      3.0000 0      8.7200      5.7200      1.5700      1.5700
281     ty       3.000 0 0       3.000      1.5700      1.5700
c
c          HEART
c
290  4 px 0
291  4 pz 0
c
c          Left Ventricle
292   4 sq  1225.0000  3624.0400  1849.0000 0 0 0 -90601.0000 0 0 0
c          Right Ventricle
293   4 sq   240.2500   710.7556  1849.0000 0 0 0 -17768.8900 0 0 0
c
c          Left Atrium
294   4 sq   240.2500   280.2276   729.0000 0 0 0 -7005.6900 0 0 0
c
c          Right Atrium
295   4 sq  1225.0000  1428.8400   729.0000 0 0 0 -35721.0000 0 0 0
c
c
c          KIDNEYS
310    sq    68.0625   612.5625    45.5625 0 0 0 -1378.2656
              6.0000     6.0000    32.5000
311    sq    68.0625   612.5625    45.5625 0 0 0 -1378.2656
             -6.0000     6.0000    32.5000
312    px     3.0000
313    px    -3.0000
c
c          LIVER
320    sq    64.0000   272.2500 0 0 0 0 -17424.0000 0 0 0
321     p      1935.0      1505.0     -1575.0    -67725.0
322    pz    43.0000
c
c
```

```
c          LUNGS
330     sq       32.4000       14.4000        1.4063 0 0 0
                 -810.0000      8.5000 0     43.5000
331   sq       32.4000       14.4000        1.4063 0 0 0
                 -810.0000     -8.5000 0     43.5000
333     px     -5.4000
334     py      1.5000
335     pz     46.0000
336     pz     54.0000
337     px      8.0000
338     py      1.0000
339     pz     55.0000
c
c          OVARIES
340     sq      1.0000      4.0000      0.2500 0 0 0     -1.0000
                6.0000 0     15.0000
341     sq      1.0000      4.0000      0.2500 0 0 0     -1.0000
               -6.0000 0     15.0000
c
c
c          PANCREAS
350 sq     15.6816  2787.8400   368.6400 0 0 0 -4014.4896
           -1.0000 0     37.0000
351     px     -1.0000
352     pz     37.0000
c
c          SPLEEN
360     sq   144.0000   441.0000    49.0000 0 0 0 -1764.0000
              11.0000     3.0000    37.0000
c extent      7.5000    14.5000     1.0000     5.0000    31.0000    43.0000
c
c          TESTICLES
370     sq     11.9025000      8.940100      3.802500 0 0 0   -20.1152250
               1.3000    -8.0000    -2.3000
371     sq     11.9025000      8.940100      3.802500 0 0 0   -20.1152250
              -1.3000    -8.0000    -2.3000
c
c          THYMUS
380     sq     10.2400    36.0000     1.4400 0 0 0
             -23.0400 0    -7.3000    57.0000
c extent     -1.5000     1.5000    -8.1000    -6.5000    53.0000    61.0000
c
c            THYROID
390     c/z 0    -3.1500     2.2000
391     c/z 0    -3.1500     1.0000
392     py     -3.1500
393     pz     75.0000
c
c          URINARY BLADDER
410     sq   142.9881   293.9429   293.9429 0 0 0 -3514.9002 0
              -4.5000     8.0000
c extent     -4.9580     4.9580    -7.9580    -1.0420     4.5420    11.4580
c
c            UTERUS
420     sq    67.1645812    16.9200596   187.04391696 0 0 0  -461.04455091
          0   -2.000   14.000
421     py     -4.6200
```

```
c
c      Void
600    so 301
c
c     STATISTICS
c  Weight =    73.54 kg ( =   162.13 pounds)
c  Height =   179.00 cm ( =    70.47 inches)

c ++++++++++++++++++++++++++++++++++++++++++++++
c
c         TRANSFORMATIONS
c ++++++++++++++++++++++++++++++++++++++++++++++
c
c         ADREANALS
tr1         3.500       5.000     38.0000
        0.615662   0.788010 0
       -0.788010   0.615662 0
      0        0        1
tr2        -3.500       5.000     38.0000
        0.615662  -0.788010 0
        0.788010   0.615662 0
      0        0        1
c
c         GALL BLADDER
tr3        -4.500      -3.200      30.000
       -0.057400       0.978   -0.200800
        0.961500   0.000000   -0.274800
        0.268700   0.209000    0.940300
c
c         HEART
tr4        1.000      -1.800      50.000
       0.675100  -0.472700  -0.566400
      -0.464000   0.324900  -0.824100
       0.573600   0.819100       0.000
c
c         ESOPHAGUS
tr6        0.000       2.575     42.300
       0.736084  -0.604969  -0.303634
       0.634945   0.772557   0.000000
       0.234575  -0.192791       0.953
c
c ++++++++++++++++++++++++++++++++++++++++++++++
c      MATERIALS
c      Compositions from ORNL Report TM-8381
c ++++++++++++++++++++++++++++++++++++++++++++++
mode p
lost 100 100
nps 20000000
C TR1 0 92 12.5 1 0 0 0 0 -1 0 -1 0
c      Adult Tissues (Density = 1.04 g/cc)
m1       1000  -0.10454
         6000  -0.22663
         7000  -0.02490
         8000  -0.63525
        11000  -0.00112
        12000  -0.00013
        14000  -0.00030
```

```
         15000  -0.00134
         16000  -0.00204
         17000  -0.00133
         19000  -0.00208
         20000  -0.00024
         26000  -0.00005
         30000  -0.00003
         37000  -0.00001
         40000  -0.00001
C
C        Skeleton (Density = 1.4 g/cc)
m2        1000  -0.07337
          6000  -0.25475
          7000  -0.03057
          8000  -0.47893
          9000  -0.00025
         11000  -0.00326
         12000  -0.00112
         14000  -0.00002
         15000  -0.05095
         16000  -0.00173
         17000  -0.00143
         19000  -0.00153
         20000  -0.10190
         26000  -0.00008
         30000  -0.00005
         37000  -0.00002
         38000  -0.00003
         82000  -0.00001
C
C        Lung (Density = 0.296 g/cc)
m3        1000  -0.10134
          6000  -0.10238
          7000  -0.02866
          8000  -0.75752
         11000  -0.00184
         12000  -0.00007
         14000  -0.00006
         15000  -0.00080
         16000  -0.00225
         17000  -0.00266
         19000  -0.00194
         20000  -0.00009
         26000  -0.00037
         30000  -0.00001
         37000  -0.00001
C
C       Air (Density = 0.001020 /cc)
m4        6000  -0.00012
          7000  -0.75527
          8000  -0.23178
         18000  -0.01283
C
C +++++++++++++++++++++++++++++++++++++++++++++++
C   User Supplied Cards
C +++++++++++++++++++++++++++++++++++++++++++++++
SDEF CEL=320 ERG=0.511 X=D1 Y=D2 Z=D3 EFF=0.00001
```

```
SI1 -21 21
SP1 0 1
SI2 -11 11
SP2 0 1
SI3 0 100
SP3 0 1
f16:p 180
f26:p 50
f36:p 70
f46:p 90
f56:p 110
f66:p 130
f76:p 140
f86:p 150
f96:p 160
f106:p 200
f116:p 212
f126:p 210
f136:p 220
f146:p 17
f156:p 41
f166:p 34
f176:p 35
f186:p 30
f196:p 230
f206:p 240
f216:p 250
f226:p 280
f236:p 290
f246:p 310
f256:p 320
f266:p 330
f276:p 350
f286:p 360
f296:p 370
f306:p 380
f316:p 390
f326:p 410
f336:p 40
f346:p 28
f356:p 190
f366:p 340
f376:p 420
```